UNIVERSITAT DE
BARCELONA

Nanoscale electrical characterization of biological matter at microwave frequencies

Maria Chiara Biagi

ADVERTIMENT. La consulta d'aquesta tesi queda condicionada a l'acceptació de les següents condicions d'ús: La difusió d'aquesta tesi per mitjà del servei TDX (**www.tdx.cat**) i a través del Dipòsit Digital de la UB (**diposit.ub.edu**) ha estat autoritzada pels titulars dels drets de propietat intel·lectual únicament per a usos privats emmarcats en activitats d'investigació i docència. No s'autoritza la seva reproducció amb finalitats de lucre ni la seva difusió i posada a disposició des d'un lloc aliè al servei TDX ni al Dipòsit Digital de la UB. No s'autoritza la presentació del seu contingut en una finestra o marc aliè a TDX o al Dipòsit Digital de la UB (framing). Aquesta reserva de drets afecta tant al resum de presentació de la tesi com als seus continguts. En la utilització o cita de parts de la tesi és obligat indicar el nom de la persona autora.

ADVERTENCIA. La consulta de esta tesis queda condicionada a la aceptación de las siguientes condiciones de uso: La difusión de esta tesis por medio del servicio TDR (**www.tdx.cat**) y a través del Repositorio Digital de la UB (**diposit.ub.edu**) ha sido autorizada por los titulares de los derechos de propiedad intelectual únicamente para usos privados enmarcados en actividades de investigación y docencia. No se autoriza su reproducción con finalidades de lucro ni su difusión y puesta a disposición desde un sitio ajeno al servicio TDR o al Repositorio Digital de la UB. No se autoriza la presentación de su contenido en una ventana o marco ajeno a TDR o al Repositorio Digital de la UB (framing). Esta reserva de derechos afecta tanto al resumen de presentación de la tesis como a sus contenidos. En la utilización o cita de partes de la tesis es obligado indicar el nombre de la persona autora.

WARNING. On having consulted this thesis you're accepting the following use conditions: Spreading this thesis by the TDX (**www.tdx.cat**) service and by the UB Digital Repository (**diposit.ub.edu**) has been authorized by the titular of the intellectual property rights only for private uses placed in investigation and teaching activities. Reproduction with lucrative aims is not authorized nor its spreading and availability from a site foreign to the TDX service or to the UB Digital Repository. Introducing its content in a window or frame foreign to the TDX service or to the UB Digital Repository is not authorized (framing). Those rights affect to the presentation summary of the thesis as well as to its contents. In the using or citation of parts of the thesis it's obliged to indicate the name of the author.

UNIVERSITAT DE
BARCELONA

NANOSCALE ELECTRICAL CHARACTERIZATION OF BIOLOGICAL MATTER AT MICROWAVE FREQUENCIES

Maria Chiara Biagi
November 2016

DOCTORAL THESIS

UNIVERSITAT DE BARCELONA
Facultat de Fisica
Departamento de Electronica

CARACTERIZACIÓN ELÉCTRICA A LA NANOESCALA DE MATERIAL BIÓLOGICO EN EL RANGO DE LAS MICROONDAS

Programa de Doctorado:
Nanociencia

Línea de Investigación:
Nanobiotecnologia

Directors de Tesis:
Gabriel Gomila Lluch
Laura Fumagalli

Autor:
Maria Chiara Biagi

“You have to start with the truth. The truth is the only way that we can get anywhere. Because any decision-making that is based upon lies or ignorance can't lead to a good conclusion.”

Julian Assange

CONTENTS

LIST OF ABBREVIATIONS AND ACRONYMS

Abbreviation	Description
AC	alternating current
AFM	atomic force microscopy / microscope
DC	continuous current
EFM	electrostatic force microscopy
EM	electromagnetic
KFM	kelvin force microscopy
NF	near-field
SCM	scanning capacitance microscopy
SEM	scanning electron microscopy
SPM	scanning probe microscopy
STM	scanning tunnelling microscopy
SMM	scanning microwave microscopy

INTRODUCTION

Microwaves are electromagnetic radiation covering the spectrum of frequency between 300 MHz and 300 GHz, and wavelength from 1 m to 1 cm [1]

Their impact in our lives as biological entities embraces fundamentally two wide areas. First, we move in a space full of microwave radiation, emitted or received by the antennae of telecommunication and remote sensing systems operating at these frequencies, such as GSM mobile phones, radar, satellite radio and television, WLAN, GPS systems etc. The use of microwaves in telecommunication has undoubted advantages (elevated directivity and data transmission rate, small antennae dimension, low power required…), but brings along safety concerns about the biological effects of prolonged exposure to such EM fields, even at low intensities. Secondarily, microwave radiation is the energy carrier of a new generation of medical tools for diagnostics and therapy, currently under development or clinical validation. As it will be discussed further on, microwaves have peculiar characteristics with respect to lower and higher frequency bands, which make them particularly suitable for applications in biology and life science.

Most of our knowledge about the interaction of microwave radiation with biological matter has comes from microwave dielectric spectroscopy. Starting in‘50s, with works by England and Sharples [2, 3], Cook [4] and including extensive studies by Schwan [5], microwave dielectric spectroscopy has been used and constantly improved to electrically characterize complex systems, from tissues to single cells.

Investigations on the polarization mechanisms of organs and tissues provided essential knowledge about their characteristic dielectric response: it was found that this is essentially produced by the energy transfer from the microwave radiation to the water polar molecules of the tissue. Furthermore, since cells composing different tissues in the body have also different water content, it was observed a clear specificity of the dielectric properties of distinct tissues, as blood, bone, fat, and grey matter, which brought to the definition of a concept called “dielectric signature”. These findings fostered a number of clinic applications for therapeutics (hyperthermia treatment, ablation, angioplasty, tissue welding), and diagnostics (microwave imaging, blood perfusion measurements, stents evaluation).

Dielectric spectroscopy measurements are performed in general by means of either resonant or non-resonant techniques. EM cavities are examples of the first kind: in this case the sample acts like a perturbation to the EM field inside the resonator, which can be monitored as a change of the resonance frequency and quality factor. Transmission lines such as coaxial cables are instead non-resonant systems: when they are placed in contact with the tissue, or immersed in the liquid under study, the biological medium modifies the electromagnetic field of the transmission line, and alters the reflection and transmission of the waves. In both implementations, the dielectric polarization response (i.e. the complex permittivity) of the sample can be retrieved from the changes on the monitored parameters affected by the field perturbation: quality factor, resonance frequency or scattering parameters. In these configurations, the sample size and the radiation wavelength are in the same scale range, in the order of 3cm at 10GHz. Therefore, the values measured for the permittivity result in fact from an average of the electromagnetic response over millimetres to centimetres cube volume, whereas notoriously the biological materials present heterogeneities in much smaller length scales.

In order to resolve these heterogeneities, and thanks to the miniaturization of MEMS and microfluidic devices, microwave dielectric microscopy was recently downscaled and upgraded to a characterization technique for single cells. Single cell measurements have been made in static cells in broadband [6] and narrowband [7] frequency range, or in a cells moving in a flow [8], [9] . In particular, the ability to detect cells individually in a flow opens the way for the development of microwave flow cytometers.

Single tumour cell could be identified upon their larger water content; stem cells also could have intrinsic properties potentially well distinct from the cells they become once differentiated. Single cell microwave dielectric spectroscopy *per se* also finds applications as tool for cell analysis and sorting: if compared with the most employed techniques, based on optical microscopy with labels, it offers then the advantages of being contactless, non-destructive, and label-free. Yet, it has still less specificity, resolution, and ease of interpretation than imagining techniques.

With this respect, a shift in the strategy for the electrical characterization of cellular and intra-cellular material has been fostered, namely from spectroscopy to imaging microscopy. Near-Field Scanning Microwave Microscopy (NF-SMM) is forwarding this new approach, which consists in using the specific dielectric polarization as contrast mechanism to form the image. Leveraging on the microwave capabilities of penetration throughout the cell membrane (see section 1.2), and free from the constraint that the spatial resolution is dictated by the frequency (see section 2.2), NF-SMM enables to resolve the dielectric properties with sub-micrometric (hence sub-cellular) resolution.

This information would help understanding the physiological mechanisms at the basis of targeted therapeutic tools, or those implicated in effects of the exposition to microwave EM fields.

For instance, in the growing field of nanoparticles for drug delivery and diagnostics, the use of such an imaging tool would be of great advantage for a comprehensive understanding of the target structures, distribution, interaction sites and intracellular fate of the nanoparticles after administration. At present, the detection and localization of metallic and oxide nanoparticles inside the cells are mostly performed via optical techniques such as confocal laser scanning microscopy (CLSM), multispectral imaging systems, or super-resolution optical microscopy (STORM) [10], or via transmission electron microscopy [11]. The optical techniques allow to conduct live cell imaging in physiologic conditions, and can achieve resolution from sub-microns to nanometres (STORM), but require labels for the nanoparticles and/or the cell compartments. Conversely, TEM can achieve sub-nanometric resolution and does not require labelling, but it operates in high vacuum conditions and on sectioned samples, for which an extensive and laborious preparation is still needed. In this context, NF-SMM could supplement these techniques, and offer complementary features such as label-free easy sample preparation, nanometric resolution and, potentially, the possibility to work in physiologic conditions.

Also the investigation of the specific biological effects of exposure requires to be able to resolve the local microwave response of sub-cellular and molecular structures. Indeed, although the evaluation of the exposure risk is usually done in tissues~~,~~ the effects of microwaves on tissues originate at a much smaller level of complexity, and can be only explained by looking at the cell physiology. Microwave fields can trigger a chain of events that starts at subcellular level, altering the charge distribution, the chemical state or the energy of the biological structures [12]. These changes can be sensed and amplified throughout the biological scale to produce responses at the level of the entire organism.

The scientific effort is now going in the direction of shedding light on these subcellular interactions, for which it requires experimental techniques able to resolve the dielectric properties at sub-micrometric scale. NF-SMM seems to be the most promising tool to this aim.

However, despite the implications and impact discussed above, practically no quantitative experimental results have been reported about the microwave dielectric properties of biological sample at such scales. This can be alleged both to the early stage maturity of NS-SMM for Life Science, and to the complexity of the interpretation of the measurements in organic samples. The work done in this Thesis is an effort to fill this lack. Precisely, the objective of my Thesis is to obtain quantitative information, at the nanoscale, about the microwave dielectric response of a single cell, by means of an AFM based NF-SMM.

The research has primarily consisted in the implementation of the analysis tools needed for the application of the technique to biological matter. Specifically, it included developing the required software tools to analyse the SMM data, and the appropriate theoretical models to interpret them; validating the implemented tools on test samples, such as inorganic dielectric structures; and finally measuring a biological sample of interest, namely a bacterial single cell.

In the *1st chapter* I will review the mechanisms of interaction of EM radiation and matter, focusing on microwave radiation and biological matter.

In the *2nd chapter* I will give an overview of the NF-SMM principles and most common implementations. I will also describe, in particular, the setup used in this work, and the procedure to calibrate the measurements, and finally present a critical review of the reported studies of biological samples with NF-SMM.

Chapters 3 and *4* are devoted to the methodology of data analysis of SMM images. In the *3rd chapter* I will describe the problem of topography crosstalk, affecting the measurements in most cases, and illustrate the procedure conceived to remove its effect. The procedure proposed allows to obtain images only related to the intrinsic electric response of the sample, and free from the topography crosstalk.

In the *4th* chapter I will present the procedures to quantify the SMM images acquired, in terms of dielectric permittivity of the sample. In particular in the first part I describe the methodologies to determine the geometry of the system, whereas in the second part they are detailed the methods to extract the permittivity.

In the appendix of *5th* and *6th* chapters I will show how I validated the procedures described on a reference SiO_2 sample, for which the permittivity values are extracted from the intrinsic electric images.

The *5th* chapter deals with the measurement of the permittivity of thin heterogeneous oxides. I will illustrate how intrinsic images acquired in contact mode can be directly related to the permittivity of the oxides, without the need of theoretical models or the knowledge of the system geometry, and represent maps of the microwave permittivity.

Finally, in the *6th chapter* I will apply the methods described in the previous chapters and validated on the inorganic samples, to a biological sample, namely a single E.coli bacterial cell, thus quantifying for the first time the local nanoscale microwave permittivity of a single cell.

1. MECHANISMS OF INTERACTION OF EM FIELDS AND BIOLOGICAL MATTER

The physics of the interaction of microwave EM fields with biological materials is described in this chapter. In order to fully understand the peculiarities of microwaves with respect to other EM frequencies, the mechanisms of interaction of the full EM spectrum are presented.

1.1 Ionization and non-ionization

When the EM radiation penetrates inside a dielectric material such as a tissue or a cell, it can be reflected, transmitted or adsorbed by its molecules. One mechanism of adsorption is the perfect coupling between the frequency of the EM wave and the frequency of oscillation of the vibrational or rotational modes of the molecules. Alternatively, energy high enough can remove electrons from the molecular orbitals, thus altering or destroying the chemical bonds between the atoms. This latter process is called ionization, and the energy associated, ionization potential. Ionization is particularly dangerous in biological systems, because it irreversibly modifies their biochemistry: it is associated to phenomena such as photobleaching, radiolysis, and radiation damage.

Ionization potentials are typically of the order of 10eV [13], whereas microwave quantum energies are well below this value (for instance, the energy of a wave at 1GHz frequency is $4.12 \cdot 10^{-5}$ eV). In fact, microwaves are a nonionizing radiation, safer then for biological specimens than higher frequency radiation, such as electrons or X-rays.

Microwave energy rather interacts in the first way above mentioned: it is adsorbed by the vibrational and overall rotational modes of the molecules, in a mechanism called dipolar polarization, and represented by the microwave complex permittivity.

1.2 Polarizations

When a dielectric material is immersed in an alternating electromagnetic field $\vec{E}$, it tends to orient its dipoles $\vec{p}_i$ accordingly.

If the material is isotropic ($\vec{P}$ is in the same direction as $\vec{E}$), homogeneous ($\vec{E}$ results in the same amount of $\vec{P}$ throughout all the inside) and linear (*/P/* only directly proportional to */E/*), the applied electric field and the total polarization are related by:

$\vec{P} = \sum_i^N \vec{p_i} = (\varepsilon_r - 1)\varepsilon_0 \vec{E}$.

This reorientation in general is not instantaneous, since the movement of all kind of dipoles encounter some resistance. Therefore the total polarization $\vec{P}$ takes some time to arrive to its final steady regime.

The complex dielectric permittivity ε_r is the microscopic intrinsic property of the material expressing how fast its dipoles change into the new orientation. Consequently, it is frequency dependent, and can be written in the form:

$\varepsilon_r^*(\omega) = \varepsilon_r'(\omega) + j\varepsilon_r''(\omega) - j\frac{\sigma(\omega)}{\omega_o\varepsilon_o}$

The real part expresses the energy stored in the material, the two imaginary parts represent the energy dissipated, in particular the first by the movement of reorientation of the dipoles in the field (responsible for dielectric heating), the second the losses for conductivity of the free charges (responsible for Joule's eating). Both the imaginary terms contribute to the loss, which are expressed by: $\tan\delta = \frac{\omega\varepsilon_r''(\omega)+\sigma(\omega)}{\omega\varepsilon_r'(\omega)}$; yet, it is impossible to distinguish the two mechanisms, and most dielectrics have $\sigma \ll \omega\varepsilon_r''(\omega)$.

The particular form of $\varepsilon_r', \varepsilon_r''$ and the characteristic time constant associated to the reorientation process, called relaxation time, depend on the frequency of the electric field applied. Indeed, at different frequency regimes, different polarization phenomena occur (see Figure 1-1 for a comprehensive overview):

1) dipolar polarization has a relaxation time within the GHz frequency range, and it is due to the reorientation of the dipole moments naturally present in polar molecules, or induced. It is a process at single relaxation time, described by a Debye first order relationship between ε_r', ε_r'' and ω:

$$\varepsilon_r' = \frac{\varepsilon_0 - \varepsilon_\infty}{1 + (\omega/\omega_0)^2} + \varepsilon_\infty;\ \varepsilon_r'' = \frac{\varepsilon_0 - \varepsilon_\infty}{1 + (\omega/\omega_0)^2} \cdot \frac{\omega}{\omega_0}$$

   Since generally the dipoles interact with each other, in heterogeneous materials there are several characteristic times; the permittivity is often described by the overall effects of these relaxation, as:

$$\varepsilon_r^*(\omega) = \varepsilon_\infty + \sum_i \frac{(\varepsilon_0 - \varepsilon_\infty)_i}{1+\left(j\frac{\omega}{\omega_0}\right)^{1-\alpha_i}} + j\frac{\sigma(\omega)}{\omega_o \varepsilon_o},$$

   where *i* is each relaxation. The exponent was generalized by Cole and Cole as 1-α, with $\alpha \in [1,0)$. The higher α, the broader the relaxation peak.

   In tissues, water dipolar relaxation is the dominant effect at microwave frequencies. Pure bulk water undergoes to a nearly single-time constant relaxation centred at 20GHz at room temperature and 25GHz at 37ºC, whereas water associated with protein surfaces has a lower relaxation frequency and contributes noticeably to the dielectric dispersion at frequency near 1GHz.

2) atomic and electronic polarizations have relaxation times respectively at infra-red and visible light; they are due to

the periodical re-displacement of atoms of opposite charge in a molecule or of the electron cloud respect the nucleus in a single atom. Since the involved masses are very light the processes have very short relaxation times. They are described by a second order relationships between ε_r', $\varepsilon_r''$and ω.

Biological materials such as cells suspensions and tissues are essentially heterogeneous. In such cases, two more polarization mechanisms, at frequency lower than that of dipolar polarization, occur:

3) Interfacial polarization, with relaxation times within the RF regime; it is related to charges appearing at the interfaces within two different regions, and it is the dominant effect across the cell membrane: at frequency minor than 100kHz the membrane acts like a capacitor, insulating the cytoplasm from the external medium. Therefore, the current does not penetrate inside and the cell appears as poorly conductive compared to the surrounding electrolytes. Instead, at frequencies between 1-100MHz, the current flows without restrictions throughout the cell, as the cell membrane shielding effect is shortcut.

4) Counterion polarization has relaxation times at few Hz, and it is associated to the diffusion of the ions of the electric double layers adjacent to charged surfaces, into the bulk solution.

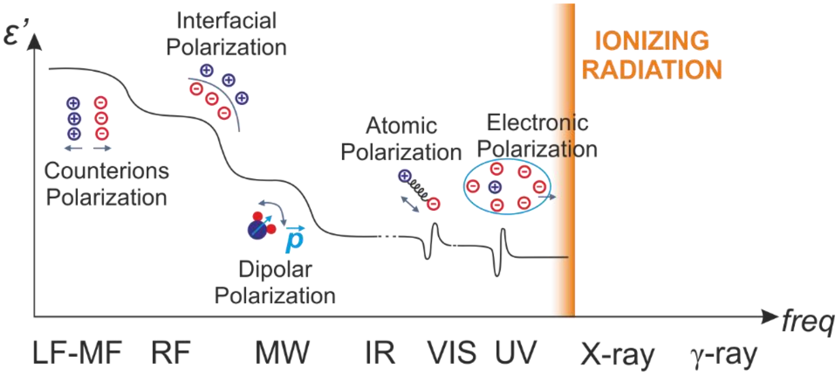

Figure 1-1 Schematics of the variation of the real part of the permettivity of a cell as a function of frequency, with the associated polarization mechanisms. (Adapted from [97])

2. SCANNING MICROWAVE MICROSCOPY

In this chapter I briefly outline the principles of Near-Field Scanning Microwave Microscopy (NF-SMM), which, as mentioned in the introduction, is a promising technique to characterize the dielectric response of samples at microwaves with high spatial resolution. Next, I review concisely the state of the art of SMM measurements in biological samples.

Finally, I focus on the particular implementation of the technique used for this work of thesis, namely an AFM-based SMM. This setup acquires simultaneously from the sample images of topography and complex microwave reflection parameter S_{11}. This latter, after a proper calibration procedure, can be related to the impedance. Since the samples analysed in this work of thesis resulted to be non-lossy, the impedance images are, in fact, capacitance images, from which the specific dielectric polarization of the sample can be retrieved.

2.1 General principles of scanning near-field microscopy

Since the invention in the 17th century of the optical microscope, microscopy techniques have advanced to the point of using wavelength of the EM spectrum other than visible light (such as microwaves in SMM), particles other than photons (such as electrons in STM, TEM, SEM), and principles other than transmission/diffraction of electromagnetic waves (such as Van der Waals forces in AFM). However, most of our knowledge about matters has come and still comes from the interaction with EM fields.

Traditionally, using electromagnetic waves involved gathering simultaneously all the information resulting from the interaction between the imaged object and the wave propagating from a source. In this case the resolution is limited by the Abbey's diffraction limit, which is the minimum angular separation between two points to be distinguished: $d \approx 1.22\frac{\lambda}{l}$, where l is the diameter of the lens (aperture) and λ is the wavelength of the radiation used. For microwaves, this would limit the resolution to the order 10^{-2} m.

Abbey's limitation can be overcome employing the evanescent waves, i.e. imaging in the near-field region of the EM field. In such condition, the signal is acquired only from a small volume of the sample at one time. Large area images can be then built up by scanning the wave source with respect to the imaged object, and reconstructing the localised measurements pixel-by-pixel (or point-by-point).

In near-field microscopy, the source of the EM radiation is usually the microscope probe, which acts as a very short ($D \ll \lambda$, where D is the dimension of the antenna and λ is the wavelength of the radiation) emitting-receiving antenna. The space invested by the radiation is divided in: near-field zone (static), intermediate zone (induction) and far zone (radiation) [14]. In the near-field region, the electric and magnetic components oscillate in time but do not propagate in the space, thus do not propagate energy: rather, this is brought back and forth in the vicinity of the tip and therefore stored as reactive. The component waves (or fields) dominating in the NF are called evanescent waves. These decay quickly with the distance r from the source, with r^{-2} or higher power (depending on the dipole order of the antenna), and define the extent of the near-field region as a depth equal approximately to D. Moreover, since the amplitude of the evanescent waves is proportional to D, and the amplitude of the far field components proportional to D/λ, for small antennae, the evanescent fields have a much greater magnitude.

NF-SMM consists in scanning the tip in contact or really close to the sample, at a distance $d \leq D \ll \lambda$ [15], therefore within the near-field region. Thus, the EM fields penetrate inside the sample in volume of approximately D^3.

The sample represents an impedance discontinuity for the EM waves, and alters the reactive energy stored in the near-field. This changes the electromagnetic response of the detection systems, in particular the impedance, and affects parameters like reflection and transmission coefficients, quality factor and resonant frequency. The variation of these parameters is recorded, and can be used to calculate the sample´s permittivity via some analytical model, simulation, or calibration standards. Thanks to the small size of the microscope probes *D*, high spatial resolution can be achieved efficiently (little radiated energy), and the diffraction limit overcome.

It is important to stress that the impedance measurement performed in this way are not absolute values but variation with respect to the unperturbed situation (far from the sample, or in absence of the sample).

Synge [16] was the first in 1928 to theorize the use of NF to increase the resolution of optical microscopy techniques, and indeed most of the scanning microscopies in use nowadays rely somehow on evanescent waves: STM uses the interactions between near-field electronic wavefunctions of tip and atoms to image the surface of conductive samples. SNOM uses evanescent optical waves to images variations in the refractive index, or in the wave absorption [17].

Concerning SMM, the first demonstration of NF use at microwave frequency were done independently by Freit [18] in 1959, and Soohoo [19] in 1962, to study ferromagnetic resonance. Yet, for most of the subsequent development not devoted to magnetic materials [20], it is Ash and Nicholls [21] who are more exactly to be credited for the break of the diffraction limit at GHz frequency, in 1972. They used 10 GHz microwaves (λ=3 cm) to image an aluminium test pattern deposited on a glass slide, achieving a spatial resolution $\lambda/60$. Nowadays, much higher resolution can be achieved, for instance Tabib-Azar et al. [17] report for their setup a resolution of λ/750000, i.e. 40nm at 10GHz.

2.2 Resolution and sensitivity

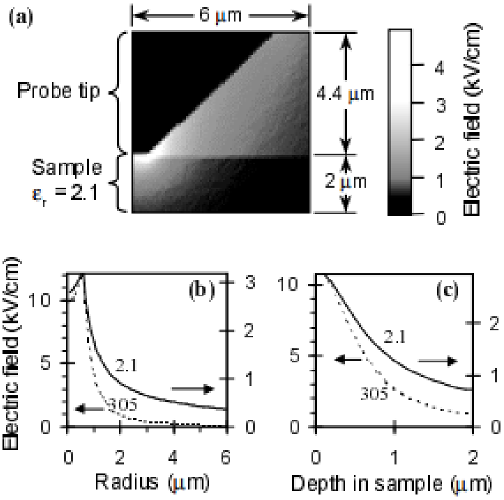

Figure 2-1 (a) Finite element calculation of the electric field near a probe of dimension D=1.2µm. Electric field magnitude as a function of radial distance (b) and depth (c) in the sample, for a sample with permittivity ε_r=2.1 and 305. (Reproduced from [22])

As discussed above, the probe size D is the parameter which most governs the spatial resolution (both lateral and vertical) of a NF scanning microscope: the smaller it is, the better is the resolution. However, as the probe becomes smaller, smaller signal are measured, whereas the background noise ascribed to the electronic components remains constant. Therefore, the ideal dimension is a tread-off between resolution and sensitivity.

Different probe configurations have been proposed to maximize the resolution of NF-SMM; the most common ones are detailed in section 2.2.1.

Furthermore, the resolution is, to a lesser extent, also a function of the dielectric characteristics of the sample: high permittivity concentrates the fields at the probe end, therefore focuses the EM fields. To illustrate this fact, Steinhauer et al. [22] (Figure 2-1) calculated the electric field as a function of radial distance from the centre of the probe (in this case coaxial waveguide ending with a tip of diameter D=1.2µm), and vertical into the sample, for two samples with different homogeneous permittivity ε_r=2.1 and 305). We can see how vertical and lateral spatial resolution are in the order of D. Moreover, for higher permittivity, the fields are more highly concentrated, and fall off more quickly away from the probe, indicating that the spatial resolution of the microscope is higher for highly polarizable materials.

The sensitivity instead depends, apart than D, also on the probe-sample distance: large probe-sample distance attenuates the interaction, because the NF is dispersed in air, therefore in order to maximize the detection, the probe must be kept as close as possible to the sample.

For the purpose of this work, it is important to emphasize that some authors [23] make a distinction between qualitative and quantitative spatial resolution. Qualitative spatial resolution is related to imaging, and is defined as the smaller contrast feature observable on a sample with very different dielectric permittivity (for instance metal/oxide microstripes). Quantitative spatial resolution is related to metrology, and is defined as the maximum volume of the material affecting the probe response, i.e. the volume storing the 100% of the energy of the probing field. It follows that the imaging resolution power is always smaller than the quantitative resolution power. As will be thoroughly discussed in the following chapters, this differentiation is important for quantitative imaging with SMM.

2.2.1 SMM probes

The probe is a small antenna compared to the operating wavelength. It delivers the microwave signal to the sample and measures the impedance within the NF region. Several probes' configurations have been developed, in order to enhance the local tip-sample interaction, maximize the resolution and minimize reflections and energy losses from source to the sample.

The basic classification is between aperture-based and apertureless probes.

Aperture probes were the first to be developed, for instance they were the type used by Ash and Nichols for their demonstration. The basic principle is to confine the lateral extent of the near-field interacting with the sample by means of a sub-wavelength aperture, and in this respect they resemble the optical fibres of SNOM. Cavity resonators with aperture (Figure 2-2a), open ended coaxial waveguides (Figure 2-2b) and parallel strip lines (Figure 2-2c) are examples of this kind. Aperture probes actually limit the probing volume to about the size of the aperture *D*, and for this reason they have a high (metrological) resolution. Yet, they are in general larger than apertureless probes, and the geometrical constrains limit the possibilities of downscaling; for this, the (imaging) resolution results anyway rather low.

Apertureless probes instead leave the EM spread through a larger portion of the sample, but enhance the local interaction by means of a sharp ending of radius *D*, which concentrates the EM field. Examples of this kind of probes are the coaxial waveguide with a sharpened tip (the most commonly used type in the literature, Figure 2-2d), the highly conductive AFM probes (Figure 2-2e) and the microstrip waveguide (Figure 2-2f). These kinds of probes gather much more signal from the sample, to the point that not only the near-field microwave community, but also the near-field optical community is gradually moving towards apertureless probes (apertureless SNOM), i.e. to the use of a field-enhancing feature

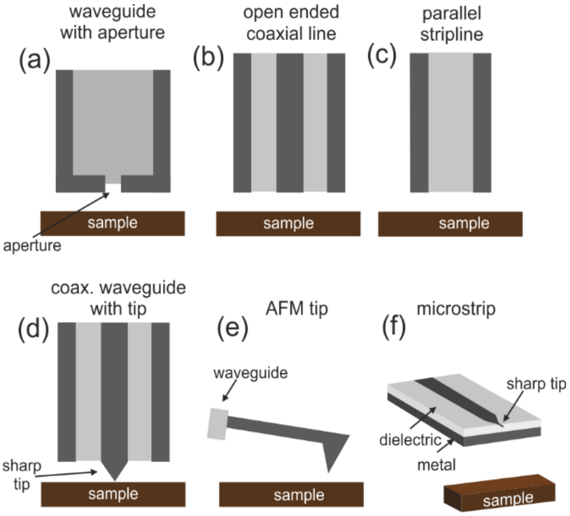

Figure 2-2 Schematics of the main types of SMM probes: (a) aperture in a waveguide, (b) open-ended coaxial waveguide, (c) parallel strip transmission line, (d) coaxial waveguide ending with a sharpened tip, (e) AFM tip, (f) microstrip. Adapted from [15].

rather than an aperture which restricts the NF volume.

In the case of AFM probes, in particular, it is possible to push the limit of the (imaging) resolution, because the size of an AFM tip can be as small as few nanometres, although in general a large background signal is present and limit the metrological resolution (Figure 2-3). In fact, the metrological resolution of apertureless probes, such as AFM tips, is of the order of few hundreds microns and not nanometres (the size of the probe apex) as it is governed by the length scale of the entire AFM cantilever and chip holder components: these parts interact long-range with the sample, and thus invest a much larger volume of it. The electrical coupling results in a capacitance stray contribution, which often amounts to the largest part of the impedance measured. Therefore, removing the non-local stray interaction is crucial to be able to quantify the local nanoscale dielectric properties.

To this aim, electrically shielded AFM probes have been developed [24, 25], where the cantilever and the tip cone are covered by a dielectric layer and a metallic layer. The metallic layer is set to the same electric potential of the sample substrate, so that the only part interacting with the sample is the tip apex, as the stray contribution is eliminated. In such way, the probe becomes sensitive only to the local properties of the sample. Electrically shielded probes are certainly an improvement for AFM-based SMM, but they became only very recently commercially available: the design and fabrication process present difficulties, due to the complexity of a microwave AFM probe and to the coupling of two materials (dielectric and metallic shield) with different thermal expansion,

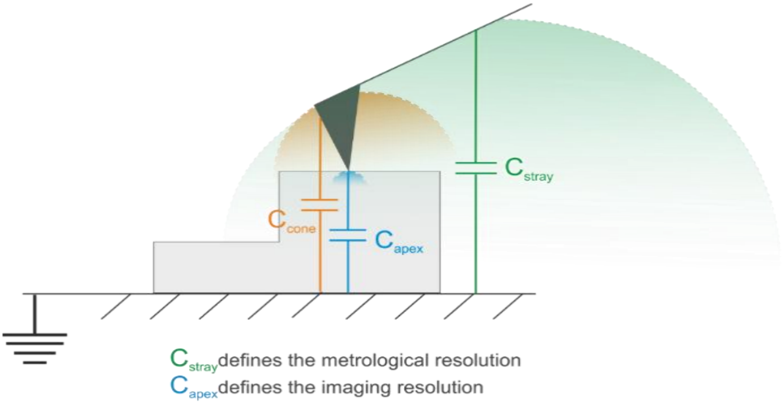

Figure 2-3. The capacitive couplings between a conventional conductive AFM probe and the substrate comprehend contributions from the tip apex, cone and cantilever (stray). The circular regions qualitatively represent the extent of the interaction volume, which controls the metrological and imaging resolution

which induces mechanical stresses.

2.2.2 Distance control mechanisms

Since the impedance signal measured depends on the distance between probe and sample, one of the crucial issues of SMM measurements is to keep this separation small, to achieve high sensitivity, and well controlled all over the scan area, to achieve high accuracy.

Feedback loop mechanisms are needed to maintain a constant probe-sample distance. The most commonly used are based either on mechanical forces or electron tunnelling, and both enable the simultaneous recording of the sample topography.

As for the firsts, Van der Waals/contact forces and shear forces are the most used, and are at the basis respectively of AFM-combined

SMM and tuning-fork-combined SMM. In AFM-SMM systems, such as the one used in this work, the Van Der Waals and contact forces cause the deflection of the cantilever supporting the AFM tip, and the deflection is monitored by mean of a laser beam projected on the top. In other modes, the probe is made oscillate mechanically at its resonance frequency; the forces dampen the amplitude of oscillation, and this change is monitored optically [26].

In tuning-fork-combined SMM too, the tip oscillate at its resonance frequency, but the shear forces are responsible for the alteration of the resonance, which is monitored with a quartz crystal tuning fork [27, 28].

For conductive samples, STM-based systems can be implemented. When the STM tip is biased with a voltage and it is brought at a few nanometres distance from the sample, an electron tunnelling current can be measured. Since the tunnelling current decays exponentially with the distance, this mechanism allows to control the tip vertical position with nanometric precision [15, 29].

2.3 SMM applications to biological samples: state of art

As mentioned in the introduction, nanoscale imaging of single cells or macromolecules using microwaves has a great appeal for medical and biological applications, for the two fundamental characteristic of GHz radiation: energy below the ionization potential and penetration under the cell membrane. This means that images of single cell’s components, where the contrast is given by their different polarization, could be obtained without damaging the cell or affecting its physiology. Furthermore, SMM *per se* requires low power to deliver the microwave field to the samples, which suggests a negligible sample heating during the scanning. For this characteristic, SMM can be potentially used not only to obtain qualitative or quantitative maps of the dielectric polarization of the single cell or macromolecule, but also to investigate the possible microthermal effects at physiological level. For these reasons it is no wonder that several groups, since the late '90s, have applied tailored home-made configurations of SMM to investigate biological specimens.

Tabib-Azar and co-authors [17] used for instance a microstrip resonator coupled with a fibre-optic sensor for distance monitoring, to obtain microwave images of different tissues at 1GHz, with resolution 400nm. Human cortical bone cuts images were notably combined with scanning acoustic microscopy, in order to investigate at the same time the mechanical properties. Also, they imaged a tooth cross-section and a balsa wood surface, for which they ascribed the contrast variation in the evanescent microwave image to the amount of moisture content.

Farina and co-workers [30] investigated the subsurface capabilities of SMM, imaging mouse muscular cells grown on top of carbon nanotubes (CNT) and fixed in formaldehyde. Their setup consists in AFM-based SMM, where the nanometric platinum probe is connected to the microwave source and measurement system throughout a coplanar waveguide. The electrical maps, obtained at 5-6GHz, revealed an elongated structure with diameter 200-300nm, which they identified as a carbon nanotube inserted in the cellular matrix. Yet, I would argue that this feature is present also in the topographic image simultaneously recorded~~,~~ therefore it could be also an effect of topography crosstalk (see chapter 3). The authors also developed an alternative setup, based on STM, to work in physiologic conditions, although STM feedback is challenging due to the small currents between tip and biological specimens.

Park and co-workers [31] used an open ended coaxial resonator with a micrometric tip protruding from the aperture to monitored the change in frequency shift and quality factor at 1.5GHz for different kinds of cells. For *yucca filamentosa* epidermal cells they ascribed the changes in contrast to the different water content of cell wall and cytoplasm, whereas in osseous tissue, because of their higher water content, they could spot the blood vessels. The electrical signal obtained was not converted into impedance and again, it might happen that part of the observed contrast is rather due to changes in tip-sample distance (topography crosstalk) than to the different dielectric properties of the biological compartments.

Lee and co-authors [32] tested the applicability of SMM imaging to multiplexed DNA sequence analysis, leveraging on the label-free characteristic of the technique. They measured the reflection of several DNA microarray of 40μm diameters, at about 4GHz, using an AFM tip with a tuning fork feedback system. They reported a good correlation of SMM maps and fluorescence images for 60mer DNA oligonucleotides, with an excellent sensitivity to the presence of DNA: .01strands/μm^2 versus the .05 fluorophores/μm^2 of the fluorescence techniques. They also imaged 10mers homonucleotides, and found that guanine bases have more contrast than the other bases, but knowledge about the level of hydration and base orientation is needed to claim that this is an effect of molecular polarization.

The studies reviewed above represent an important contribution to shed light onto the potential biological applications of SMM, but are limited to the observation of the parameters used to monitor the interaction (may they be shifts in resonance frequency and quality factor, or complex scattering parameters) and do not proceed further with their conversion into probe-sample impedance. To date, only three other groups have worked in this direction, Lai and co-workers, Kalinin and co-workers and Tuca and co-workers.

Lai and co-authors [33] used a new configuration consisting in two transmission lines, one for excitation and one for detection. They used aluminium coplanar waveguides micropatterned on a cantilever chip and measured the in-phase and out-of-phase sensed signal, which, after proper calibration, can manifest the complex impedance of the measurement. Among other samples, they proved the capability of their setup at 1GHz on a compound eye and an antenna lobe of a *Drosophila* (fruit fly), for which they precise that the contrast in the image is given by variations in both sample topography and electrical properties.

Kalinin and co-authors [34] demonstrated the capability of SMM subsurface tomography by imaging polystyrene beads, electrodes dendrites and yeast cells, immersed a liquid cell covered by a thin dielectric membrane (8-50nm). The setup consists in an AFM-based SMM, where a shielded probe is scanned over the dielectric lid in contact or intermittent mode. The reflection signal measured at 3-8GHz is converted into capacitance and conductance with a calibration kit. The key intuition of this work is that only the sample and not the tip is immersed in the liquid, which simplifies the conversion and the interpretation of the results. Moreover, provided that the membrane deflection during the scans remains insignificant, no topography crosstalk effect is present, and the impedance contrast variation are to be ascribed only to the dielectric inhomogeneity of the samples under the surface. The impedance contrast reveals the different permittivity of the sample with respect to the liquid medium, thus enabling to distinguish for instance between dielectric or metallic parts of the samples. The probing depth varies depending on the tip diameter, membrane thickness and permittivity of liquid and samples, meaning that by changing the tip dimension it is possible to obtain tomography images. The authors report a lateral resolution of 50nm with a tip radius of 50nm.

Tuca and co-workers [35] used instead the same setup and calibration method I used in this thesis, to study the impedance of *E.coli* and CHO cells in air condition, at different environmental humidity levels and frequencies. For *E.coli* they did not observe any conductance at all at any humidity level, in agreement with results at lower frequency [25] and with the results of this thesis (chapter 6). For CHO cells instead they found that the conductance behaves qualitatively similarly to the one of bulk water: fixing the humidity at 30% RH, a higher conductance is observed at higher frequency

(2GHz and 18GHz), and fixing the frequency at 19.9GHz, higher conductance is observed at higher humidity (2% and 60%). Again in this case part of the contrast could be affected by topography crosstalk artefacts. As it will be detailed in the next chapter, the topography crosstalk plays a major role in the formation of the contrast in images of samples exhibiting heights of hundreds of nanometres and acquired in intermittent and contact modes, so its removal is essential to highlight the intrinsic electric properties of the sample.

.

2.4 SMM setup and calibration used in this work of Thesis

The NF-SMM setup used in this work consists in a 5600LS Keysight AFM combined with a Keysight E8362B 20GHz vector network analyser (VNA). The AFM tip is made in highly conductive solid platinum, not shielded, and is connected to the VNA by a transmission line consisting in coaxial cables. In Figure 2-4 it is depicted a sketch of the operational principles.

The AFM feedback system (laser + photodetector + piezo stage) controls the probe’s scanning and allows to obtain topography

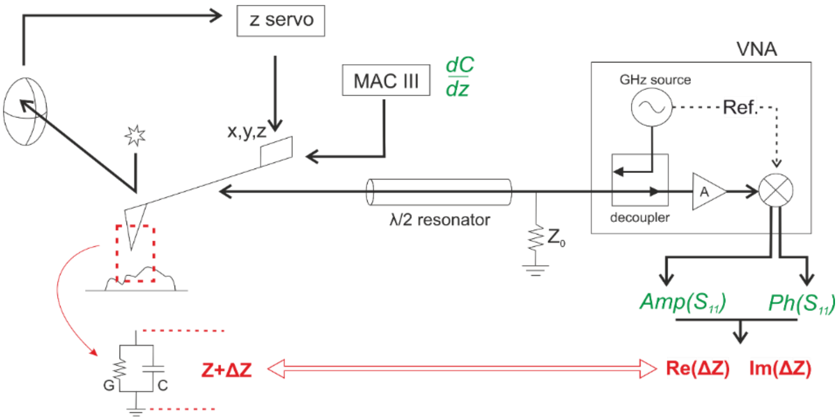

Figure 2-4 Schematic of the AFM-based SMM setup used for this work

images of the sample in the most common AFM modes: contact, intermittent contact and two pass lift mode.

At the same time a microwave signal is generated at a single frequency by the VNA, it travels throughout a transmission line and arrives to the probe end, where it creates an EM field concentrated around the tip apex. When the sample is in proximity of the tip, its complex impedance produces an electrical alteration in the near-field around the tip apex.

From the point of view of transmission lines theory, the microwave network includes all the components from the VNA to the tip-sample interface. For this, the impedance measured by the VNA is the one of the tip and the region of the sample within the near-field. The impedance of the tip-sample system can be modelled via lumped elements as a resistance and a capacitance in parallel.

VNA and transmission line have both characteristic impedance Z_0=50 Ohm. The tip-sample system instead can have whichever impedance, in general much higher. Thus, there is an impedance mismatch at the end of the transmission line, which causes the incident microwave signal to be partially reflected back towards the VNA. The amount of reflected signal is proportional to the impedance mismatch, therefore carries information on the dielectric response of the sample.

In the reflection mode measurements used in this work of thesis, the VNA compares the signal reflected back from the device under test (DUT, *i.e.* probe-sample system) with the stimulus signal, and returns this comparison in dB, as the complex scattering parameter S_{11}[1]:

$$\mathrm{S}_{11}[dB] = 20\log\Gamma = 20\log\left(\frac{V_{ref}}{V_{in}}\right) = 10\log\left(\frac{P_{ref}}{P_{in}}\right),$$

where $\Gamma = \mathrm{s}_{11}$ is the reflection coefficient, related to the complex impedance of the sample, Z:

$$\Gamma = \mathrm{s}_{11} = \frac{Z-Z_0}{Z+Z_0}.$$

When no DUT is present, $Z = \infty$, therefore $S_{11} = 0\mathrm{dB}$ and $s_{11} = +1$ (total reflection), whereas in case that the DUT has the same impedance of the network ($Z=Z_0$=50 Ohm, perfect matching load), the reflection is null because the full wave is adsorbed by the tip-sample system: $S_{11} = -\infty$ and $s_{11} = 0$. This latter condition means that only load impedances of about Z_0 can be measured with high precision, as it is shown in Figure 2-5: load impedance around 50 Ohm fall in the linear region of the reflection coefficient, and can be

---

[1] Note that the S-parameter of transmission lines, s_{11}, is actually equal to Γ, but it is often called and treated as a return loss with a positive sign, i.e. as its variation in dB. In fact, in our case the output of the VNA is more precisely a *variation* of the scattering parameter. To avoid confusion, we call this S_{11}

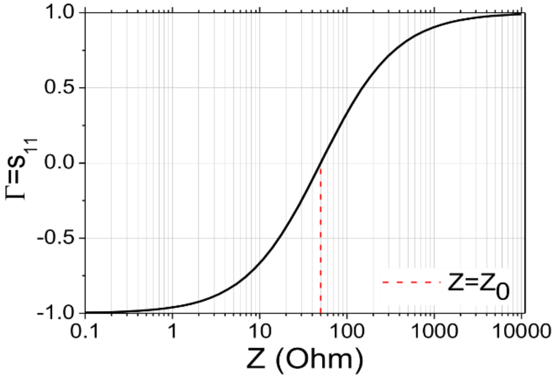

Figure 2-5 Reflection coefficient behaviour as function of load impedance. The areas of open circuit and shortcut offer low sensitivity to the change in impedance, as the reflection coefficient saturates, whereas around s_{11}=0, i.e. Z_0=50Ohm, it is achieved the best sensitivity.

measured with better sensitivities with respect to much higher or lower impedances, where the reflection coefficient saturates.

Because of the characteristic nanometric dimension, the impedance of the tip-sample system is order of magnitudes larger than Z_0. In order to reduce it, and thus achieve the suitable sensitivity, a matching network is inserted in the transmission line. This consists in a half-wavelength coaxial resonator and a 50 Ohm shunt impedance put in parallel to the tip-sample. When the tip is in contact with the sample, the matching network creates a pattern in the S_{11} frequency response, where amplitude minima occur at frequencies corresponding to the half wavelength of the transmission line, in our case almost every 1GHz being the transmission line of 9cm long. In other words, at frequency spaced almost 1GHz, the impedance of the system tip-sample matches the characteristic impedance, and the VNA and the load are basically a resonant structure.

Several signal detection methods can be used to monitor the change of S_{11}, as it can be seen from Figure 2-6.

A typical way, used also in our setup, is to fix a frequency maximizing the signal and to follow the changes of S_{11} amplitude and phase. Otherwise, one could detect the shift in resonance frequency brought by the probe-sample impedance, and use a feedback system to maximize the amplitude of the reflection [36], varying either the source frequency or the tip-sample distance [37]. We perform the measurement at fixed frequency in proximity of one of the sharp notches, where the slope of the S_{11} plot is the steepest, and therefore maximum sensitivity is achieved. Generally, notches around 20GHz are the deepest and give better sensitivity. In this way, capacitance changes on the order of aF can be measured.

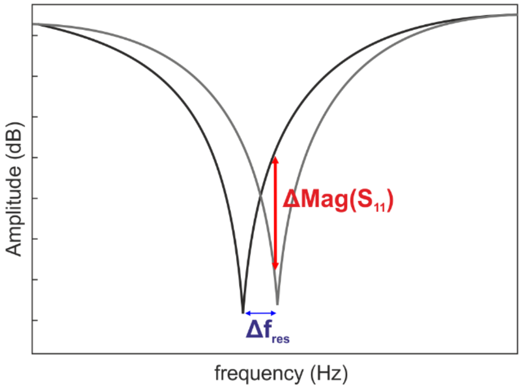

Figure 2-6 Methods for the detection of changes in the amplitude of the reflection coefficient: when an alteration of the reflection occurs, the S_{11} plot passes from the grey to the black line. This change can be tracked either by comparing the amplitude at a fixed frequency close to the notch (maximum transmission), or following the notch amplitude by detecting the shifts in frequency

To sum up, by measuring S_{11} as the tip is scanned over the sample, at the same time with topography, one obtains images of the electrical response of the sample, at microwave. Then throughout a calibration procedure, S_{11} is converted into impedance variations of the tip-sample system. It is important to stress that it's not possible to measure strictly the absolute impedance of just the sample, but only *variations of the tip-sample impedance.* Nonetheless, provided that the tip geometry doesn't change much during the scans and the tip-scan distance remains constant, these variations represent, in fact, variations of the impedance of the sample.

2.4.1 Calibration

Figure 2-7 represents the sketch of a one-port transmission line, ideal (left), and real (right). This latter takes into account the intrinsic errors of the network in reflection measurements, namely:

- directivity (e_d): expresses how well the directional coupler inside the VNA can actually separate the signal going in two opposite directions, from and to the load (tip-sample).
- source-load mismatch (e_s): accounts for possible reflections due to untighten connections all through the transmission lines
- reflection tracking (e_{rt}): expresses how precisely the reflected signal is measured at the same frequency of the sent signal wave.

e_d, e_s, e_{rt} are complex quantities. Subsequently, the measured reflection, $\mathrm{s}_{11,m}$, is not just given by the DUT reflection, $\mathrm{s}_{11} = \frac{Z-Z_0}{Z+Z_0}$, but it is affected by all these error sources:

$$s_{11,m} = s_{11} \pm \left[e_d + e_s s_{11}^2 + s_{11}\left(1-e_{rt}\right) \right] = s_{11} + e_{rt} \frac{s_{11}}{1- s_{11} e_s}$$

Equation 2-1

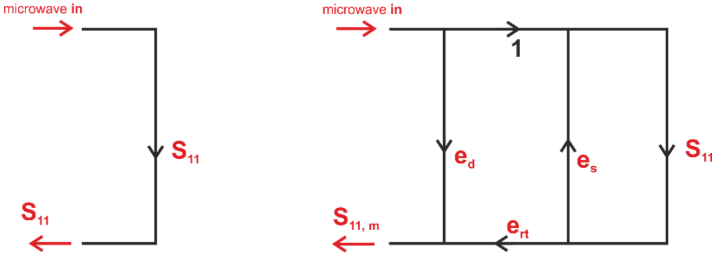

Figure 2-7 Calibration parameters in the ideal (left) and real (right) conditions of the reflection equivalent circuit, where in fact the signal measured $s_{11,m}$ is not just given by the reflection from the tip-sample, s_{11}, but is also affected by spurious effects present in the network: directivity (e_d), source-load mismatch (e_s) and reflection tracking (e_{rt}).

In order to convert the measured maps of $S_{11,m}$ into impedance variation images, it is needed a calibration procedure to determine the error parameters, which implies to measure three known reference impedances.

The most straightforward approach was proposed by Huber et al. [38], who used a calibration kit consisting in micrometric gold pads of various sizes over a SiO_2 staircase structure, on a highly doped silicon substrate. The impedance was modelled as two capacitors in series (one for the capacitor itself, i.e., the oxide layer, and one for the background substrate capacitance), and related to the measured S_{11} by a linear relationship: $C_{tot} = \alpha^* |S_{11,m}|$. The error parameters (inside α^*) were determined by fitting the S_{11} values measured on the pads with control measurements made with an external capacitance bridge.

The limit of this approach is the low accuracy: it presents the inconvenient that one must substitute, in the microscope, the calibration kit with the DUT, and this exchange in fact can modify the stray capacitances to the point that the calibration almost loses its validity.

We applied here the calibration procedure described by Gramse et al. [39], which on the contrary, works *in situ*, and doesn't require a calibration standards kit. On the other hand, it requires a special gold nosecone which supports the AFM tip and connects it electrically to a low frequency source.

The method consists in applying to the AFM tip, together with the microwave signal at a single GHz frequency, an AC voltage at low frequency, $V(t) = V_0 \sin(\omega t)$, with typically ω=2kHz and V_0=3V The tip is approached on a single point of the highly conductive part of the sample substrate, and then one records, simultaneously as a function of tip-substrate distance z, the complex reflection parameter $S_{11,m}(z)$ and the change of the cantilever oscillation amplitude, due to the electrostatic force, at the double harmonic, $A_{EFM,2\omega}(z)$.

The module of the amplitude of the electrostatic force microscopy at the second harmonic does not depend on the surface voltage of the sample, and is related to the capacitance gradient by an equilibrium condition between the work done by the electrostatic force to bend the cantilever from the equilibrium position far from the sample, z_0, and its elastic energy contrasting the bending:

$A_{EFM,2\omega}(z) = \frac{1}{4k}\frac{\partial C}{\partial z}V_0^2$.

Therefore the capacitance variation can be obtained from the EFM measurements by integration of the inverted formula above:

$$\Delta C_{EFM}(z) = \int_{z_0}^{z} \frac{\partial C}{\partial \tilde{z}}\, d\tilde{z} = \int_{z_0}^{z} \frac{4k\, D_{EFM,2\omega}(\tilde{z})}{V_0^2}\, d\tilde{z}$$

Since the substrate is lossless (highly conductive), the equivalent impedance in Figure 2-4 is purely capacitive:

$$\Delta C_{EFM}(z) = \frac{1}{j\omega \Delta Z(z)}.$$

Equation 2-2

The three complex error parameters can be found by fitting Equation 2-1 with Equation 2-2. They remain valid for all subsequent measurements (if the tip dimensions do not vary significantly), and can be used to obtain images of calibrated impedance variation.

Combining these impedance images with detailed information about tip and sample geometry, and separation distance, one can root back to maps of the dielectric permittivity.

3. TOPOGRAPHY CROSSTALK REMOVAL FROM CALIBRATED SMM IMAGES

As we have seen in the previous chapter, the AFM-based SMM setup allows to obtain simultaneously topography and calibrated capacitance (and conductance) images of the sample.

One of the major difficulties of interpretation of the SMM capacitance images is the presence of parasitic contributions, such as stray and topography crosstalk. In particular, for 3D samples irregularly tall, such as cells, when the images are acquired with the AFM tip following the surface features of the sample, the topography crosstalk often accounts for the vast majority of the signal measured, and it can, in fact, mask the local dielectric response of the sample. Perhaps the most important contribution of my research to the SMM community and to the research group is the elaboration of a methodology to disentangle and remove the topography crosstalk contribution from the capacitance images acquired by SMM.

In this chapter I thoroughly describe the problem and the procedure theorized and implemented to remove it. This procedure enables to obtain new capacitance images free from parasitic contributions, and only related to the intrinsic dielectric response of the sample. Such images are therefore suitable for the quantification of the permittivity.

3.1 Topography crosstalk

With the AFM-based SMM detailed in chapter 2, the measurements are usually performed using commercial conductive non-shielded AFM probes in two of the most common AFM operational modes, contact mode or intermittent contact mode (from now in the text just intermittent). The advantages of these choices for irregularly tall samples, such as cells and bacteria, will be clarified further in the text. At this point, it is important to discuss the drawback

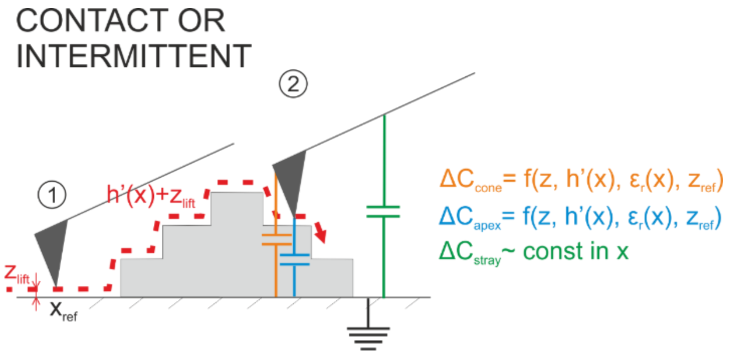

Figure 3-1 Capacitance contributions to the raw image for an AFM conventional non-shielded probe. The capacitance (variation) from point 1 to point 2 in images acquired in contact or intermittent mode is due to contributions from the tip apex, tip cone, and stray, where only the first two depend on the permittivity and tip-substrate distance..

associated to such imaging conditions: the presence of two main source of parasitic capacitance, namely stray and topography crosstalk capacitance contributions. Both are due fundamentally to the interaction of the probe with the substrate.

In section 2.2 it was pointed out that for non-shielded apertureless probes the capacitance images contain not only local information coming from the tip apex interaction with the sample (i.e. collected from a sample region scaling with the tip dimension *D*), but also from a stray contribution, i.e. from the coupling of cantilever and other tip supporting elements with the substrate, which involve a much larger region of the sample (multiples of *D*) and dominates at large distance from the sample. The stray is the major factor limiting the metrological resolution and must be eliminated for a quantitative analysis. One notable characteristic is that long-range interactions can be reasonably approximated to be independent from the local permittivity and topography, therefore the stray is almost constant all over the area scanned. On the contrary, the topography crosstalk is a local parasitic contribution. It is present in operational modes where the tip scans following the sample surface topography, such as in contact or intermittent. These modes are convenient for sample exhibiting height variations of hundreds of nanometres, such as cells, because the tip remains close to the sample surface in each point of the scan. Consequently, the local interaction between tip and sample is maximized, and so it is the signal (see the considerations in section 2.2). For this reason, the measurements presented in this thesis are acquired in such modes. Yet, the tip-substrate distance variations during the

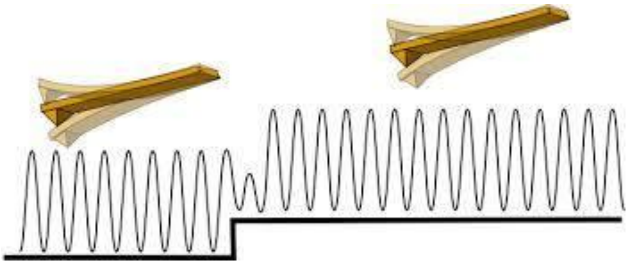

Figure 3-2 Amplitude modulated intermittent mode

scans induces spurious capacitance variations independent from the dielectric properties of the sample. In fact, this topography crosstalk, would be present even if the tip moved in air following the topography of the sample but in absence of it.

Figure 3-1a shows a sketch of the contributions present in the capacitance images acquired. As commented in section 2.1, the capacitance image is more properly a capacitance *variation* from a point far from the sample, but from now on in the text it will be referred just as capacitance.

The tip scans over the sample passing from the reference position 1 on the substrate (x_{ref}) to the generic position 2 above the sample (x). The total capacitance $\Delta C_T$is given by the sum of the tip apex, tip cone and stray contributions, calculated with respect to a reference point far from the substrate, z_{ref}. The first two are a function, apart from the geometrical parameters, of the local permittivity $\varepsilon_r(x)$ and tip-substrate distance $z_{lift}+h'(x)$. $h'(x)$ is the topography of the sample, obtained simultaneously with the AFM as result of the convolution of the sample geometry $h(x)$ with the tip apex. z_{lift} is the average tip-sample distance at which the tip scans, thus $z_{lift}=0$ in contact mode, and z_{lift} is in the order of the free oscillation amplitude in intermittent mode modulated at constant amplitude

(Figure 3-2).

This latter equivalence is a reasonable assumption, implying to consider the oscillation over the sample purely sinusoidal as the free oscillation and not damped by the presence of it. The change of the total capacitance is due then to both a change in the local permittivity and in the tip-substrate distance, for effect of the cone and apex interactions.

The raw capacitance contrast of the image from point 1 to point 2 is then given by:

$$\delta C_T\left(z_{lift},\, h'(x),\, \varepsilon_r(x)\right)=\Delta C_T\left(h'(x)+z_{lift},\ \varepsilon_r(x)\right)-\Delta C_T\left(h'(x_{ref})+z_{lift},\ \varepsilon_r(x_{ref})\right)=$$
$$=\ \Delta C_T\left(h'(x)+z_{lift},\ \varepsilon_r(x)\right)-\Delta C_T\left(z_{lift},\ 1\right)$$

Equation 3-1

Analogously, the topography crosstalk contrast from point 1 to point 2 when the tip moves in absence of the sample is given by:

$$\delta C_{T,CT}\left(z_{lift},\, h'(x),1\right)=\Delta C_T\left(h'(x)+z_{lift},\ 1\right)-\Delta C_T\left(h'(x_{ref})+z_{lift},1\right)=$$
$$=\ \Delta C_T\left(h'(x)+z_{lift},\ 1\right)-\Delta C_T\left(z_{lift},\ 1\right)$$

Equation 3-2

It is clear that by subtracting the topography crosstalk from the raw capacitance variation image, we obtain a new image where the contrast is only related to variation of the sample's permittivity and not of the topography:

$$\delta^2 C_{T,\mathrm{int}}\left(z_{lift},\, h'(x),\, \varepsilon_r(x)\right)=\delta C_T\left(z_{lift},\, h'(x),\, \varepsilon_r(x)\right)-\delta C_{T,CT}\left(z_{lift},\, h'(x),1\right)=$$
$$=\ \Delta C_T\left(h'(x)+z_{lift},\ \varepsilon_r(x)\right)-\Delta C_T\left(h'(x)+z_{lift},\ 1\right)$$

Equation 3-3

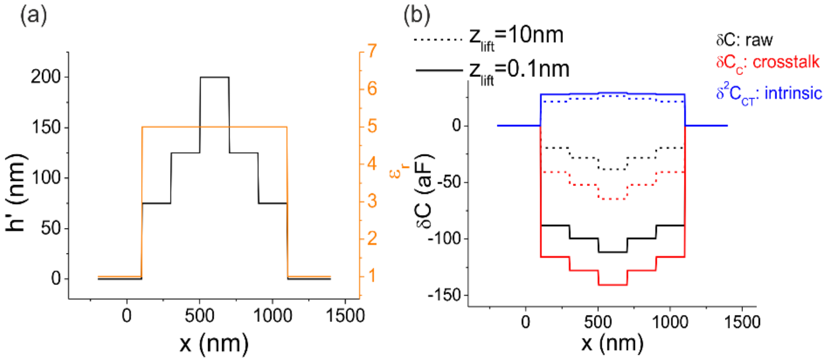

Figure 3-3 Capacitance contrast for a homogeneous sample, (a) Topography and permittivity of a hypothetical sample with heterogeneous dielectric properties. (b) raw (black), crosstalk (red), intrinsic (blue)capacitance contrast profiles, calculated with respectively Equation 3-1, Equation 3-2 and Equation 3-3 combined with Equation 3-4, setting z_{lift}=0.1nm (contact) and z_{lift} =10nm (intermittent). The closer the tip scans to the surface, the larger is the contrast recorded, in all cases. The parameters of the calculations are: tip radius R=300nm, tip half angle θ=10º, k_{stray}=0.03aF/nm, cone height H=80µm, z_{ref}=3µm

The three contrasts are depicted in Figure 3-3, for the case of a hypothetical sample dielectrically homogeneous (Figure 3-3a, orange line) but with thickness varying from 75 to 200nm (Figure 3-3a, black line). For this theoretical example, we calculated the capacitance variations using the formulae for a laterally infinite thin film, in which the sample thickness is smaller and the lateral dimensions are larger than the tip radius [40]. In such conditions, the overall capacitance can be expressed as sum of apex, cone and stray contributions [40]:

$$\Delta C\left(z,z_{ref},h'(x),\varepsilon_r(x)\right)=\Delta C_{apex}+\Delta C_{cone}+\Delta C_{stray}=$$
$$=C_{apex}\left(z,h'(x),\varepsilon_r(x)\right)-C_{apex}\left(z_{ref},h'(x),\varepsilon_r(x)\right)+$$
$$+C_{cone}\left(z,h'(x),\varepsilon_r(x)\right)-C_{cone}\left(z_{ref},h'(x),\varepsilon_r(x)\right)+C_{stray}(z)-C_{stray}(z_{ref})$$

with:

$$C_{apex}\left(z,h'(x),\varepsilon_r(x)\right)=2\pi\varepsilon_0 R\cdot ln\left(1+\frac{R\cdot(1-sin\theta)}{z+\dfrac{h'(x)}{\varepsilon_r(x)}}\right)+C_0$$

$$C_{cone}\left(z,h'(x),\varepsilon_r(x)\right)=$$

$$\frac{-2\pi\varepsilon_0}{ln\left[(tg\theta/2)\right]^2}\cdot\left[\left(z+\frac{h'(x)}{\varepsilon_r(x)}+R\cdot(1-sin\theta)\right)\cdot\ln\left(\frac{H}{+\dfrac{h'(x)}{\varepsilon_r(x)}+R\cdot(1-sin\theta)}\right)\right]+$$

$$+\frac{2\pi\varepsilon_0}{ln\left[(tg\theta/2)\right]^2}\cdot\left[R\cdot(1-sin\theta)+\frac{Rcos^2\theta}{sin\theta}\cdot ln\left(z+\frac{h'(x)}{\varepsilon_r(x)}+R\cdot(1-sin\theta)\right)\right]+C_1$$

$$C_{stray}(z)=-k_{stray}\cdot z+C_2$$

Equations 3-4

In the formulae, z is the tip-sample distance, therefore it was set $z=z_{lift}\sim0$ (contact), and $z=z_{lift}=10$nm (intermittent mode). The other parameters are: tip radius $R=300$nm, tip half angle $\theta=10º$, $k_{stray}=0.03$aF/nm, cone height $H=80$µm, $z_{ref}=3$µm, and C_0, C_1, C_2 are irrelevant constants.

Figure 3-3b represents in black the raw capacitance contrast, in red the crosstalk contrast and in blue the intrinsic contrast, calculated substituting Equations 3-4 in respectively Equation 3-1, Equation 3-2 and Equation 3-3. The continuous lines represents profiles calculated in contact ($z_{lift}\sim0$), and the dashed line the profiles calculated in intermittent mode at $z_{lift}=10$nm. As we can see, despite the topography variations, and unlike the raw profiles, the intrinsic contrast profiles for a homogeneous sample are fairly flat all over the sample area, being the dielectric permittivity uniform. In particular, the intrinsic contrast in contact mode reproduces qualitatively the dielectric characteristics with perfect agreement, whereas the contrast in intermittent mode present some small features due to the topography, although much reduced respect to the absolute raw profiles.

The intrinsic contrast has two useful characteristics: it is different from zero only on the parts of the images where the sample is present, i.e. where $\varepsilon_r(x)\neq 1$, and is free from stray contributions, as this is constant all over the profile and both in presence and in absence of the sample and thus it cancels out.

Also, as it can be seen in Figure 3-4 the intrinsic contrast in the

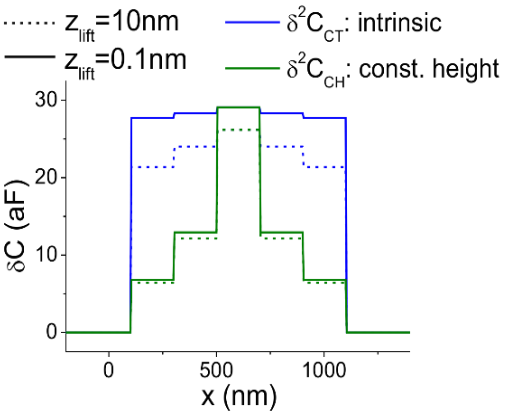

Figure 3-4. Intrinsic profiles in contact (blue continuous) and intermittent (blue dashed) mode, same as in Figure 3-3b, compared with the constant height profiles respectively at z_{CH}=200.1nm (green continuous) and z_{CH} =210.1nm (green dashed). The other parameters of the calculations are the same of Figure 3-3. It is evident that, unlike the constant height profiles, the information given by the intrinsic profile represents qualitatively the dielectric nature of the sample in all its part; for the constant height profiles instead, this is true only at the closest point to the tip, i.e. at the point of maximum height of the sample.

point of maximum height of the sample, h'_{max}, is equal to the contrast of images acquired in constant height mode (green lines), i.e. when scanning the tip at a constant distance from the substrate $z_{CH} = h_{max}{}' + z_{lift}$.

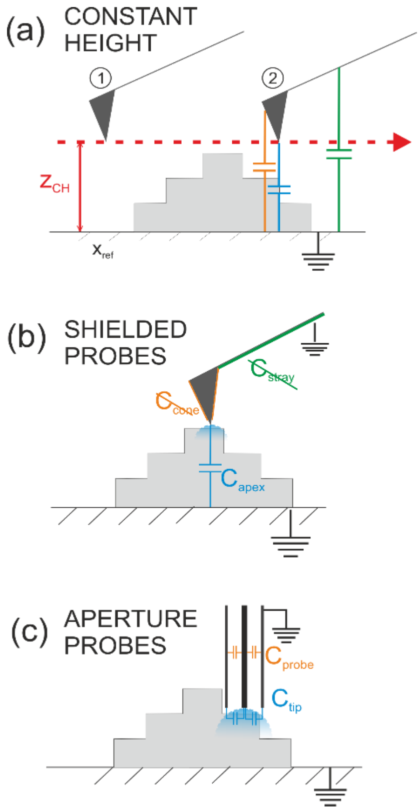

Figure 3-5 Capacitance contributions to the raw capacitance image for different imaging modes and tip alternatives. (a)The capacitance from point 1 to point 2 in images acquired in constant height mode doesn't present the crosstalk contribution, because the distance from the substrate is the same in point 1 and point 2, and cancels out. (b) Shielded probes eliminate the contribution of the tip cone and of the cantilever's stray, being these parts at the same electric potential of the substrate; the image contrast thus results only from the tip apex capacitance variation. (c) In aperture probes, only the small aperture interacts with the sample and produces the capacitance variation.

As it can be seen in Figure 3-5a, the constant height mode by definition does not contain topography crosstalk contributions, but the signal acquired is maximized only at the closest point to the tip: the regions of the sample next to the substrate give a poor response, being far from the tip. For this reason, it is a convenient alternative only for thin flat samples.

From Figure 3-5b it is also evident that shielding the cantilever and the cone eliminates or reduces the contributions due the long range stray interactions with the substrate, but, in images acquired in contact or intermittent mode, the topography crosstalk still remains, due to the apex capacitance dependence on the distance from the substrate.

If the sample is tall enough, only aperture probes can effectively eliminate both parasitic contributions, as illustrated in Figure 3-5c. For aperture probes indeed the electrical coupling takes place between the two conductors of the waveguides, strip lines or resonators and not with the substrate. By consequence, no stray contribution is present and, unless the sample is thin, no interaction with the substrate occurs, therefore the apex capacitance is not a function of tip-substrate distance. As mentioned in chapter 2, the major drawback of this kind of probes is the limited resolution, as the aperture size is generally hundreds of micrometres.

3.2 Topography crosstalk reconstruction

From the considerations above it emerges that for the measurements of biological samples in the context of this thesis it is not possible to eliminate neither crosstalk nor stray in the experimental phase. Thus, in order to extract the intrinsic dielectric information of the sample, it was elaborated a method which quantifies these parasitic contributions and removes them from the raw capacitance images in a post-processing phase.

This method consists in combining a topographic image with a capacitance variation approach curve $\Delta C(z, z_{ref})$ taken on a point on the metallic substrate of the sample, far enough from the sample to not to be influenced by its dielectric characteristics.

The approach curve is defined as capacitance variation with respect to a point z_{ref} far from the substrate: $\Delta C(z, z_{ref})=C(z)-C(z_{ref})$. During the image scans, the tip-substrate distance is given pixel by pixel by the topographic image and the lift distance as $z = h'(x_i) + zlift$.

Each of these points is found interpolating the abscissae of the capacitance variation approach curve, and its corresponding capacitance variation is recorded for the pixel. The topography crosstalk image is thus formed pixel by pixel and can be subsequently subtracted from the raw capacitance image. The left over capacitance gives the intrinsic capacitance image.

This reconstruction requires a preliminary step to set the capacitance on the substrate at the same value for the raw capacitance image and the approach curve: indeed, since the respective reference points can be different, the capacitance variation values on the substrate at the lift distance is in general different. In order to equalize them, the capacitance variation approach curve is then shifted of the quantity:

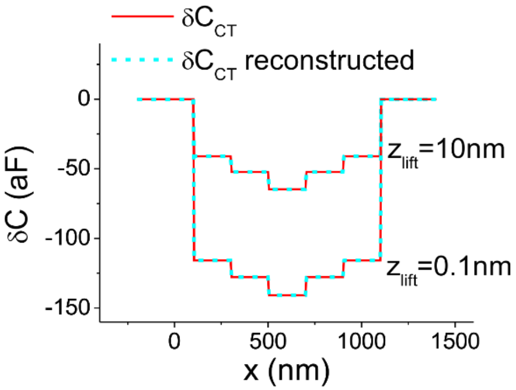

Figure 3-6 Equivalence of the methods of crosstalk calculations. The red lines represent the crosstalk profile calculated with Equation 3-2, at z_{lift}=0.1nm (contact) and z_{lift}=10nm (intermittent). The dashed lines represent instead the crosstalk profiles reconstructed by combination of the topography profile in Figure 3-3a and the cyan (for contact) and pink (for intermittent) capacitance variation approach curve in Figure 3-7. At both distances there is perfect agreement of the reconstructed crosstalk profiles with the crosstalk profile calculated.

$$\Delta C_{shift}(z, z_{shift}) = \Delta C(z, z_{ref}) - \left(\delta C_T \left(z_{lift}, h'(x_{ref}), \varepsilon_r(x_{ref}) \right) - \Delta C\left(z_{lift}, z_{ref} \right) \right) =$$

$$= \delta C_T \left(z_{lift}, 0, 1 \right) - \Delta C\left(z_{lift}, z_{ref} \right)$$

where $\delta C_T\left(z_{lift}, h'(x_{ref}), \varepsilon_r(x_{ref})\right) = \delta C_T\left(z_{lift}, 0, 1\right)$ is the average capacitance variation of the substrate on the image, calculated over a area of the substrate generally corresponding to 256*4 pixels, whereas $\Delta C(z_{lift}, z_{ref})$ is the capacitance variation of the approach curve on the substrate, calculated at the distance z_{lift}.

The crosstalk contribution in the *i*-th pixel is then given by $\delta C_{T,CT}\left(z_{lift}, h'(x_i), 1\right) = \Delta C_{shift}\left(h'(x_i) + zlift, \mathrm{z_{ref}}\right)$.

The procedure is illustrated in Figure 3-6 for the same sample in

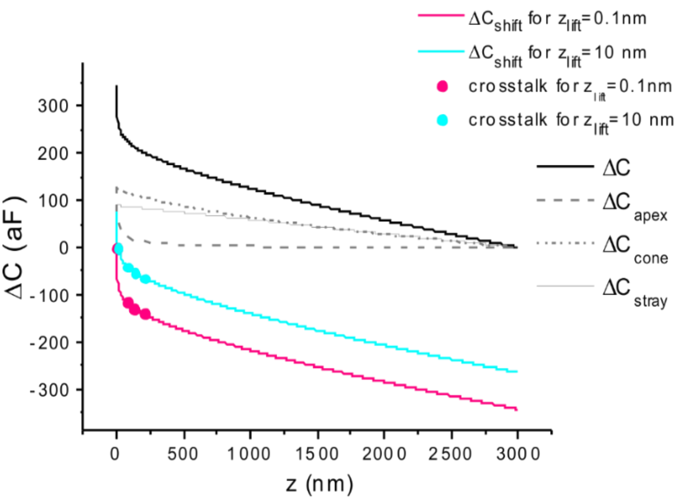

Figure 3-7 Capacitance variation approach curve. Black line: capacitance variation approach curve calculated with Equations 3-4, for R=300nm, tip half angle θ=10º, k_{stray}=0.03aF/nm, cone height H=80µm, z_{ref}=3µm. The three contribution of apex, cone and stray are shown separately in grey. The curve has been shifted vertically so that $\Delta C(z_{lift}=0.1nm)=0aF$ (cyan curve), and $\Delta C(z_{lift}=10nm)=0aF$ (pink curve), to reconstruct the crosstalk profiles in Figure 3-6 and Figure 3-8b-c (dashed lines). The dots represents the values of the crosstalk profile on the curves.

Figure 3-3. The red lines represent the crosstalk profile calculated with Equation 3-2 same as in Figure 3-3b, whereas the cyan lines represent the crosstalk calculated using the single point approach curve on metal Figure 3-7 (black line), but shifted ~343aF for the crosstalk profile at z_{lift}~0nm (cyan) and ~265aF at z_{lift}=10nm (pink). Because of the shift, we have $\Delta C_{shift}\left(z_{lift}, z_{ref}\right) = \delta C_{T,raw}\left(z_{\,lift}, 1, 0\right) = 0$. The capacitance variation approach curve is derived from the same theoretical formulae in Equations 3-4, setting $\varepsilon_r(x)$=1, $h'(x)$=0 and the points reconstructing the crosstalk profile are found on the approach curve at distances $z=h'(x) + z_{lift}$.

Such points are depicted as bullets on the curves in Figure 3-7 and as dashed line in Figure 3-6. Since the two crosstalk profiles (cyan and red lines) perfectly overlap, we can assay that the reconstruction of the crosstalk from the approach curve is a valid method.

These result holds true as long as the formulae for thin film can be applied. Nonetheless, the equivalence between the crosstalk profiles has been proven also for the case of a more complex and realistic geometry, an ellipsoid, by means of 3D numerical calculations (Figure 6-1i, inset).

In Figure 3-8 we repeated the analysis for the case of a heterogeneous pillar (Figure 3-8a, orange line). Figure 3-8b-c show the cross-section profiles of the capacitance variations at z_{lift}~0 (b) and z_{lift}=10nm (c).

The black lines represent the raw capacitance profile given by Equation 3-1, the red lines represent the crosstalk capacitance profile given by Equation 3-2 and the blue lines represent the intrinsic profile calculated with Equation 3-3. The dashed dark green lines represent the crosstalk reconstructed combining the topography profile in Figure 3-8a with the shifted approach curves in Figure 3-7.

In contact (Figure 3-8b), this profile reproduces qualitatively the trend of $\varepsilon(x)$. At higher tip-sample distance, z_{lift}=10nm, some topographic feature is still observable. In Figure 3-8d we can notice that for the fact that the tip is on average farther from the sample surface, the intrinsic contrast is reduced in intermittent mode. It is also shown, for comparison, the profile at constant height, taken at a constant distance from the substrate of $z_{CH}=z_{lift}+200nm$. We can observe what above mentioned, namely that the contrast at constant height is maximum only on top of the sample, where it is also equal to the intrinsic contrast. Out of the region of maximum height yet, the constant height profile still retains topographic effects (see especially Figure 3-8d)

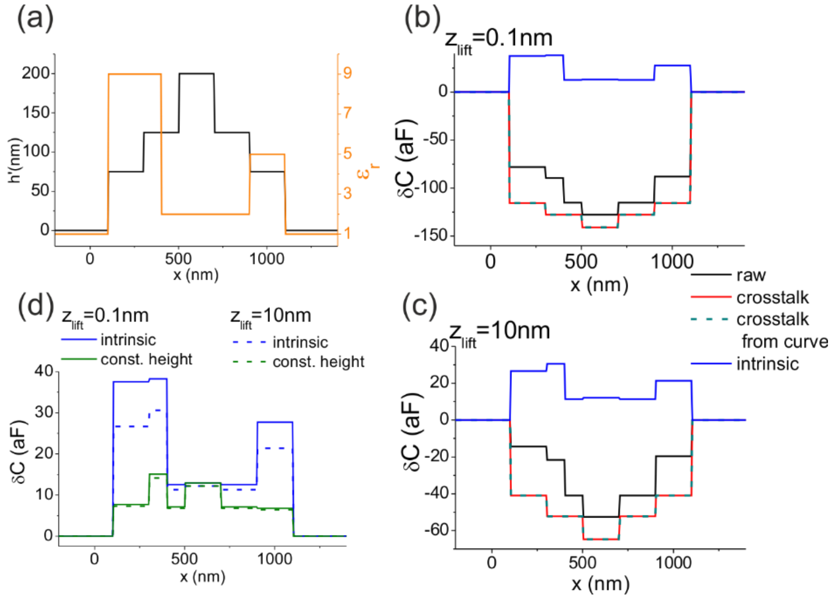

Figure 3-8 Capacitance contrasts in case of heterogeneous sample. a) Topography and permittivity of an hypothetical sample with heterogeneous dielectric properties. (b) Raw (black), crosstalk (red), intrinsic (blue)capacitance contrast profiles, calculated with Equation 3-1, Equation 3-2 and Equation 3-3, using the profiles in (a) and z_{lift}=0.1nm (contact). The dashed line represents the crosstalk profile calculated combining the topography profile in (a) and the cyan capacitance approach curve in Figure 3-7, for which we observe perfect agreement with the crosstalk profile calculated with the formula. (c) Same as (b) for z_{lift}=10nm (intermittent) and pink approach cure in Figure 3-7. (d) Intrinsic profiles in contact (blue continuous) and intermittent (blue dashed) mode, same as in (b) and (d), compared with the constant height profiles respectively at z_{CH}=200.1nm (green continuous) and z_{CH}=210.1nm (green dashed). The other parameters of the calculations are: tip radius R=300nm, tip half angle θ=10º, k_{stray}=0.03aF/nm, cone height H=80µm, z_{ref}=3µm. We can observe that the intrinsic contrast reproduces qualitatively the dielectric characteristics of the sample, and that the contrast is maximized in contact. Moreover, the corresponding intrinsic and constant height profiles match at the point of maximum height of the sample.

3.3 Software implementation

A Matlab script was coded in order to apply the algorithm detailed above to the experimental capacitance images and approach curves. The script receives as input the images of topography and calibrated capacitance, the approach curve on the metallic substrate, and the tip-sample distance at which the images have been acquired, z_{lift}, and returns the images of the intrinsic capacitance and of the crosstalk capacitance.

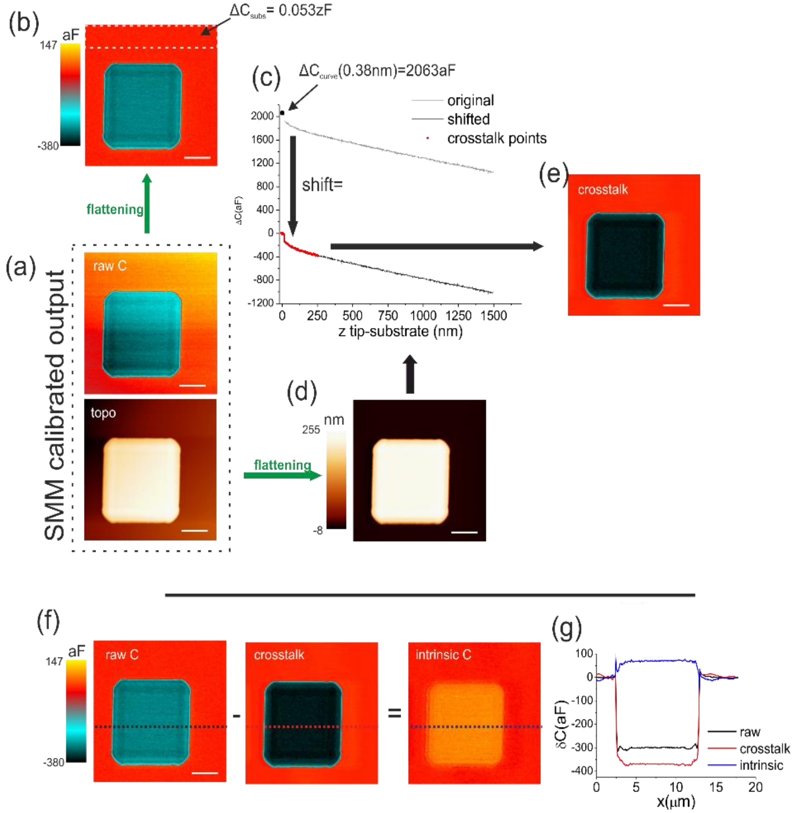

Figure 3-9 procedure for reconstruction of topography crosstalk for the software. (a) Topography and raw capacitance images output from the calibration of S_{11} of a square pillar, obtained in contact mode. (b) raw capacitance output from the flattening. The average substrate capacitance calculated in the dashed area is ΔC_{sub} =0.053zF. (c) Capacitance variation approach curve on the metallic substrate used to reconstruct the crosstalk image. The grey line represent the original curve. The value of the capacitance at zlift~0nm is ΔC_{curve}(.38nm)=2063aF. The curve subsequently shifted of ΔC_{sub}-ΔC_{curve}(.38nm), is shown in black. The points used to reconstruct the crosstalk image are shown in red on the curve. (d) Topography image after the flattening. The points of the images are interpolated in the black curve in (c) and the corresponding capacitance reconstructs the crosstalk image in (e). (f) Raw (same as (b)), crosstalk (same as (e)) and intrinsic capacitance images, and (g) corresponding cross-section profiles.

A schematic representation of the procedure is depicted in Figure 3-9, where it was applied to an image of a SiO_2 pillar acquired in contact mode. The preliminary steps needed, and performed with the free software WSxM, are shown as green arrows, while the code's steps are shown as black arrows. In the upper part of Figure 3-9, the crosstalk reconstruction procedure is outlined; in the bottom part instead it is shown the resulting intrinsic capacitance image, together with the cross-section profiles of the three images. More in detail, the preparatory editing operations, performed with WSxM, include:

- setting the physical units, aF and nm;
- flattening the substrate excluding the pixels of the sample;
- setting the images in absolute values, in particular this is important for the topography, as the substrate height must be circa zero;
- exporting the images as matrices x-y-z, where the z column is the topographic height in one case and the raw capacitance variation in the other, whereas the x-y column are the pixels indexes.

Furthermore, another preparatory is steps is the alignment of the

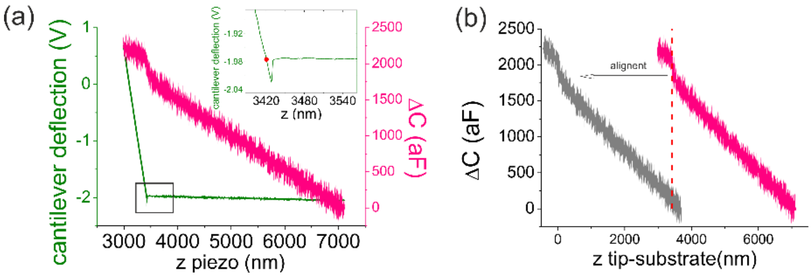

Figure 3-10 SMM approach curve alignment. (a) Green: cantilever deflection curve, pink: raw capacitance approach curve simultaneously acquired, as function of the piezo extension. The inset shows the magnification of the region of contact between cantilever and substrate, where the point z^* is found as intersection of the two linear regions of the deflection: contact and non-contact. (b) Alignment of the capacitance curve with respect to the substrate distance (grey curve), the dashed line corresponds to $z=z^*$

approach curve with respect to the distance from the substrate. By default, the capacitance approach curves on the substrate are output as capacitance versus piezo extension, and recorded simultaneously with the curves of cantilever deflection versus piezo extension.

Expressing the curves in terms of distance from the substrate consists in a shift of the abscissae by a quantity z^* which corresponds to the point of zero deflection of the cantilever: $z_{tip\text{-}substrate}=z_{piezo}-z^*$. This point is found as intersection of the non-contact horizontal region and the contact diagonal region of the cantilever deflection curve (Figure 3-10, inset).

The two edited images, the capacitance approach curve, and the value of z_{lift} are the input of the Matlab script, which performs the following operations:

- calculation of the average capacitance of the substrate ΔC_{subs}, using generally the first four rows of the image, corresponding to 256*4 pixels;

- finding on the capacitance variation approach curve the closest experimental point to z_{lift}, and its corresponding capacitance variation $\Delta C_{curve}(z'_{lift})$. When the experimental curve is noisy or too few points are available, it can be that $\Delta C_{curve}(z'_{lift})$ results visually an outlier respect to the approach curve trend. For these cases it is included the option to select it manually;
- calculation of the shift, as ΔC_{sub} - $\Delta C_{curve}(z'_{lift})$, and shift of the capacitance variation approach curve;
- Finding for each topography point (z-column of the topography matrix) the corresponding capacitance variation on the shifted approach curve: ΔC_{CT}. The image of crosstalk is formed using the x-y columns of the images and ΔC_{CT} as z column;
- Subtraction of the crosstalk from the raw capacitance image, and formation of the intrinsic capacitance image;
- The script returns the three capacitance variation images, as matrices with the same x-y columns and different z-column, namely raw, crosstalk and intrinsic capacitance.

It is important to highlight again that the algorithm implies the knowledge of z_{lift} a priori.

4. QUANTIFICATION OF THE PERMITTIVITY

The intrinsic capacitance images obtained with the procedure detailed in chapter 3 already give a qualitative indication about the dielectric characteristics of the sample. This qualitative information becomes almost quantitative in some cases, as will be more extensively shown in chapter 5.

However, most of the times, quantifying the permittivity from the intrinsic capacitance requires the use of theoretical models of the capacitive interaction between probe and sample, to which the experimental data are compared.

These theoretical models must carefully take into account not only the permittivity of the sample, but also its geometry and dimensions, as well as the geometry and dimensions of the probe.

In the first part of this chapter I discuss how to model with good approximation the geometry of the system tip-sample, and to obtain a good estimation of the dimensions. In particular, the probe's dimensions can be retrieved from a procedure of tip calibration, which I adapted from the one for low frequency electrostatic force measurements to the case of microwave capacitance measurements, and which makes use of 2D finite element numerical models of the tip. The sample's dimensions can be retrieved from the deconvolution of the topography image with the probe geometry, once this is known. I elaborated several deconvolution algorithms for the different geometries of the bacterial cells (ellipsoid, hemiellipsoid, cap ellipsoid and buried ellipsoid), and pillar (parallelepiped with rounded edges) experimentally measured in this work of thesis.

Finally, once the geometry of the system is fully known, this information can be inserted into analytical models, as well as 2D or 3D numerical models, to calculate theoretically the capacitance between tip and sample.

In the second part of this chapter, I describe the numerical 2D models for a bacterial cell and a pillar, which I adapted from the ones originally developed by the group for low frequency electrostatic force measurement, to the case microwaves capacitance measurements. These models were used for some of the results in the heterogeneous inorganic samples presented in chapter 5, and for preliminary analysis on the bacterial cell presented in chapter 6, although for these latter we eventually preferred the use of the 3D models developed by Dr. Fabregas of the research group. These 3D models are also compared to the 2D models I developed in this chapter.

From the correspondence of the theoretical calculations with the SMM measurements, the permittivity of the sample can be quantified, either from the intrinsic capacitance images or from capacitance approach curves performed on a single point on top of the sample.

As final product of the implementation of the analysis techniques and tools described, two user friendly interfaces were developed and distributed within the group, one for the tip calibration and one for the permittivity extraction.

Determination of tip and sample geometry

The capacitance is an extensive magnitude, because the electric field flux amount between tip and substrate, developed for a given electric field force (or voltage), depends not only on the dielectric permittivity (the intensive magnitude) of the material between them, i.e. the sample, but also on their distance and on the geometry of probe and sample. Subsequently, for a proper quantification of samples' permittivity from the intrinsic images, it is necessary first to have a detailed knowledge of the geometry of the two systems electrically interacting, i.e. of the tip and the sample. The next two sections deal with the methodologies developed to such aim.

4.1 Tip radius calibration

The first step of the quantification of the system geometry is the tip calibration, in particular the determination of the tip radius R. In this thesis we followed a procedure previously developed by the research group for electrical force measurements [41-43] and low-frequency capacitance measurements [44-46], based on single-point capacitance variation approach curves.

The procedure consists in measuring a capacitance variation approach curve on a point of the metallic substrate $\Delta C_{exp}(z, z_{ref}) = C_{exp}(z) - C_{exp}(z_{ref})$ and fit it to a set of curves $\Delta C_{th}(z, z_0, R, \theta) = C_{th}(z, R, \theta) - C_{th}(z_0, R, \theta) + k_{stray}(z - z_0)$ obtained from a theoretical model, with the tip geometry (apex radius R and tip half angle θ) and the stray k_{stray} as fitting parameters. Here, z_{ref} is the reference point at which the experimental curve has been set to zero, whereas z_0 is the analogous for the theoretical curve, which can be different. k_{stray} is the phenomenological parameter accounting for the non-local interaction of the cantilever with the substrate.

Although $\Delta C_{th}(z, z_0, R, \theta)$ can be obtained with the analytical formulae in Equations 3-4, for consistency with the method of extraction of permittivity for complex geometries (see ahead in the text), we rather adopted a set of numerically calculated approach curves: indeed, there is a 10% difference in the estimation of the radius between analytical and numerical models (see ahead Figure 4-4).

The numerical approach curves were obtained from a finite element simulation software (Comsol 3.4 or 5.0), where the tip was modelled as a truncated cone of different half angles θ, terminating with a hemisphere of different radii R, and at different tip-substrate distances z.

The family of theoretical approach curves thus is generated choosing a range of parameter values resembling to the particular experimental situation. Globally, simulations have been performed for tip radii from $R = 150$nm to 1800nm in steps of 50nm; half angles from θ=5º to θ=20º in steps of 5º; and tip-substrate distances taken from 7nm up to 4000nm, in 20 logarithmic steps. The cone height H is set to the nominal value provided by the manufacturer, and no cantilever is included to account the effects of the stray (see ahead in the text).

The least-square fitting routines to fit the theoretical curves to the experimental data are implemented in Matlab (Mathworks Inc.). First, it is set a common reference point ($z_{ref} = z_0 = z'_{max}$) for the family of numerical curves and the experimental curve:

$$\begin{cases} \Delta C_{exp}\left(z,\ z_{max}\right) = \Delta C_{exp}\left(z,\ z_{ref}\right) - \overline{\Delta C_{exp}}\left(z'_{max},\ z_{ref}\right) \\ \Delta C_{th}\left(z,\ z_{max},\ R,\ \theta\right) = \Delta C_{th}\left(z,\ z_0,\ R,\ \theta\right) - \ \Delta C_{th}\left(z'_{max},\ z_0,\ R,\ \theta\right) \end{cases}$$

Where z'_{max} is the numerically simulated point closest to the fitting limit chosen z_{max}. $\overline{\Delta C_{exp}}\left(z'_{max}, z_{ref}\right)$ is the average of the experimental capacitance variation approach curve over 11 points around z'_{max}.

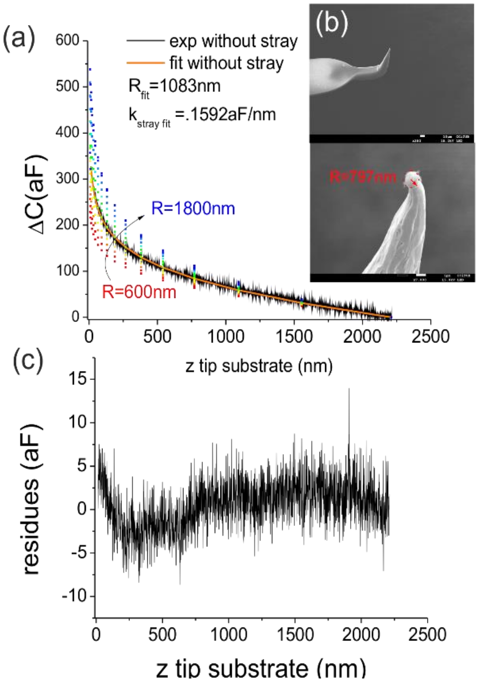

Figure 4-1 Tip radius calibration and SEM images of the calibrated tip. (a) Fit of the experimental approach curve on metallic substrate (black line), with a set of theoretical curves simulated for different radii, from R=600nm to R=1800nm (dots) and same half angle θ=10º. The fitting curve (orange line) corresponds to a radius of R_{fit}=1083nm. (b) SEM images of the same tip, from which we observe a smaller physical radius (R=797nm), and a bending of the tip. (c) Residues of the calibration fit.

Since the geometrical parameter which most influences the capacitance values is the tip radius, the cone half angle is normally kept fixed at a nominal value, typically 10 or 15º for this work of thesis, and a fit of only two variables (R, k_{stray}) is implemented. The confidence intervals of the two parameters found are calculated at the 95%.

In Figure 4-1 it is shown an example of a fit of a single curve at fixed half angle θ=10º, where the range of fit is 13-2000nm, and z'_{max}=2210nm. The results give R= 1082± 5nm, k_{stray}= 159.2± 0.2 zF. It is important to stress that the calibrated radius obtained is an electrically equivalent radius, which in fact can be much different from the physical one. Indeed, in the numerical calculations, the value found by the fit corresponds to the radius of an ideal axial symmetric tip which would give the same measured capacitance of the actual tip. This latter yet undergoes important modifications of shape and dimensions at the beginning of any experiment, when it is purposely enlarged with harsh imaging conditions (high setup, fast scans etc.), in order to maximize the signal acquired. As a consequence, the conical ideal shape can be partially lost, as we can see from the SEM images. The different tip shape with respect to the ideal shape of the model explains the discrepancy in the values found from the fit and its physical dimensions. For the curve in Figure 4-1, for instance, the Scanning Electronic Microscope (SEM) images taken after the tip usage show an apex about 25% smaller than the electrically equivalent radius found.

The value of radius resulting from the calibration is strongly dependent on the distance range at which we perform the fit. In particular the effects of the radius are evident at small tip-substrate distances (indeed it is the apex-substrate interaction which provides the local information) whereas at the larger distances, the long range contribution of the cone and the stray weight more. As a general rule, the fitting distance must be at least twice the tip radius in order to steadily estimate its value, i.e. to attenuate dependence from the fitting range.

Generally, we extract the tip radius from the average of the fit results of more than one subsequent experimental approach curve. Moreover, in order to account for possible tip structural modifications or adhesion of material (occurring frequently when working with biological cells) we compare the tip dimension obtained from curves acquired in the metal region before and after performing an image or an approach curve on top the sample. It was also observed that when the stray changes considerably, for instance because the sample is taken out and substituted with another, this changes also the shape of the approach curve in a way that not only the value extracted from the fit for k_{stray} is different, but also for the radius.

4.1.1 Numerical models

Two-dimensional and three-dimensional numerical models of the tip were used in the scope of this thesis, to calculate the theoretical capacitance approach curves. The three-dimensional model was completely developed by Dr. R. Fabregas, and it won’t be detailed here. On the contrary, I adapted the two dimensional model,

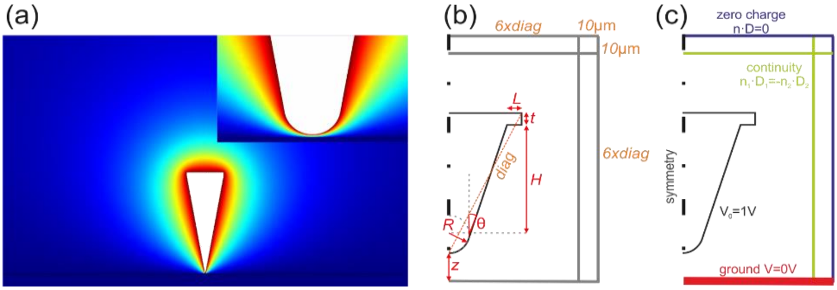

Figure 4-2 2D model for the tip. (a) Electric potential around the tip and (inset), at the tip apex. (b) Sketch of the geometry and dimensions of the model and (c) of the boundary conditions.

originally implemented by previous members of the research group for electrostatic force measurements, to the case of capacitance measurements and larger tip radii.

The 2D model was implemented in the finite element commercial software Comsol Multiphysics 3.4.

The tip is modelled in axisymmetric geometry (Figure 4-2) as a truncated cone of height H=80μm (nominal height of the AFM probes used for the experiments) and half angle θ, ending with a hemispherical apex of radius R, located at a distance z from the metallic substrate. A disk of thickness t and width $R_{disk}=L+H \cdot tg\theta$ is placed at the base of the cone to mimic the cantilever effects, where L is the part of the disk radius protruding from the base. Note that L is not the physical dimension of the cantilever, but represents the effective interaction of the cantilever with the substrate, i.e. the stray. For this, since in the least square fitting of the calibration we account for the stray as independent fit parameter k_{stray}, it is set L=0. The use of L is relevant instead for thick dielectrics [43].

The capacitance acting between tip and sample is calculated by integration of the electric displacement all over the cone surface. Assumed the validity of the electrostatic approximation of the electric potential in the near-field region, this is found by solving Poisson’s equation:

$$\begin{cases} -\nabla\cdot\left(\varepsilon_0\varepsilon_r\nabla V\right)=0 \\ bounday\,conditions \end{cases} \rightarrow \vec{D}=-\varepsilon_0\varepsilon_r\nabla V \rightarrow C=\frac{Q}{V_0}=\frac{\iiint_{tip}\rho\,dV}{V_0}=\frac{\iiint_{tip}\nabla\cdot\vec{D}\,dV}{V_0}=\frac{\oiint_{tip}(\hat{n}\cdot\vec{D})dS}{V_0}$$

where Q is the total charge on the tip, ρ is the charge density and $\varepsilon_r=1$ in air.

The boundary conditions are set as follows (Figure 4-2): electric potential V_0=1V on the probe, ground V=0V on the metallic substrate, and electrical insulator ($\hat{n}\cdot\vec{D}=0$) at the simulation box boundaries. It was checked that the capacitance values obtained did not vary with the dimensions of the simulation box, as it was added a perfectly matching layer approximating the radial and axial lengths away from the active region to infinite.

The model was previously applied for EFM models in [41, 43, 47], where the force acting on the tip is proportional to the capacitance gradient $\frac{dC}{dz}$, and this is numerically calculated from the electric potential by integration of the built-in Maxwell stress tensor over the surface of the probe. In order to verify the adaptation of the model to the capacitance calculations, we simultaneously calculated the absolute capacitance, C_{Comsol}, and its gradient, $\frac{dC_{\mathrm{Comsol}}}{dz}$, and checked that the numerical integration (with the

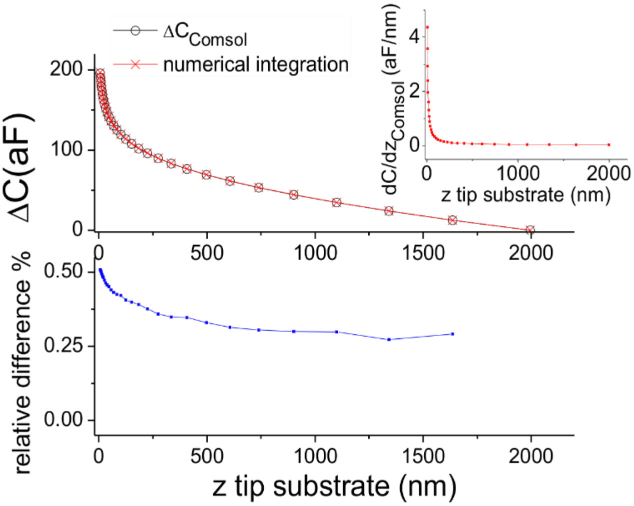

Figure 4-3 Validation of the 2D model by comparison between integrated capacitance gradient numerically calculated (red line with cross) and capacitance numerically calculated (black line and dots). The capacitance gradient is shown in the inset. The absolute difference is less than 1aF, one order of magnitude smaller than the experimental noise. Parameters of the simulation: R=500nm, θ=10º, H=80µm, L=0um, z_{ref}=2000nm.

trapezoids approximation) of $\frac{dC_{\text{Comsol}}}{dz}$ along z and from a reference point z_0=2000nm far from the substrate, coincides with the capacitance variation, with respect to the same point, output by the software. As shown in Figure 4-3 the integration of $\frac{dC_{\text{Comsol}}}{dz}$ is equivalent to use directly $\Delta C_{Comsol}=C_{Comsol}(z)-C_{Comsol}(z_0)$, which demonstrate the exactness of capacitance calculations.

Figure 4-4 shows the comparison of the 2D model with the analytical formulae (Equations 3-4) and the 3D model, implemented in Comsol Multiphysics 5.0 by Dr. Fabregas from the

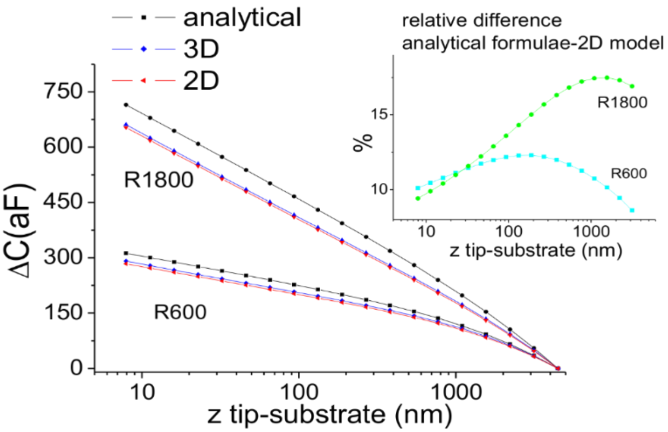

Figure 4-4 Comparison between 2D (red dotted line), 3D (blue dotted line) and analytical (black dotted line) models, for two different radii, R=1800nm and R=600nm, and θ=10º, H=80um, L=0um, z_{ref}=4466nm. The analytical model overestimate the capacitance of about 10-15% (inset).

research group. Since the tip is modelled in axisymmetric geometry, the 2D and 3D models give similar results: the maximum difference is around 7aF at $z=z_{min}$=7nm, and decays to zero with the increasing distance. Variations of the boundary box dimensions in the two model can explain this small (yet larger than the experimental noise) difference in the capacitance values. For this it is important to maintain the coherency between the model, 2D or 3D, used to calibrate the tip, with the model used to extract the permittivity of the sample. The same conclusion is even more valid when using the analytical formulae, which, as it can be seen, overestimate the values of the capacitance about 10%.

4.2 Software implementation: interface 1

A user friendly interface (Figure 4-5) was coded with the “Matlab GUI build environment”, in order to execute the fitting routines and thus calibrate the tip.

Briefly, the interface receives as input the file of the experimental approach curve, and information about the type of fit, such as the number variables to be fitted (radius and half angle(s)), range of distances etc. Then, it loads a database of theoretical curves previously calculated, and perform the fit accordingly. The output of the interface are the fitting curve and the values found for the fit variables.

The operating principle is describd more in detail in the following steps.

1) The user starts by loading the file of the experimental approach curve, which is plotted on the graph area of the interface. Then, he selects name and path for the fitting output file. By default, the interface automatically sets the name as “***Experimental_File_Name*****_fit_on_metal**” and puts it into the same folder of the experimental file. The output of the fitting file includes the values found by the fit for radius and half angle(s) and stray.
2) The user choses a kind of fit, by selecting the tip model and the variables enabled as free fitting parameters ($k_{stray}$is always fitted by default). In the tip model, it is included the particular case of a conic

tip with two semiangles, particularly diffused for the case of small tip (R<20nm). The SMM tips used in this work however have radii at least one order of magnitude larger, for which the model of double angle is not used in this work of thesis. Thus, only the fit options for single angle tips will be discussed here, namely fits for only two variables, where the radius and the k_{stray} are free fitting parameters (the most common option), and the fit for three variables, where the half angle is the third free fit parameter. The selection is made by marking the corresponding box (note that **LargeAngle** box is disabled for fit at single angle).

3) The user sets the initial guess for the fitting variables: if a variable is disabled for the fit, the value typed in the box will be the fixed value for it. Otherwise, it will be initial point of the fit. Furthermore, it is needed to set the value of the cone height, typically 80µm. The combination of the chosen initial guess values automatically prompts the load of a specific set of simulated approach curves, i.e. the most similar curves to the initial guess combination. In fact, the interface is linked to a database of several sets of approach curves numerically calculated with 2D and 3D models and obtained combining various ranges of the tip geometrical parameters. This database can be

progressively updated: for instance, if the combination of the initial guess values is not included in any of the simulation sets available, a warning message is output. In such case, it is necessary to produce *ex situ* a new customized set of numerically calculated approach curves, which can be loaded into the interface with the corresponding button, and used for the fit.

4) The user selects the tip-substrate distance range for the fit, for which he has two options: by clicking on the experimental curve plotted on the graph area, or by typing the values of the end points wished on the box.
5) The user starts the fit. The experimental curve and the simulations are put to zero at the point of the simulations closest to the z_{max} selected, z'_{max}. The initial point for the stray parameter is automatically calculated as the slope of the curve in the last segment.
6) The fit results with their limits of the confidence interval appear in the box of **FitResults** and on the graph. The standard deviations of the parameters found from the fit is calculated at the 95%. These define the upper and lower limit of the confidence interval, and are used to interpolate the two black dashed error curves encompassing the green continuous curve of the best fit (Figure 4-5, bottom)

7) The next steps possible for the user are repeating the fit (**Clear and do it again**), or launch the interface for the permittivity extraction, which will be detailed further on.

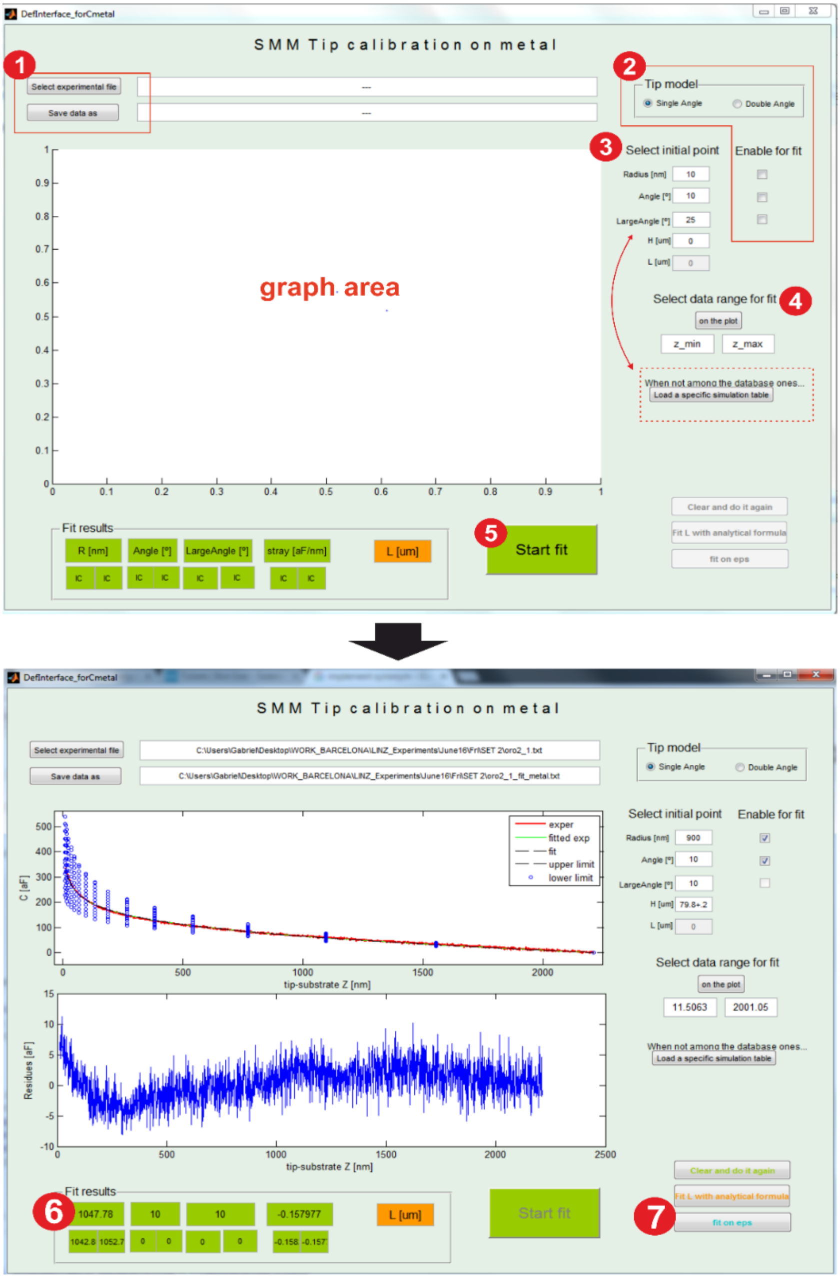

Top:

Select experimental file: ---

Save data as: ---

Tip model: ● Single Angle ○ Double Angle

Select initial point		Enable for fit
Radius [nm]	10	☐
Angle [º]	10	☐
LargeAngle [º]	25	☐
H [um]	0	
L [um]	0	

Bottom:

Select experimental file: C:\Users\Gabriel\Desktop\WORK_BARCELONA\LINZ_Experiments\June16\Fri\SET 2\oro2_1.txt

Save data as: C:\Users\Gabriel\Desktop\WORK_BARCELONA\LINZ_Experiments\June16\Fri\SET 2\oro2_1_fit_metal.txt

Tip model: ● Single Angle ○ Double Angle

Select initial point		Enable for fit
Radius [nm]	900	☑
Angle [º]	10	☑
LargeAngle [º]	10	☐
H [um]	79.8+.2	
L [um]	0	

Select data range for fit: 11.5063 2001.05

Fit results:

1047.78	10	10	-0.157977
1042.8 1052.7	0 0	0 0	-0.158 -0.157

Figure 4-5 Interface for tip calibration (top) and example of the fit of an approach curve (bottom).

4.3 Tip-sample deconvolution

As in all SPM techniques, it must be considered that the AFM tip is never ideal, i.e. a Dirac's delta. Thus, the topography image obtained during the scans is affected by some distortions due to its finite size. This in particular occurs when tip radii and samples heights are comparable, such as in our case, where these characteristic dimensions are in the order of 100nm. As a consequence, it is not utterly correct to take as sample's planar dimensions directly the values obtained from the topography cross-section profiles.

In order to take into account and correct the effect of shape dilation, I developed several algorithms for tip-sample deconvolution. The deconvolution procedure consists in the following steps: the 3D sample`s shape is approximated to a regular one, while the tip is still modelled as a cone terminating with an half sphere. The two main vertical plans of the sample are considered. For both, it is found the analytical expression of the lowest point of the tip when the tip is tangent to the sample, along the lateral direction (analytical convolution). The analytical convolution represents the core of the algorithm: it depends on the regular shape considered for the sample, the dimensions of the tip (half angle θ and radius R, known from the calibration) and the (deconvoluted) dimensions of the sample (height and lateral dimension along the axis). The sample's height is exactly the value resulting from the topography, whereas the lateral dimension is varied until it is found the value for which the analytical convolution best adjusts the topography cross-section profile along the direction considered.

In this work of thesis I measured two basic kinds of samples, a square pillar and a bacterium, for which I developed two class of deconvolution algorithms. In the following, the analytical expressions of the convolution profiles are derived in the various cases of geometry and dimensions of tip and samples.

4.3.1 Pillar with rounded edges

In Figure 4-6 it is depicted the geometry considered for a square pillar of half width L_p and height H_p (only the half is shown, being it symmetrical respect to *z*-axis). The pillars measured exhibit upper rounded edges, which we modelled as a quarter of ellipse of semiaxes *a, b*. Next to it, a tip of radius *R* and half cone half angle θ is shown, moving in contact with the pillar towards the origin of the axes. The path of the lowest tip point, *h'(x),* as the tip moves along the *x*-axis, is depicted in blue, and represents the analytical convolution.

The derivation is made in the hypothesis that first point of the tip touching the pillar rounded edge belongs to the tip cone:

$$R(1-\sin\theta) < z_T = Hp - b + \left(\left(\frac{a^2}{b^4} ctg^2\theta \right)^2 + \frac{1}{b^2} \right)^{-1/2} .$$

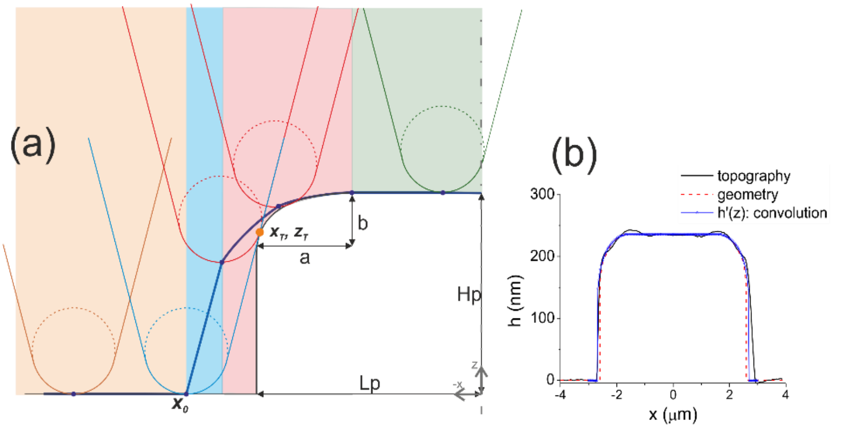

Figure 4-6 Tip-pillar convolution in the case of contact with the tip cone. (a) Only half of the pillar is shown, assuming it symmetric. The four regimes of the motion are depicted in different colours: orange: the tip moves on the substrate, cyan: the tip cone touches the pillar corner and the tip rises up, red: the tip apex is tangent to the pillar corner, green: the tip moves on the planar part on top of the pillar. The overall motion of the lowest tip point, i.e. the convolution, is represented by the blue line. The pillar dimensions to be extracted from the comparison with the topography are the lateral dimension L_p and the corner axis, *a,b*, whereas the pillar height H_p is set to the topography value. x_T, z_T are the coordinates of the first tangency point, and x_0 is the position at the tangency. (b) Example of convolution (blue line) matching the topography cross-section (black) for a pillar of height H_p =236nm, and calculated for a tip radius *R*=167nm, and half angle θ=15º. We found L_p =2.6μm, *a*=1 μm, *b*=80 nm. The dashed line represents the geometry found.

As shown in Figure 4-6 four regions composing the tip motion can be distinguished, highlighted in different colours:

$$h'(x)=\begin{cases} 0 \quad \text{for } x \le x_0 \\ (x-x_0)\cdot ctg\ \theta \quad \text{for } x_0 < x \le x_T - R\cdot cos\theta \\ (H_p-b)+\ b\ sin\alpha(x)-\dfrac{a}{b}tg\alpha(x)\cdot\sqrt{\dfrac{R^2}{1+\left(\dfrac{a}{b}tg\ \alpha(x)\right)^2}} \quad \text{for } x_T - R\cdot cos\theta < x \le -L_p + a \\ H_p \quad \text{for } -L_p + a < x \le 0 \end{cases}$$

Equation 4-1

where x_0 is the position when the cone is tangent to the pillar:

$$x_0 = x_T - \left(z_T - \left(H_p - b\right) - R\left(1 - \sin\theta\right)\right) \cdot tg\theta - R \cdot cos\theta$$

x_T and z_T are the coordinates of the first tangent point:

$$\begin{cases} x_T = -\dfrac{a^2}{b^2} \cdot ctg\theta \cdot \left(z_T - \left(H_p - b\right)\right) + (-L_p + a)) \\ z_T = \dfrac{1}{\sqrt{\dfrac{a^2}{b^4} \cdot ctg^2\theta + \dfrac{1}{b^2}}} + (H_p - b) \end{cases}$$

and the angle $\alpha(x)$ can be extracted from the non-linear equation of the x-coordinate of the tangent points between tip apex (sphere) and pillar corner (ellipse):

$$x = a\,cos\alpha\left(x\right) - \sqrt{\frac{R^2}{1 + \left(\dfrac{a}{b} tg\,\alpha\left(x\right)\right)^2}} + L_p - a$$

In this case, the lateral dimensions to be found by adjusting the analytical convolution to the topography profile are *a, b* and L_p. Figure 4-6b shows an example for R=167nm, θ=15º, H_p=236nm, where we found L_p=2.6µm, a=1µm, b=80nm. The black line represents the cross-section of the topography image, the dashed red lines represents the geometry corresponding to the dimensions extracted by the deconvolution, and the blue dotted line represents the convolution, calculated with Equation 4-1.

For large radii instead (Figure 4-7), the tip cone never touches the pillar. In particular, when the first contact point occurs between the apex sphere and the pillar rounded corner, i.e. in the hypothesis

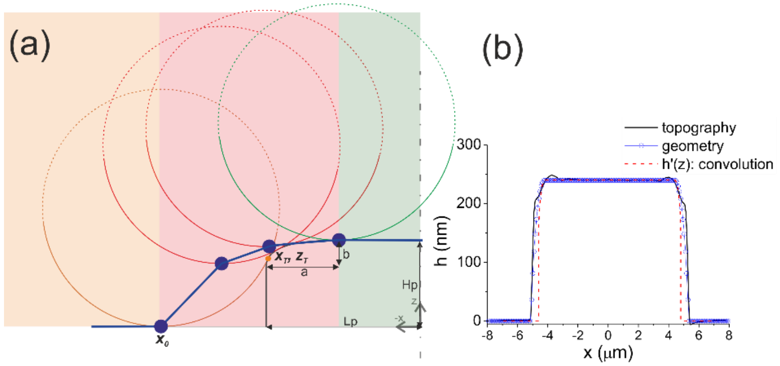

Figure 4-7 Tip-pillar convolution in the case that only the tip apex contacts the pillar. (a) Only half of the pillar is shown, assuming it symmetric. The three regimes of the motion are depicted in different colours: orange: the tip moves on the substrate, red: the tip apex is tangent to the pillar corner, green: the tip moves on the planar part on top of the pillar. The overall motion of the lowest tip point, i.e. the convolution, is represented by the blue line. The pillar dimension to be extracted from the comparison with the topography are the lateral dimension L_p and the corner axis, *a,b*, whereas the pillar height H_p is set to the topography value. x_T, z_T are the coordinates of the first tangent point, and x_0 is the position of the tip at the tangency. (b) Example of convolution (blue line) matching the topography cross-section (black) for a pillar of height H_p =240nm, and calculated for a tip radius *R*=965nm. We found L_p =4.7μm, *a*=400nm, *b*=100nm. The dashed line represents the geometry found.

that $R(1-\sin\theta) > z_T = Hp - b + \left(\left(\frac{a^2}{b^4}ctg^2\theta\right)^2 + \frac{1}{b^2}\right)^{-1/2}$,

the analytical convolution is given by:

$$h^{'}(x) = \begin{cases} 0 \ \text{ for } x \le x_0 \\ -R + \left(H_p - b\right) + \ b\ sin\alpha\left(x\right) - \frac{a}{b} tg\alpha\left(x\right) \cdot \sqrt{\dfrac{R^2}{1 + \left(\frac{a}{b} tg\alpha\left(x\right)\right)^2}} \ \text{ for } x_0 < x \le \text{-}L_p + a \\ = H_p \ \text{ for } \text{-}L_p + a < x \le 0 \end{cases}$$

Equation 4-2

For the second tract of the convolution, i.e. $x_0 < x < -L_p + a$, depicted in red in Figure 4-7, we calculate the x position of the centre of the apex circle tangent to the corner ellipse, for $x\,\epsilon\left[-L_p - R;\ -L_p + a\right]$, from which we extract the angle $\alpha(x)$.

$$x = a\,cos\alpha(x) - \sqrt{\frac{R^2}{1+\left(\frac{a}{b}tg\alpha(x)\right)^2}} + L_p - a \rightarrow \ \alpha(x)$$

Then we calculate the corresponding convolution as in the formula above, keeping only *h'(x)>0.*

The position of the tip at the first tangent point with the pillar, x_0, is found as the minimum x such that *h'(x)≥0*.

Here too, the lateral dimensions to be varied to match the topography profile and analytical convolution are *a, b* and L_p. In Figure 4-7b it is shown an example for for *R*=965nm and, H_p=240nm, where we found L_p=4.7µm, *a*=400nm, *b*=100nm.

4.3.2 Bacterium

The bacterium geometry can be approximated to an ellipse, a cap ellipse with a conical base or a buried ellipse. These analytical convolutions are descripted here and found good agreement for

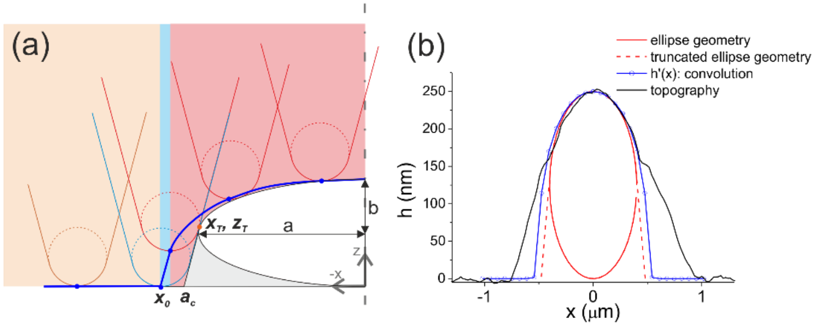

Figure 4-8 Convolution for ellipse and a cap ellipse with a conical base. (a) Only half of the ellipse is shown, assuming it symmetric. The three regimes of the motion are depicted in different colours: orange: the tip moves on the substrate, cyan: the tip cone is tangent to the ellipse, red: the tip apex is tangent to the ellipse. The overall motion of the lowest tip point, i.e. the convolution, is represented by the blue line. The grey area represents the truncated conical base of the cap ellipse, having a_c as axis dimension. The ellipse (or cap ellipse) dimensions to be extracted from the comparison with the topography are the lateral dimension a, (or a_c) whereas the ellipse height $b = H_p/2$ is set to the topography value. x_T, z_T are the coordinate of the first tangent point, and x_0 is the position at the tangency. (b) For both geometries (ellipse as continuous red line, cap ellipse with conical base as red dashed line), the convolution (blue line) matches equally the topography cross-section (black). The parameters of the calculations are R= 113nm, θ=30º, $H_p = 2b$=250nm. We obtained a=400nm and a_c=476.6nm.

our experimental cases but do not claim to be exhaustive of all the possible geometries of the bacterial cells.

In the case that the tip cone contacts the bacterium ellipse before the apex (i.e. $R(1 - sin\theta) < b = H_p/2$, where H_p is the bacterium height) the convoluted path of the tip is then composed of three regions (Figure 4-8):

$$h^{'}(x)=\begin{cases}0 \ \text{ for } x\le x_0\\(x-x_0)\cdot ctg\theta \quad \text{for } \ x_0<x\le x_T-R\cos\theta\\R+\left(H_p-b\right)+\ b\ sin\alpha\left(x\right)-\frac{a}{b}tg\alpha\left(x\right)\cdot\sqrt{\frac{R^2}{1+\left(\frac{a}{b}tg\alpha\left(x\right)\right)^2}}+b \ \ \text{for } x_T-R\cos\theta\le x<0\\ \end{cases}$$

Equation 4-3

where the first tangent point x_T, z_T is given by:

$$\begin{cases}x_T=-\frac{a^2}{b^2}\cdot ctg\theta\cdot\left(z_T-b\right)\\z_T=\frac{1}{\sqrt{\frac{a^2}{b^4}\cdot ctg^2\theta+\frac{1}{b^2}}}+b\end{cases}$$

and the position of the apex at the tangent point is:

$$x_0=x_T-\left(z_T-b-R\left(1-\sin\theta\right)\right)\cdot tg\theta-R\cdot cos\theta$$

The angle $\alpha(x)$ of the third part of the motion can be found solving the non-linear equation of the centre of a circle tangent to the ellipse, for $x \,\epsilon [x_T - Rcos\theta; 0]$:

$$x=a\,cos\alpha\left(x\right)-\sqrt{\frac{R^2}{1+\left(\frac{a}{b}tg\alpha\left(x\right)\right)^2}}+L_p-a\rightarrow\ \alpha\left(x\right)$$

The same analytical convolution could be given by a cap ellipsoid corresponding to an ellipse of semiaxes a, $b=H_p/2$, having an elliptic-based conical shape of height z_T and axis

$$a_c=x_T-\frac{z_T}{\left[-\left(\frac{b}{a}\right)^2\cdot\frac{x_T}{z_T-b}\right]}$$

The conical base is depicted as grey area in the figure, thus in this case the bacterium is formed by the white and grey regions.

The lateral dimension to be adjusted in this case is only a (or a_c). In Figure 4-8b it is shown in red an example for the two cases of cap ellipsoid and ellipse, for which R= 113nm, θ=30º, H_p=250nm. We obtained a=400nm and a_c=476nm. The topography cross-section is depicted as black line, the ellipse geometry found as a continuous red line, and the truncated cone base as a red dashed lines. For both geometries, the convolution obtained from Equation 4-3 is represented by the blue line.

As we can see from Figure 4-8b, the analytical convolution does not follow well the topography profile, especially at small h. We found that in such conditions an ellipse buried under the surface of a quantity $d=(b-H_p)$, where b is the vertical semiaxes of the ellipse, adapts better. In such case, together with the lateral dimension a it is necessary to determine also the buried depth d.

The analytical profile of a buried ellipse is derived in the conditions sketched in Figure 4-9, when the contact point belongs always to the surface of the tip apex: $R(1-sin\theta) \geq \left(\frac{a^2}{b^4}ctg^2\theta + b^{-2}\right)^{-\frac{1}{2}} - d$.

We first find the coordinates of the convolution of the apex circle tangent to and the ellipse for any $x\,\epsilon[-a-R;\ 0]$.

$$\begin{cases} x = a\,cos\alpha(x) - \sqrt{\dfrac{R^2}{1+\left(\dfrac{a}{b}tg\alpha(x)\right)^2}} \rightarrow \alpha(x) \quad \text{for } -a-R<x<0 \\ h'(x) = -R + b\,sin\alpha(x) - \dfrac{a}{b}tg\alpha(x)\cdot\sqrt{\dfrac{R^2}{1+\left(\dfrac{a}{b}tg\alpha(x)\right)^2}} - d > 0 \end{cases}$$

Equation 4-4

Then we keep only $h'(x)>0$. The position of the apex at the tangency point is found as the minimum x such that $h'(x)\geq 0$.

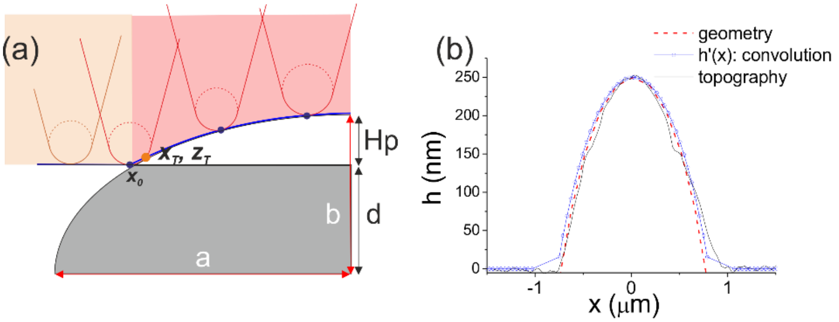

Figure 4-9 Convolution for buried ellipse. (a) Only half of the ellipse is shown, assuming it symmetric. The two regimes of the motion are depicted in different colours: orange: the tip moves on the substrate, red: the tip apex is tangent to the ellipse. The overall motion of the lowest tip point, i.e. the convolution, is represented by the blue line. The grey area represents the buried part of the ellipse, having a, b the axis. The dimensions to be extracted from the comparison with the topography are the lateral dimension a, and the buried depth $d=b-H_p$ where H_p is the ellipse height, set to the topography value. x_T,z_T are the coordinate of the first tangent point. (b) Example of convolution (blue line) matching the topography cross-section (black) for the same ellipse in Figure 4-8 (H_p =240nm, R=965nm, for which we found a=1000nm, d=490nm. The dashed line represents the geometry. The convolution in this case adapts better to the topography than the one calculated for ellipse or cap ellipse in Figure 4-8.

In Figure 4-9, we obtained a convolution profile much better adapting to the same topography cross-section of Figure 4-8b for a buried ellipse with a=1000nm, d=490nm.

Equation 4-4 applies also to the case of large radii, when only the tip apex is touching the bacterium: $R\ (1 - sin\theta) > Hp/2$, and the bacterium is modelled as ellipse. The convolution profile in this case is found setting $d=-b$ and $b=H_p/2$. This situation is depicted in Figure 4-10a. In Figure 4-10b it is shown an example of convolution profile (blue line and symbols) obtained in the case that R=250nm and $H_p/2$=145m, for which we found a=570nm. As in the case of

$R\ (1 - sin\theta) < Hp/2$, the same analytical convolution would be given by a cap ellipsoid having an elliptic-based conical shape of height z_T and base axis $a_c = x_T - \frac{z_T}{\left[-\left(\frac{b}{a}\right)^2 \cdot \frac{x_T}{z_T - b}\right]}$.

Note that in this case the trajectory of the centres of the apex circle tangent to the ellipse (black dashed line in Figure 4-10a) can also be described by a superellipse function of the form:

$$\begin{cases} x(\alpha) = \pm(a+R)cos^{2/n}\alpha \\ z(\alpha) = b \pm (b+R)sin^{2/n}\alpha \end{cases} \quad \text{for } 0 \leq \alpha \leq \pi/2$$

Therefore, the analytical convolution can also be found using the superellipse, as follows: it is first found the tangent point x_T, z_T between circle apex and ellipse when both lie on the same ground line (substrate). This can be done can either analytically or iteratively adjusting the position of the circle (we adopted this latter method) Then, the parameter *n* in the superellipse equation is varied until this passes through three points: the centre of the circle passing through the tangent point, the centre of a circle on top of a bacterial cell, and the centre of the circle at one side of the bacterial cell.

This superellipse gives the trajectory of the centre of the tip apex when a topographic image is recorded in contact with the bacterial cell. Next, the superellipse is translated in the vertical axes for a distance −R. This gives the movement of the contact point between apex and bacterium, and only $z>0$ is considered. The lateral dimension is obtained by varying a until the superellipse convolution matches the topography.

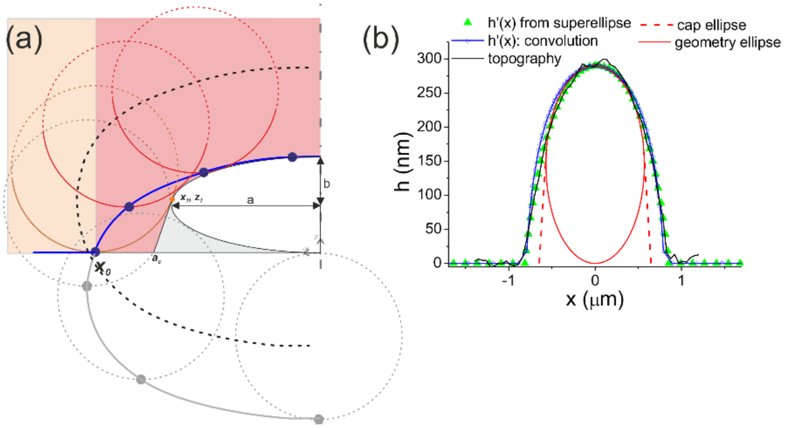

Figure 4-10 Convolution for ellipse in the case that only the tip apex contacts the ellipse. (a) Only half of the ellipse is shown, assuming it symmetric. The two regimes of the motion are depicted in different colours: orange: the tip moves on the substrate, red: the tip apex is tangent to the ellipse. The overall motion of the lowest tip point, i.e. the convolution, is represented by the blue line. The grey area represents the truncated conical base of the alternative cap ellipse, having a_c as the axis dimension. The ellipse (or cap ellipse) dimensions to be extracted from the comparison with the topography are the lateral dimension a, (or a_c) whereas the ellipse height $b= H_p/2$ is set to the topography value. x_T,z_T are the coordinate of the tangent point, and x_0 is the position at the first tangency point. The dashed black line represent the superellipse passing through the tip apex centres: by shifting it vertically of –R (continuous grey line), this is equivalent to the convolution in the red area (b) For both geometries (ellipse as continuous red line, cap ellipse with conical base as red dashed line), the convolution according to Equation 4-4(blue dotted line) and the superellipse convolution (green triangles) match equally the topography cross-section (black). The parameters of the calculations are R=250nm and Hp=2b=290m, for which we found a=570nm and a_c=648nm.

In Figure 4-10b it is shown that the two methods are equivalent: the convolution profile obtained with the superellipse method (for n=2.33, green triangles) and the one obtained from Equation 4-4 (blue dots) adjust to the topographic profile (black line) for the same lateral dimensions a=570nm of the ellipse (red continuous line) and a_c=648nm (red dashed lines).

Permittivity extraction

Once the system geometry is fully determined, one can insert this information in the models which calculate theoretically the capacitance between the tip and the sample.

For complex samples' shapes and dimensions covering a range of several orders of magnitudes, analytical models are difficult to theorize. For this, we recurred to finite element numerical calculations: one of the most important advantages of using finite element numerical simulations is that, since the solution is calculated in an ensemble of points in which the system geometry is discretized, it can be found also for realistically complex geometries.

By comparison of these calculations with the experimental measurements, namely capacitance images and approach curves acquired on a single point on top of the sample, we can obtain the permittivity of the sample.

4.4 Numerical models

For the samples object of this work of thesis, i.e. bacterial cells and pillars, we developed 2D and 3D models.

Same as for the radius calibration, the implementation of the 3D model was done in Comsol 5.0 by Dr. R. Fabregas from the research group, and won't be detailed here, whereas I adapted the 2D model of a disk and a spheroid, originally developed in the group for electrostatic force measurements [40, 41, 43, 47], to capacitance measurements.

4.4.1 Bacterium

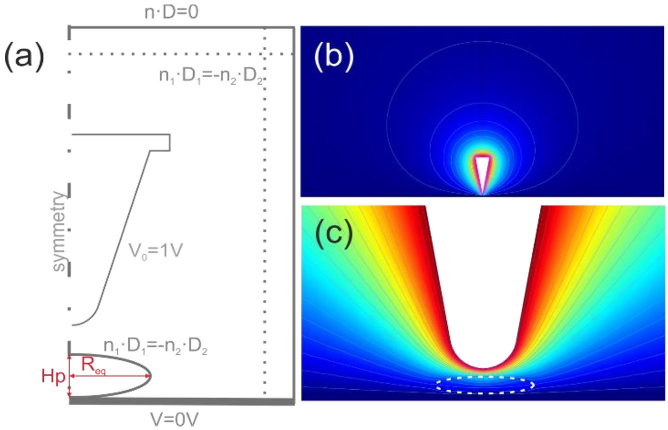

Figure 4-11 2D axisymmetric model for the bacterium. (a) Geometry and boundary conditions of the tip and bacterium, modelled as ellipsoid of radius $R_{eq} = \sqrt{\frac{l \cdot w}{4}}$. The tip geometrical parameters are the same as in Figure 4-2b. (b) Electric potential distribution and (c) detail of the tip-bacterium region. In this case, R=500nm, θ=10º, H=80µm, ε_r=2, H_p=290, R_{eq}=752nm.

The system geometry considered in the 2D numerical calculations is schematically depicted in Figure 4-11a. The SMM probe and the bacterium on a metallic substrate have axisymmetric geometry. The probe is modelled as a truncated cone as described in 4.1.1, whereas the bacterial cell is modelled as an oblate spheroid with height H_p, and equatorial axis (width), $D_{eq}=2R_{eq}$. The spheroid geometry is amenable to 2D axisymmetric numerical routines, which reduce the number of variables considered, but it is an approximation of the natural rod shape of bacteria, better represented by ellipsoids.

The height of the spheroid is the bacterium height, directly obtained from the topography image, whereas the radius R_{eq} is taken so that the volume of the bacteria is preserved, i.e. $Req = \sqrt{\frac{l\cdot w}{4}}$, where *l* and *w* are the bacterium width and length, respectively, found from the tip-sample deconvolution in the two main direction of the bacterium (therefore, referring to the section 4.3.2, $a=l/2$ in one axis and $a=w/2$ in the perpendicular axis). The electric permittivity of the bacterium is assumed to be uniform, and no conductivity is considered. Indeed, experimentally, the impedance shows a pure capacitive response and the magnitude of interest to be extracted is the tip sample capacitance.

The potential distribution is calculated in the electrostatic approximation. From the calculated potential the electric displacement can be determined, which, after integration over the

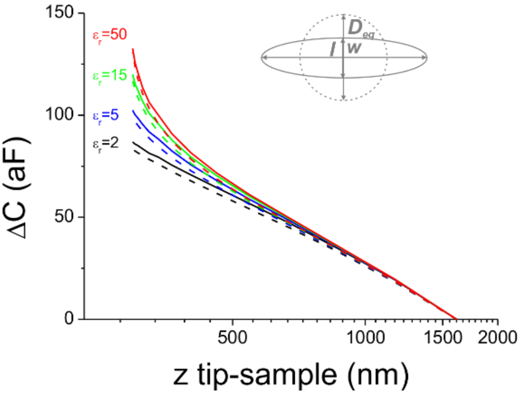

Figure 4-12. Comparison between 2D (dashed lines) and 3D (continuous lines) capacitance variation curves calculated on top of a bacterium, for various permittivity of the bacterium. For details about the 3D model, see section 6.5.1. The bacterium dimensions in the 3D model are l=2450nm, w=964nm, corresponding to an equivalent diameter for the 2D spheroid $D_{eq}=2R_{eq}$=1504nm, The other parameters of the geometry are set to the same values, namely R=500nm, θ=10º, H=80µm, H_p=290nm.

tip surface, gives the desired capacitance. In the model, we set the surface of the tip to V_0=1V (Figure 4-11), the bottom boundary of the simulation box to “ground”, the top and right boundary to “zero charge” ($\hat{n} \cdot \vec{D} = 0$) while the left boundary represents the symmetry axis. The bacterium surface has a continuity condition ($\hat{n}_1 \cdot \vec{D}_1 = -\hat{n}_2 \cdot \vec{D}_2$).

The validity of the model was tested by comparing the numerical integrals of the capacitance derivative obtained with the model (and for which the model was originally designed) to the capacitance directly calculated (see 4.1.1), similarly to what was done in absence of the sample.

From the calculated capacitances, we can calculate capacitance variations-distance curves $\Delta C_{th}(z, z_0, \varepsilon_r) = C_{th}(z, \varepsilon_r) - C_{th}(z_0, \varepsilon_r)$ where z is the tip substrate distance and z_0 is a reference distance far from the substrate (Figure 4-12, dashed lines). ΔC_{th} represents the magnitude that would be measured by performing an SMM approach curve on a single point on top of the bacterium. The curves show the characteristic behaviour of the capacitance variation approach curves measured with an SMM: in the long distance range, they exhibit an almost linear behaviour due to the capacitive contributions of the microscopic parts of the probes (cone and cantilever in this case), while at distances close to the sample they show a non-linear behaviour, due mainly to the contribution of the apex part of the probe. In this range of distances the capacitance variation curves are clearly dependent on the dielectric properties of the sample (the bacterium in this case), while at longer distances they are insensitive to them.

We can also calculate the maximum intrinsic capacitance contrast that would be measured at given distance with respect to the substrate, z_{CH}: $\delta C_{th}\ (z_{CH}, \varepsilon_r) = C_{th}(z_{CH}, \varepsilon_r) - C_{th}(z_{CH}, 1)$. The black lines in Figure 4-13 show the predicted capacitance contrast dependence on the dielectric constant of the same bacterium in Figure 4-12. Different tip-substrate distances have been considered to illustrate the dependence of capacitance intrinsic contrast on the imaging distance. The contrast increases both when the dielectric constant increases and when the tip-bacterium distance decreases, as expected. We note, however, that beyond a dielectric constant value typically around $\sim$10 the capacitance contrast modifies its dependence on the dielectric constant of the bacterium, passing from an almost logarithmic dependence to an almost saturation behaviour. This means that the capacitance contrast seems to be sensitive to the precise dielectric constant of the bacterium mainly for relatively low dielectric constants, while it becomes insensitive to its value if the dielectric constant values are very large. Interestingly, and in spite of the large differences in size, this type of behaviour has been showed to occur also for smaller scale objects like nanoparticles and viruses [42].

Figure 4-12 and Figure 4-13 also show the comparison with 3D model of the same bacterium. In the 3D model (see section 6.5.1), the bacterium is represented as an ellipsoid of w=964nm, l=2350nm, which correspond to the equivalent spheroidal diameter for the 2D model $D_{eq}=2R_{eq}$=1504nm. In both models, R=500nm, θ=10º, H_p=290nm, H=80µm. The difference is in all cases less than 4aF, which is around the experimental noise. We can see also that the difference between the models decreases at high distances from the substrate and it's independent from the permittivity.

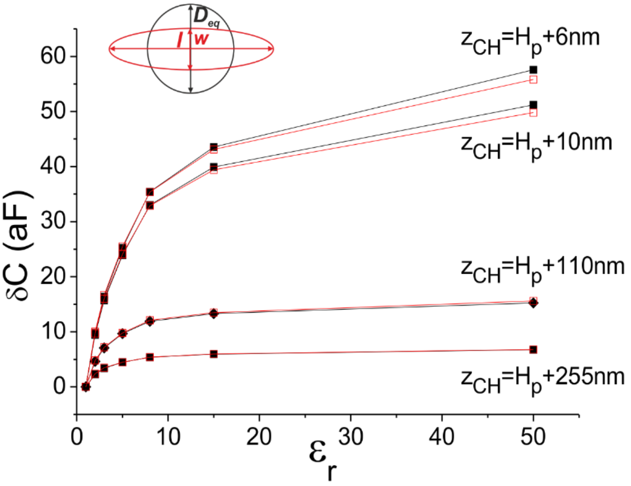

Figure 4-13 Comparison between 2D (black lines) and 3D (red lines) capacitance contrast calculated on top of a bacterium at various distances z_{CH}, and as function of the permittivity of the bacterium. For details about the 3D model, see section 6.5.1. The bacterium dimensions in the 3D model are l=2450nm, w=964nm, corresponding to an equivalent diameter for the 2D spheroid D_{eq}=1504nm, The other parameters of the geometry are set to the same values, namely R=500nm, θ=10º, H=80µm, H_p=290. We observe in both models that the capacitance contrast becomes unsensitive to the permittivity, for large values of this latter, and this occurs at lower ε_r, when increasing the distance z_{CH}.

4.4.2 Pillar

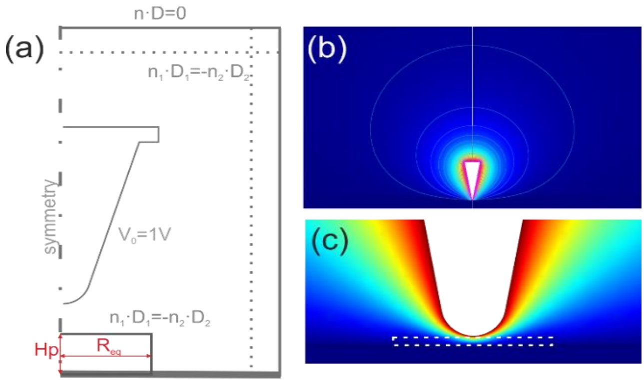

Figure 4-14 2D axisymmetric model for the pillar. (a) Geometry and boundary conditions of the tip and pillar, modelled as a circular disk of diameter $R_{eq}=2L_p/\sqrt{\pi}$. The tip geometrical parameters are the same as in Figure 4-2b. (b) Electric potential distribution in the domain and (c) detail of the tip-pillar region. In this case, R=1000nm, θ=10º, H=80µm, ε_r=2, H_p=140nm, R_{eq}=2820nm.

The pillar is modelled in the 2D axisymmetric geometry as a disk of height H_p and radius R_{eq} laying on a metallic substrate (Figure 4-14). The height is directly obtained from the topographic images, whereas the equivalent radius is calculated so that the volume is preserved: $D_{eq}= 2R_{eq}=4L_p/\sqrt{\pi}$, where L_p is the lateral dimension obtained from the deconvolution procedure (see 4.3.1), i.e. half of the pillar side. The probe is modelled as described in 4.1.1 and 4.4.1, and the boundary conditions are the same. Also for the pillar is assumed a pure capacitive response, and a homogeneous effective permittivity.

Analogously to the case of a bacterium, we calculated both capacitance variation approach curves (Figure 4-15, dashed lines) and capacitance contrast at fixed tip-substrate distance (Figure

4-16 black lines). The same considerations valid for the case of the spheroid apply here.

In Figure 4-15. and Figure 4-16 it is also shown the comparison with the 3D model, where the pillar is represented as a parallelepiped of dimensions ($2L_p$ x $2L_p$ x H_p). Still, the 2D model underestimates the capacitance, with a maximum difference of around 5aF.

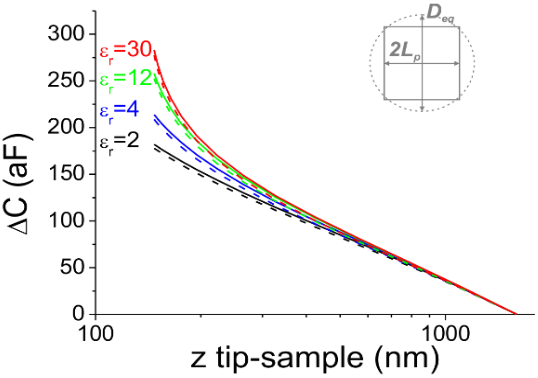

Figure 4-15. Comparison between 2D (dashed lines) and 3D (continuous lines) capacitance variation curves calculated on top of the pillar, for various permittivities. For details about the 3D model, see section 6.5.1. The pillar lateral dimension in the 3D model is $2L_p$ =5000nm, corresponding to an equivalent diameter of the 2D disk $D_{eq}=2R_{eq}$ =5642nm. The other parameters of the geometry are set to the same values, namely R=1000nm, θ=10º, H=80µm, H_p=140nm.

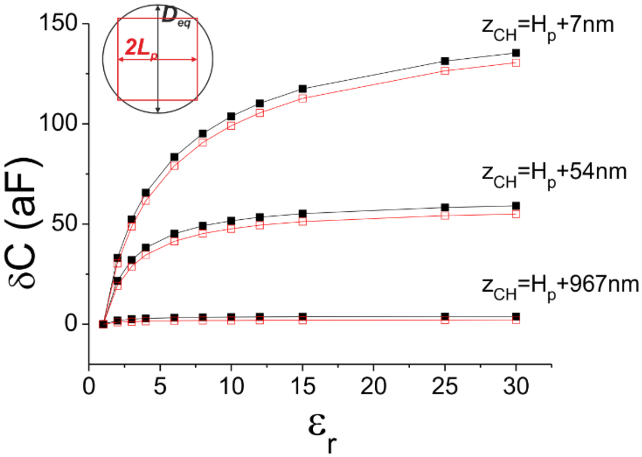

Figure 4-16 comparison between 2D (black lines) and 3D (red lines) capacitance contrast calculated on top of a pillar at various distances z_{CH}, and as function of the permittivity of the pillar. For details about the 3D model, see section 6.5.1 where it is applied to a bacterium. The pillar dimension in the 3D model is $2L_p$ =5000nm, corresponding to an equivalent diameter for the 2D disk $D_{eq}=2R_{eq}$ =5642nm, The other parameters of the geometry are set to the same values, namely R=1000nm, θ=10º, H=80µm, H_p=140nm. As for the case of spheroidal geometry, we observe in both models that the capacitance contrast becomes insensitive to the permittivity, for large values of this latter, and this occurs at lower ε_r, when increasing the distance z_{CH}.

4.5 Extraction of permittivity

4.5.1 From intrinsic capacitance images

The maximum intrinsic capacitance contrast of the experimental images can be combined with the numerically calculated intrinsic capacitance contrast, δC_{th} (z_{CH}, ε_r), (Figure 4-13 and Figure 4-16) to obtain the permittivity of the sample. For an experimental image obtained scanning the sample at a given z_{lift} in contact or intermittent mode, the corresponding numerical capacitance contrast must be calculated for the same distance tip-substrate, i.e. $z_{CH} = H_p + z_{lift}$.

Then, by simply interpolating the experimental intrinsic contrast $\delta C_{T,intr}(z_{lift}, h'(x), \varepsilon_r(x))$ on the numerically calculated one, we obtain then the effective permittivity of the sample, i.e. the value producing the same experimental intrinsic capacitance, in the case that the sample was electrically homogeneous. The contrast of the intrinsic images is free from stray, and for this no cantilever effect is considered in the numerical model of the tip: Subsequently, the only output of this method is the value of ε_r.

4.5.2 Capacitance approach curves

The effective permittivity of the sample can be quantified also from single point approach curves taken on top of the sample, following a method already applied in NIM and SCM [44, 48] for lower frequency measurements. Although the use of approach curves to quantify the permittivity is a well-established method, in order to achieve the same lateral resolution as the method based on intrinsic capacitance images, one should acquire and simulate curves on many different positions of the sample. This would heavily impact the experimental implementation, tip integrity, calculation time and easiness of analysis, thus ultimately affecting the stability and reliability of the results.

The procedure consists in approaching the tip on one point top of the sample, and recording the capacitance variation with respect to a point far from the surface z_{ref}: $\Delta C_{exp}(z, z_{ref})$ The curve is aligned with respect to the sample distance using the cantilever deflection curve simultaneously acquired, following the method already described to align the approach curve on metallic substrate (see section 4.2).

The curve is then least-square fitted to the family of simulated capacitance variation approach curves for the given geometry of the tip: $\Delta C_{th}(z, z_0, \varepsilon_r) = C_{th}(z, \varepsilon_r) - C_{th}(z_0, \varepsilon_r) + k_{stray}(z - z_0)$, calculated with respect to a point far from the sample (z_0) and for various permittivity of the sample (Figure 4-12 and Figure 4-15). Prior to the fit, the experimental and the numerical curves are set to a common reference point z'_{max}.

$$\Delta C_{exp}(z, z'_{max}) = \Delta C_{exp}(z, z_{ref}) - \overline{\Delta C_{exp}}(z'_{max}, z_{ref});$$

$$\Delta C_{th}(z, z'_{max}, \varepsilon_r) = \Delta C_{th}(z, z_0, \varepsilon_r) - \Delta C_{th}(z'_{max}, z_0, R\ \varepsilon_r);$$

Here, z is the absolute distance from the substrate, obtained from the sum of the relative distance from the sample, Z, and the sample's height obtained from the topography: $z=Z+H_p$; z'_{max} is the numerically simulated point closest to the upper fitting range limit chosen, z_{max}, and $\overline{\Delta C_{exp}}(z'_{max}, z_{ref})$ is the average of the experimental capacitance variation over 11 points around z'_{max}.

The fit is performed with permittivity and k_{stray} as free variables. Again, the fitting range influences the fitting results. However this dependence decreases with distance, and in general for $z_{max}>2R$ the fit results are independent from the fitting range.

The permittivity value thus extracted is an effective value, since the theoretical curves are calculated with a uniform value for ε_r all over the sample volume.

4.6 Software implementation: interface 2

A second Matlab-based interface was developed to extract the permittivity from the approach curves or the intrinsic capacitance contrast. Briefly, the user first sets the geometry and dimensions for tip and sample; the interface is linked to Comsol 3.4, thus the simulations to calculate the theoretical capacitance for the desired inputs by the user are launched on line *ex situ* (Figure 4-17*)*. In a second step, the experimental measurements are loaded and used, in combination with the simulated results, to perform the quantification. The output are the values for the permittivity resulting from the quantification (and k_{stray}, in case of fit of an approach curve) and the corresponding plots (Figure 4-18).

More in detail, the operational steps are described as follows:

- Part one (Figure 4-17): numerical simulations:
    1) the user chooses the type of geometry and the dimensions to simulate: he can select the kind of substrate under the sample (metallic or, rarely, dielectric) by setting its dielectric permittivity, the geometry of the sample (particle if spherical or ellipsoid, membrane if parallelepiped), the relative effective permittivity value(s) of the sample to simulate (single value, or a range of values), and the radial and axial dimension of the sample.
    2) The user chooses whether to calculate a

capacitance approach curve or a capacitance contrast, for each value of the sample permittivity chosen. The values **z_min** and **z_max** and **z_value** are the distance from the top part of the sample, and the approach curve is calculated in (**n_points**-1) points logarithmically spaced between **z_min** and **z_max.**

3) The user loads the tip geometry (radius, half angle, large angle and cone height) found by the interface for the tip calibration, or, alternatively, edits or enters other values manually.
4) Once all the parameters have been entered, the simulation starts. At the end, a surface plot of the last point calculated will appear in the graph area. In Figure 4-17 (bottom) is shown an example for a membrane geometry.
5) Alternatively, the user can load an existing simulation table and use this for the subsequent analysis of the experimental data.

- Part two (Figure 4-18): permittivity extraction:

6) In the case we selected a single value for the distance tip-sample, it will be implemented

an interpolation of the intrinsic capacitance contrast: the user must enter the average experimental intrinsic contrast calculated from the image, plus/minus its standard deviations. The fit interpolates $\delta C_{th}\,(z_{CH}, \varepsilon_r)$ in the three points, to find the three corresponding ε_r, as described in section 4.5.1. In this case, no stray is calculated, since by definition the intrinsic image has no stray, and in the simulation model no cantilever is included. The results of the interpolation of the given values with the simulated set appear in the bottom right corner and are plotted in the graph area, as it is shown in Figure 4-18(top)

7) In case we selected a range of values for the tip sample distance, it will be implemented a fit of a capacitance variation approach curve. The user starts by loading the experimental file (note that all distance in this part are referred as absolute distances from the substrate), which will be plotted in the graph area. Next, he selects a name for saving the output file, which includes the values found for permittivity and k_{stray}, their interval confidence at 95%, the best fit curve, the error curves and the residues.

8) The user next selects the range of tip-substrate distances for fit, either by clicking on the plot of the experimental file (and the points selected will appear in the boxes **z_min**, **z_max**), or by typing there the end points wished.
9) Finally, the user choses an initial condition for the variable permittivity the fit, **eps0** (the initial condition for k_{stray} variable is automatically defined as the slope of the last 100 points of the curve).
10) The user starts the fit, performed in two variables (ε_r and k_{stray}) as detailed in section 4.5.2. The results of the fits for the two variables appears in the bottom, and the fitting curve and the error curves are plotted on the graph area (Figure 4-18 (bottom).

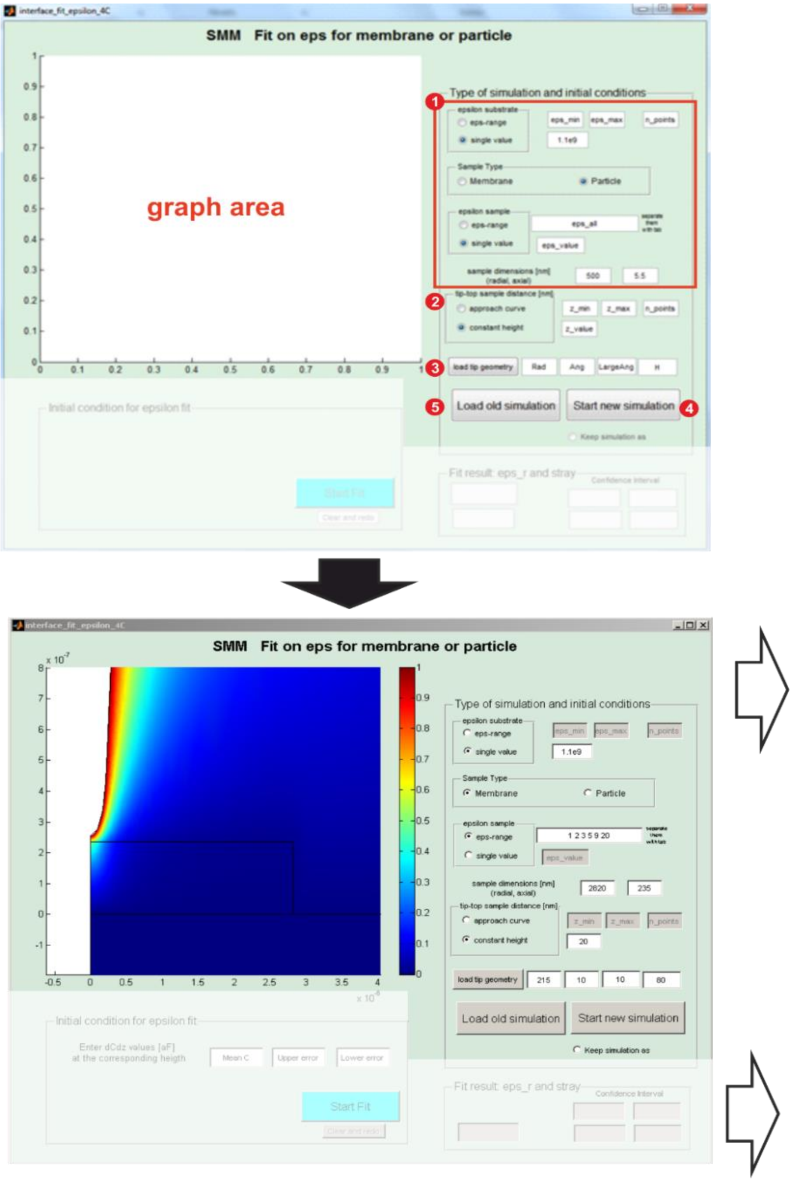

(top)
epsilon substrate: ○ eps-range ● single value 1.1e9
Sample Type: ○ Membrane ● Particle
epsilon sample: ○ eps-range ● single value
sample dimensions [nm] (radial, axial): 500 5.5
tip-top sample distance [nm]: ○ approach curve ● constant height

(bottom)
epsilon substrate: ○ eps-range ● single value 1.1e9
Sample Type: ● Membrane ○ Particle
epsilon sample: ● eps-range 1 2 3 5 9 20 ○ single value
sample dimensions [nm] (radial, axial): 2820 235
tip-top sample distance [nm]: ○ approach curve ● constant height 20
load tip geometry: 215 10 10 80
○ Keep simulation as

Figure 4-17 Interface for permittivity quantification, part one: numerical simulations. (top) commands of the parameters to input for the simulations. (bottom) Example of simulation of a dielectric pillar.

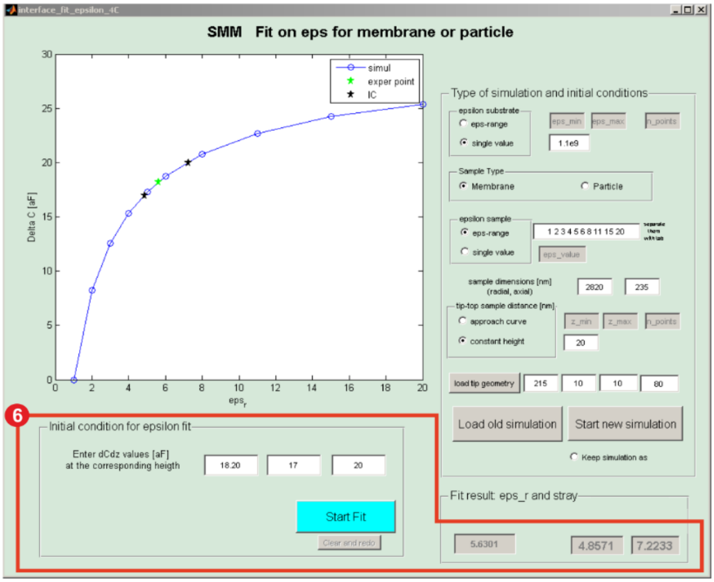

Type of simulation and initial conditions

epsilon substrate: ○ eps-range ● single value: 1.1e9

Sample Type: ● Membrane ○ Particle

epsilon sample: ● eps-range: 1 2 3 4 5 6 8 11 15 20 ○ single value

sample dimensions [nm] (radial, axial): 2820 235

tip-top sample distance [nm]: ○ approach curve ● constant height: 20

load tip geometry: 215 10 10 80

○ Keep simulation as

Initial condition for epsilon fit

Enter dCdz values [aF] at the corresponding heigth: 18.20 17 20

Fit result: eps_r and stray: 5.6301 4.8571 7.2233

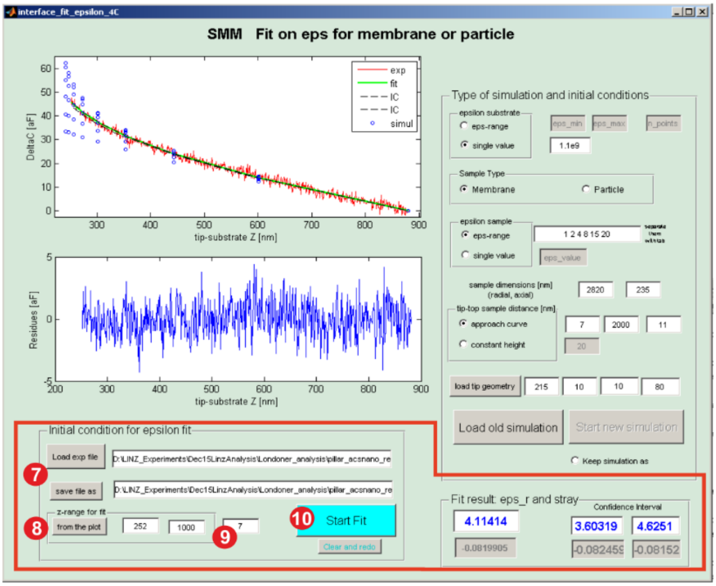

Type of simulation and initial conditions

epsilon substrate: ○ eps-range ● single value: 1.1e9

Sample Type: ● Membrane ○ Particle

epsilon sample: ● eps-range: 1 2 4 8 15 20 ○ single value

sample dimensions [nm] (radial, axial): 2820 235

tip-top sample distance [nm]: ● approach curve: 7 2000 11 ○ constant height: 20

load tip geometry: 215 10 10 80

○ Keep simulation as

Initial condition for epsilon fit

Load exp file: D:\LINZ_Experiments\Dec15LinzAnalysis\Londoner_analysis\pillar_acsnano_re

save file as: D:\LINZ_Experiments\Dec15LinzAnalysis\Londoner_analysis\pillar_acsnano_re

z-range for fit: from the plot: 252 1000 7

Fit result: eps_r and stray: 4.11414 -0.0819905

Confidence Interval: 3.60319 4.6251 -0.082459 -0.08152

Figure 4-18 Interface for permittivity quantification, part two: permittivity extraction. Determination of the permittivity from (top) the intrinsic contrast, where the result is depicted as green star, and (bottom) from the capacitance variation approach curve on top of the sample, where the resulting fit curve is depicted in green. The results appear in the bottom right corner in both cases.

5. DIRECT MAPPING OF THE PERMITTIVITY ON HETEROGENEOUS THIN FILMS

The first application of the methodologies described in chapters 3 and 4 has concerned inorganic heterogeneous samples, consisting in pillars of different oxides and different thicknesses, and whose dimensions are comparable to the ones of bacterial cells. In fact, for their tall three-dimensional shape, such samples present the same problem of topography crosstalk as cells. Yet, given their inorganic rigid nature, they are much easier to handle, in the experimental phase, and most of the precautions which must be respected when dealing with biological samples can be relaxed.

I obtained intrinsic capacitance images at around 19 GHz in contact mode and show that these images directly map the electric permittivity, therefore the materials can be identified on the basis of their dielectric response without the need of the quantification processes described in chapter 4.

Since most biological samples must be imaged in softer conditions, such as intermittent or lift mode, I also investigated such imaging conditions, finding that for non-contact modes the interpretation of the capacitance images in terms of the electric permittivity of the materials is less straightforward.

For the analysis of the experimental images I used the analytical formulae for thin films, introduced in section 3.1, and the 2D numerical model for a pillar presented in section 4.4.2.

This chapter reproduces almost literally the manuscript "Direct Mapping of the GHz Electric Permittivity on Heterogeneous Thin Film Samples by AFM-Scanning Microwave Microscopy" by M.C. Biagi, G. Badino, G.Gramse, L. Fumagalli and G. Gomila. In this manuscript I was in charge of performing the experimental and the theoretical parts and of processing the results. The manuscript was written by me in collaboration with the other authors.

5.1 Abstract

We obtained maps of the electric permittivity at ~19 GHz frequencies on non-planar thin film heterogeneous samples by means of combined atomic force-scanning microwave microscopy (AFM-SMM). We show that the electric permittivity maps can be obtained directly from the capacitance images acquired in contact mode, after removing the topography crosstalk effects. This result demonstrates the possibility to identify the electric permittivity of different materials in a thin film sample irrespectively of their thickness by just direct imaging and processing. We show, in addition, that quantitative maps of the electric permittivity can be obtained with no need of any theoretical calculation or complex quantification procedure when the electric permittivity of one of

the materials is known. To achieve this results the use of contact mode imaging is a key factor. For non-contact imaging modes the effects of the local sample thickness and of the imaging distance makes the interpretation of the capacitance images in terms of the electric permittivity properties of the materials much more complex. Present results represent a substantial contribution to the field of nanoscale microwave dielectric characterization of thin film materials with important implications for the characterization of novel 3D electronic devices and 3D nanomaterials.

5.2 Introduction

Near-Field Scanning Microwave Microscopes (SMM) emerged in 1972 [21] by the need to provide local maps of the electric permittivity properties of heterogeneous materials in a non-destructive way and with micrometric spatial resolution. Fundamentally, a microwave microscope consists of a near-field probe, which can be scanned over the sample, and which is connected to a microwave source/measurement system. When the probe is hold close or in contact to the surface of the sample, this latter perturbs the evanescent electromagnetic field. By consequence, the system becomes sensitive to the local complex impedance of the probe-sample system, and hence, to its local complex electric permittivity. Micrometric to deep sub-micrometric spatial resolution measurements can be obtained by engineering special measuring probes. First setups employed traditional microwave elements such as microstrips [49] , coaxial waveguides with tapered end [22] or waveguides with aperture

[50] as probes. Lately, combined Atomic Force-Scanning Microwave Microscope systems (AFM-SMM) [25, 26, 33] were able to use AFM probes (conventional or engineered [24]) as source of the evanescent field. The size of AFM probes can be easily manufactured down to tens of nanometres, enabling a high spatial lateral resolution. Examples of application of the SMM includes the rapid, non-destructive and local detection of the electric permittivity in insulating materials, ferroelectric and new functional materials discovered by combinatorial synthesis [51-53], which are employed in supercapacitors, batteries, non-volatile memories, diodes and photovoltaic cells [54, 55], complex oxides [56], graphene [57, 58], carbon nanotubes [59], doped semiconductors [60] and superconductors [61]. Furthermore, in the emerging field of high frequency nanoelectronic devices there is the demand of on-wafer measurement systems sensitive to the microwave electromagnetic properties of dielectric materials [62]. In spite of the large number of successful applications of the SMM, a main challenge still remains, namely, the difficulty in mapping the electric permittivity of heterogeneous samples exhibiting large height variations. Until now, most applications have dealt with either heterogeneous 2D planar samples [25, 26, 53, 63], or with homogeneous 3D samples [64], but the general situation of 3D heterogeneous systems has not been addressed yet. The emergence of the new 3D electron device technologies (e.g. 3D transistors FinFET [65], and 3d NAND memories [66]) and of new 3D functional nanomaterials [67-69] is prompting for a resolution of the above mentioned challenge [70]. The major issue posed by

non-planar heterogeneous systems is that the measured microwave signal may show variations due to both changes in the sample topography and changes in the local electric permittivity properties, whose disentanglement is rather complex [34].

Here, we present a method to disentangle topographic and electric permittivity variations in the particular case of thin film heterogeneous samples with variable thickness. We show that maps of the electric permittivity of the different materials in the sample in the GHz frequency range can be obtained directly from capacitance images acquired with an AFM-SMM system by just simple image processing. To achieve this, we show that contact mode intrinsic capacitance images, obtained from conventional AFM-SMM capacitance images by removal of the topography crosstalk contributions, can be directly related to the local electric permittivity of the materials in the sample, with no effect of the thickness of the different materials. The use of contact mode imaging is key to achieve this result. Indeed, we show that for non-contact imaging modes, such as for instance intermittent contact mode or two pass modes, very often used with AFM-SMM systems, the relation between intrinsic capacitance images and electric permittivity is more complex and depends on the sample topography and imaging distance, thus making more complex the derivation of electric permittivity maps.

5.3 Results

The problematics posed by non-planar heterogeneous thin film samples concerning the measurement of its local electric permittivity properties by means of an AFM-SMM system can be understood by considering a thin film sample consisting of micropatterned oxides of different thicknesses. Figure 5-1a shows a contact mode topographic image of one of such samples. It consists of Al_2O_3 square pillars (located to the left of the image by design) and of square SiO_2 pillars (located on the right of the image), e-beam evaporated and micropatterned on a gold substrate (see Experimental section for microfabrication details). In this sample the pillars have thicknesses h_{Al2O3}=104 nm and h_{SiO2}=65 nm, respectively (see topography cross-section profile in Figure 5-1b).

Figure 5-1c shows a contact mode (calibrated) capacitance image of the sample obtained at ~19 GHz with an AFM-SMM set up (see Experimental section for a description of the set-up , and the SMM calibration procedure used to obtain the capacitance images). The contact mode capacitance image (Figure 5-1c) shows a very similar contrast for the two pillars, just slightly larger for the Al_2O_3 pillar than for the SiO_2 pillar, $\left|\delta C_{contact}^{Al_3O_2}\right| = 87 \pm 1\, aF$ and $\left|\delta C_{contact}^{SiO_2}\right| = 84 \pm 1\, aF$, respectively, see cross-section profile in Figure 5-1d (black line). This result is not in line with the expected higher electric permittivity of Al_2O_3 with respect to SiO_2 ($\varepsilon_{r,SiO2} < \varepsilon_{r,Al2O3}$). This means that the difference in electric permittivities

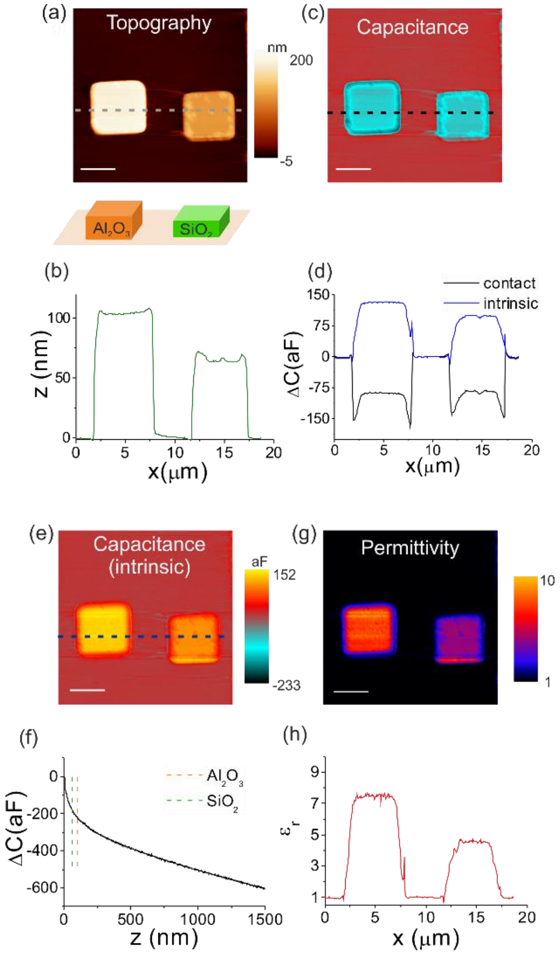

Figure 5-1

(a)AFM contact mode topography image and (b) corresponding cross-section profile of a thin film sample consisting of micropatterned Al2O3 (left) and SiO2 (right) pillars of different thicknesses on a gold substrate. Pillars thicknesses: h_{Al2O3}=104 nm and h_{SiO2}=65 nm. (c) SMM Contact mode calibrated capacitance image at ~19 GHz and (d) corresponding cross-section profile (black line). (e) Intrinsic contact mode capacitance image. The corresponding cross-section profile is shown in (d), blue line. (f) Capacitance approach curve on the bare substrate used, in combination with the topographic image in (a), to construct the intrinsic capacitance image. Note that the curve has been shifted in order to set the capacitance at contact with the substrate to the same value obtained from the capacitance image, namely 0 aF. This curve is also used to calibrate the tip radius giving R=1173 nm, θ=10º and k_{stray}= 0.124 aF/nm. The vertical dashed lines refer to the thicknesses of the two pillars in the sample. (g) Relative electric permittivity map, and (h) corresponding cross-section profile, obtained from the intrinsic capacitance image in (e) with the use of Equation 5 6 and the calibrated tip radius. Scale bar of all images=3.8μm.

between the two materials can be compensated by the difference in their respective thicknesses. This problem does not appear if one considers the intrinsic capacitance image shown in Figure 5-1e, in which topography crosstalk effects have been removed (to construct the intrinsic capacitance image we used the capacitance approach curve shown in Figure 5-1f and the topographic image in Figure 5-1a, see Experimental section). The resulting intrinsic image (Figure 5-1e) shows a clear higher contrast for the Al_2O_3 pillar ($\left|\delta C_{contact,\mathrm{int}}^{Al_2O_3}\right| = 133 \pm 1\,aF$) as compared to the SiO_2 pillar ($\left|\delta C_{contact,\mathrm{int}}^{SiO_2}\right| = 99 \pm 1\,aF$), in agreement with the expected larger electric permittivity of Al_2O_3 (see blue line in Figure 5-1d).

The intrinsic contact mode capacitance images can be used to obtain almost directly quantitative maps of the electric permittivity of the materials. To do so, we use the analytical model proposed in Ref. [40] for the tip-sample capacitance on thin film samples (see further discussion on this point in the Discussion section). According to this model, the tip-sample capacitance in a thin film system can be expressed as a sum of apex, cone and stray contributions [40, 64],

$$C(z,h,\varepsilon_r) = C_{apex}(zh,\varepsilon_r) + C_{cone}(z,h,\varepsilon_r) + C_{stray}(z) + C_0$$

Equation 5-1

where:

$$C_{apex}(z,h,\varepsilon_r) = 2\pi\varepsilon_0 \ln\left(1 + \frac{R\cdot(1-\sin\theta)}{z + h/\varepsilon_r}\right)$$

Equation 5-2

$$C_{cone}\left(z,h,\varepsilon_r\right) =$$

$$\frac{-2\pi\varepsilon_0}{ln\left[\left(tg\theta/2\right)\right]^2}\cdot\left[\left(z+\frac{h}{\varepsilon_r}+R\cdot\left(1-sin\theta\right)\right)\cdot\ln\left(\frac{H}{+\frac{h}{\varepsilon_r}+R\cdot\left(1-sin\theta\right)}\right)\right]+$$

$$+\frac{2\pi\varepsilon_0}{ln\left[\left(tg\theta/2\right)\right]^2}\cdot\left[R\cdot\left(1-sin\theta\right)+\frac{Rcos^2\theta}{sin\theta}\cdot ln\left(z+\frac{h}{\varepsilon_r}+R\cdot\left(1-sin\theta\right)\right)\right]$$

Equation 5-3

$$C_{stray}(z) = -k_{stray}z$$

Equation 5-4

Here, C_0 is a constant value independent from z, z is the tip sample distance, R is the tip apex radius, θ is the tip half angle, H is the tip cone height and k_{stray} is a phenomenological parameter accounting for the long range stray interaction of the cantilever and chip holder with the substrate. Moreover, h is the thin film thickness and ε_r its relative electric permittivity. From this model, the intrinsic capacitance contrast at a given position on the sample plane, $\vec{x} = \left(x, y\right)$, can be expressed as:

$$\delta C_{\text{int}}(\vec{x}) = \left[C\left(h(\vec{x}) + z_c; \varepsilon_r(\vec{x})\right) - C\left(Z_{ref} - h(\vec{x}); \varepsilon_r(\vec{x})\right) \right] + \\ - \left[C\left(h(\vec{x}) + z_c; 1\right) - C\left(Z_{ref} - h(\vec{x}); 1\right) \right]$$

Equation 5-5

where Z_{ref} is a tip-substrate reference distance far from the substrate, $\varepsilon_r(x)$ the local electric permittivity and $h(x)$ the local thickness of the sample. Equation 5-2, Equation 5-3 and Equation 5-4 can be substituted into Equation 5-1 and this into Equation 5-5. If we then consider $Z_{ref} >> h(x), R$, the second and fourth member of the left side in Equation 5-5 and the stray components, cancel out. Furthermore, under the conditions $R >> h(x)$ (thin film), and $z_c = 0$ (contact mode imaging), one obtains a remarkable simple relation:

$$\delta C_{\text{int},contact}(\vec{x}) = 2\pi\varepsilon_0 R \ln(\varepsilon_r(\vec{x}))$$

Equation 5-6

Equation 5-6 shows that the contact mode intrinsic capacitance image in a non-planar thin film sample is directly related to the local relative electric permittivity of the sample, with no dependence on the local sample thickness, $h(x)$. This result confirms the experimental findings described above. According to Equation 5-6 quantitative electric permittivity maps can be obtained directly from the intrinsic contact mode capacitance image by just inverting this equation, i.e.,

$$\varepsilon_r(\vec{x}) = e^{\frac{\delta C_{contact,\text{int}}(\vec{x})}{2\pi\varepsilon_0 R}}$$

Equation 5-7

where only the intrinsic capacitance and the tip radius R need to be known (the tip radius can be determined *in situ*, for instance, by using a capacitance approach curve measured on the metallic substrate as shown elsewhere [39, 64, 71]). Figure 5-1g we show the electric permittivity image obtained from the intrinsic capacitance image shown in Figure 5-1e with the use of Equation 5-7 and the calibrated tip radius. The images predict an electric permittivity for the Al_3O_2 pillar of $\varepsilon_{r,Al3O2}$=7.5±1 while for the SiO_2 pillar they predict $\varepsilon_{r,SiO2}$=4.5±0.5 (the errors have been calculated from error propagation analysis of Equation 5-7). The values obtained for the electric permittivities are in reasonable agreement with the nominal values reported for these materials in the literature, ($\varepsilon_{r,SiO2}$~4 [72], $\varepsilon_{r,Al2O3}$~9 [63]).

Similar conclusions are drawn by analysing a second sample in which the thicknesses of the two materials are almost identical. A topographic image of this second sample is shown in Figure 5-2a, together with a cross-section profile Figure 5-2b. In this case the thicknesses are: h_{Al2O3}=130 nm and h_{SiO2}=140 nm. The contact mode SMM capacitance image at ~19 GHz (Figure 5-2c) shows that the contrast on the centre of the Al_2O_3 pillar ($\left|\delta C_{contact}^{Al_3O_2}\right| = 99 \pm 1\, aF$) is smaller than that of the SiO_2 pillar ($\left|\delta C_{contact}^{SiO_2}\right| = 120 \pm 1\, aF$), as it can be seen on the cross-section profile (black line) in Figure 5-2d.

Again the contrasts are not in line with the expected higher electric permittivity of Al_2O_3 as compared to that of SiO_2. Instead, if we construct the intrinsic capacitance image with the help of the capacitance approach curve on the gold substrate (shown in Figure 5-2f) and the topographic image in Figure 5-2a, the correct contrast

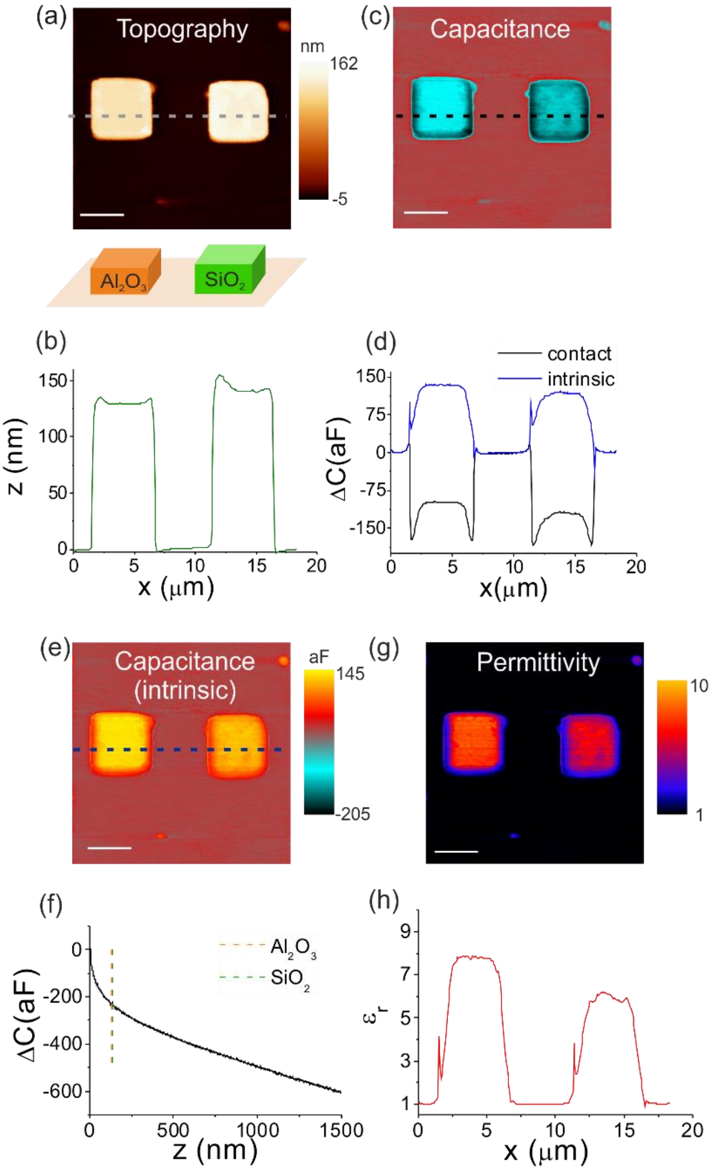

Figure 5-2

(a) AFM contact mode topography image and (b) corresponding cross-section profile of a thin film sample consisting of micropatterned Al_2O_3 (left) and SiO_2 (right) pillars of different thicknesses on a gold substrate. Pillars thicknesses: h_{Al2O3}=130 nm and h_{SiO2}=140 nm. (c) SMM Contact mode calibrated capacitance image at ~19 GHz and (d) corresponding cross-section profile (black line). (e) Intrinsic contact mode capacitance image. The corresponding cross-section profile is shown in (d), blue line. (f) Capacitance approach curve on the bare substrate used, in combination with the topographic image in (a), to construct the intrinsic capacitance image. Note that the curve has been shifted in order to set the capacitance variation at contact with the substrate to the same value obtained from the capacitance image, namely 0 aF. This curve is also used to calibrate the tip radius giving R=1172 nm, θ=10º and k_{stray}= 0.137 aF/nm. The vertical dashed lines, almost indistinguishable, refer to the thicknesses of the two pillars in the sample. (g) Relative electric permittivity map, and (h) corresponding cross-section profile, obtained from the intrinsic capacitance image in (e) with the use of Equation 5-6 and the calibrated tip radius. Scale bar of all images=3.8µm.

order is obtained. Figure 5-2e shows the obtained intrinsic capacitance image, which shows a higher contrast for the Al_2O_3 pillar ($\left|\delta C_{contact,\mathrm{int}}^{Al_2O_3}\right| = 134 \pm 1\, aF$) as compared to the SiO_2 pillar ($\left|\delta C_{contact,\mathrm{int}}^{SiO_2}\right| = 120 \pm 1\, aF$), see cross-section profile in Figure 5-2d (blue line), this time in accordance with the expected higher electric permittivity of Al_2O_3. This result indicates that topography crosstalk effects may dominate the contact mode SMM capacitance images, even for a sample with just 10 nm difference in thickness like the present one, thus highlighting the importance of these effects. Finally, we construct the electric permittivity image with the help of Equation 5-7 and the calibrated tip radius (same as before). The resulting image, together with a cross-section profile, are shown in Figure 5-2g and Figure 5-2h, respectively. The image predicts an electric permittivity for the Al_3O_2 pillar of $\varepsilon_{r,Al3O2}$=8±1 while for the SiO_2 pillar it predicts $\varepsilon_{r,SiO2}$=6±1.

The value obtained for the Al_3O_2 pillar is almost identical to the one obtained for the first sample analysed above. However, for the SiO_2 pillar we obtained a somewhat larger value. We have verified thoughtfully the quantitative capabilities of the methodology proposed by analysing with it the electric permittivity properties of a micropatterned high quality thermally grown SiO_2 sample on a highly doped silicon wafer. Results shown in Figure 5-3 provide an electric permittivity value of $\varepsilon_{r,SiO2}=4.1\pm0.3$, in excellent agreement with the nominal value of SiO_2. Therefore, we attribute the slightly larger value obtained for the SiO_2 pillar in the sample of Figure 5-2 to a poorer quality of this specific e-beam deposited SiO_2. We remember that the dielectric properties of SiO_2 are highly sensitive to the quality of the deposited material and to the presence of eventual contaminations, as it has been show earlier for SiO_2 deposited by different methods, where in all cases, a larger electric permittivity was reported (Refs. [73]–[75]). This result, shows the high sensitivity of the methodology proposed to the actual dielectric properties of the materials.

We have then shown that contact mode SMM capacitance images do not reflect directly the electric permittivity properties of the materials in non-planar heterogeneous thin film samples. Instead, intrinsic capacitance images, obtained by removing the topography crosstalk effects, provides direct information on the electric permittivity of the materials and allow deriving in a straightforward way electric permittivity maps of the sample, irrespectively of the thickness of the different materials.

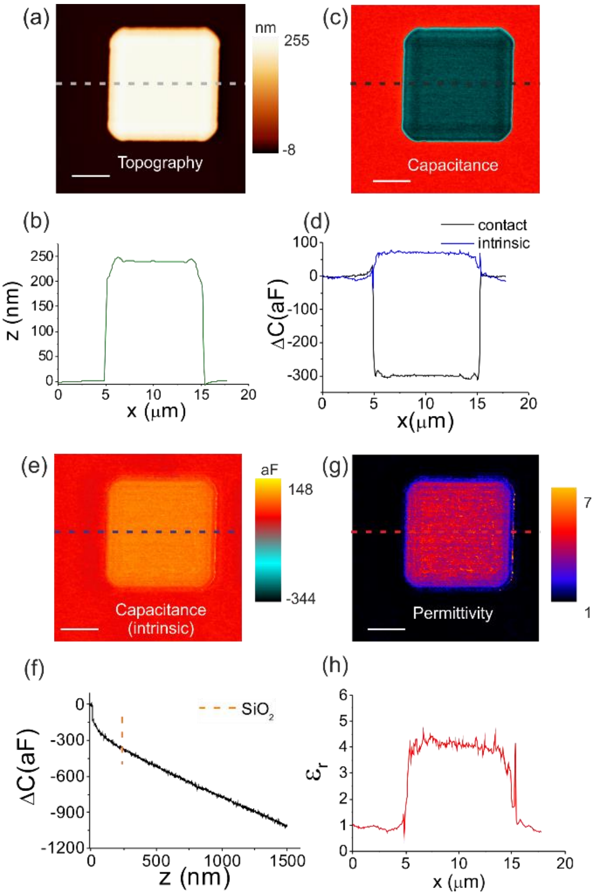

Figure 5-3

(a) AFM contact mode topography image and (b) corresponding cross-section profile of a thin film sample consisting of micropatterned SiO2 pillar of h_{SiO2}=240 nm thickness on a highly doped silicon substrate. (c) SMM Contact mode calibrated capacitance image at ~19 GHz and (d) corresponding cross-section profile (black line). (e) Intrinsic contact mode capacitance image. The corresponding cross-section profile is shown in (d), blue line. (f) Capacitance approach curve on the bare substrate used, in combination with the topographic image in (a), to construct the intrinsic capacitance image. Note that the curve has been shifted in order to set the capacitance variation at contact with the substrate to the same value obtained from the capacitance image, namely 0 aF. This curve is also used to calibrate the tip radius giving R=802 nm, θ=10º and k_{stray}= 0.4274 aF/nm. The vertical dashed line refers to the thicknesses of the pillars. (g) Relative electric permittivity map, and (h) corresponding cross-section profile, obtained from the intrinsic capacitance image in (e) with the use of Equation 5-6 and the calibrated tip radius. Scale bar of all images=3.8μm.

We also note that in the case that the electric permittivity of one of the materials in the sample is known, then one can derive the electric permittivity values of the other materials without even knowing the geometry of the measuring tip. Indeed, from Equation 5-6, it is immediate to show that the electric permittivity of two regions of a sample satisfies the relationship

$$\varepsilon_r(\vec{x}) = \varepsilon_r(\vec{x}_{ref})^{\left(\frac{\delta C_{\mathrm{int}}(\vec{x})}{\delta C_{\mathrm{int}}(\vec{x}_{ref})}\right)}$$

Equation 5-8

which is solely dependent on the ratio of intrinsic capacitance contrasts and on the electric permittivity of the reference material. This result represents a crucial advantage in imaging heterogeneous thin film non-planar samples, since by only knowing the electric permittivity of one material, one can obtain an electric permittivity map directly from the intrinsic capacitance image by just rescaling the image according to Equation 5-8.

5.4 Discussion

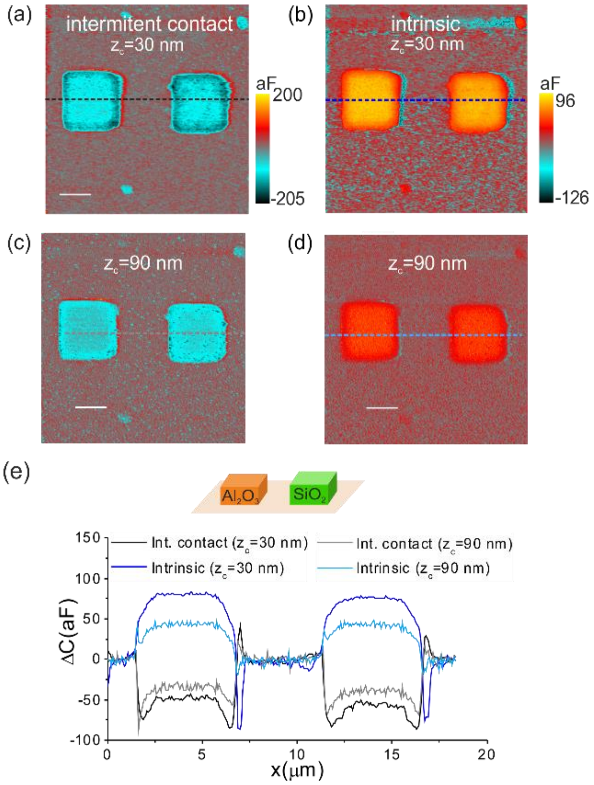

Figure 5-4 SMM capacitance and intrinsic capacitance images acquired at ~19GHz on the sample shown in Figure 5-2 but acquired in intermittent mode at two different oscillation amplitudes: (a)-(b): z_c=30 nm and (c)-(d) z_c=90 nm. (e) Cross-section profiles along the lines in the images.

We have seen that contact mode intrinsic capacitance images obtained with an AFM-SMM system on non-planar thin film heterogeneous samples can be directly interpreted in terms of the electric permittivity of the materials, with no effects associated to the sample thickness. It is important to highlight that this statement holds true as long as the images are obtained in contact mode. To show it, we have obtained SMM capacitance images in intermittent contact mode and analysed them following the same procedure described above.

In Figure 5-4a and Figure 5-4c we show intermittent contact mode SMM capacitance images acquired at ~19 GHz on the sample of Figure 5-2 (h_{Al2O3}=130 nm and h_{SiO2}=140 nm) at two different oscillation amplitudes, corresponding to mean tip sample distances z_c =30 nm and z_c=90 nm, respectively. It can be observed from the capacitance images, and from the capacitance cross-section profiles shown in Figure 5-4e (black and grey lines for z_c =30nm and z_c=90 nm, respectively), that the capacitance contrast decreases by increasing the average tip-sample distance, as expected. For the two distances considered, the intermittent contact capacitance contrast is larger for the SiO_2 pillar ($\left|\delta C^{SiO_2}_{non-contact}\right|_{z_c=30nm}=55\pm2\,aF$, $\left|\delta C^{SiO_2}_{non-contact}\right|_{z_c=90nm}=39\pm3\,aF$) than for the Al_2O_3 pillar ($\left|\delta C^{Al_3O_2}_{non-contact}\right|_{z_c=30nm}=48\pm2\,aF$, $\left|\delta C^{Al_3O_2}_{non-contact}\right|_{z_c=90nm}=34\pm3\,aF$), again opposite to the expected dielectric response of the materials. Figure 5-2b and Figure 5-2d show the corresponding intrinsic capacitance images resulting from the subtraction of the topography crosstalk contributions. For the smaller tip-sample distance, z_c =30nm, the intrinsic contrast for the Al_2O_3 pillar ($\left|\delta C^{Al_3O_2}_{non-contact,\mathrm{int}}\right|_{z_c=30nm}=80\pm1\,aF$) is larger than that of the SiO_2 pillar ($\left|\delta C^{SiO_2}_{non-contact,\mathrm{int}}\right|_{z_c=30nm}=76\pm1 aF$), in line with the expected electric permittivity value. However, for the larger tip-sample distance (z_c=90 nm), the intrinsic capacitance contrasts of both pillars are the same within the experimental error ($\left|\delta C^{Al_3O_2}_{non-contact,\mathrm{int}}\right|_{z_c=90nm} = 44 \pm 2\ aF$ and $\left|\delta C^{SiO_2}_{non-contact,\mathrm{int}}\right|_{z_c=90nm} = 43 \pm 2aF$). Therefore, while at short tip-sample distances the intrinsic intermittent contact capacitance images still may reflect to some extend the electric permittivity properties of the materials, at larger distances this is no longer the case, and the interpretation of the images has to be made with caution.

This result can be simply understood by considering the analytical model for the tip-sample capacitance in Equation 5-1, Equation 5-2, Equation 5-3 and Equation 5-4 for the case that the tip-sample distance is different from zero, $z_c \neq 0$. One obtains the following expression for the intrinsic capacitance contrast

$$\delta C_{non-contact,\mathrm{int}}(\vec{x}) = 2\pi\varepsilon_0 R \ln\left(\frac{zc + h(\vec{x})}{zc + \dfrac{h(\vec{x})}{\varepsilon_r(\vec{x})}}\right)$$

Equation 5-9

i.e., the intrinsic capacitance contrast in non-contact imaging modes, depends not just on the local electric permittivity of the sample, but also on its topography, *h(x)*, and on the tip-sample distance at which the image is acquired, z_c. As a consequence, the intrinsic capacitance does not reflect directly the electric permittivity of the materials in all situations. To illustrate it, in Figure 5-5a we plot the intrinsic non-contact capacitance contrast as a function of the imaging distance, z_c, as predicted by Equation

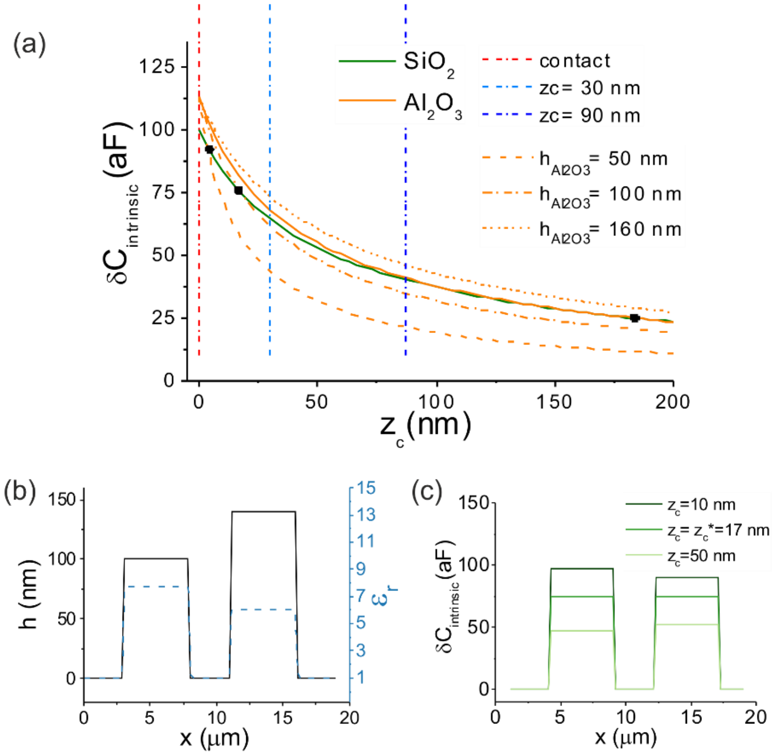

Figure 5-5

(a) Intrinsic capacitance as function of tip-sample imaging distance for a sample with thin film pillars of SiO_2 and Al_2O_3 calculated according to Equation 5-9 (tip radius R=1000 nm). The thick lines represent SiO_2 (green) and Al_2O_3 orange) pillars with properties equal to the ones determined for sample in Figure 5-2: h_{Al2O3}=130nm, $\varepsilon_{r,Al2O3}$=8 and h_{SiO2}=140nm, $\varepsilon_{r,SiO2}$=6. The thick line curves intersect at z_c*=189 nm, indicating a reverse of the contrast order for distances larger than this. At z_c=8 nm (dark blue dot-dashed vertical line) the contrasts are not reversed but they are almost indistinguishable. Instead at z_c=0 nm (red dot-dashed vertical line) and z_c=30 nm (light blue dot-dashed vertical line) the contrasts are not reversed and are ordered according to the electric permittivity of the materials. The dashed, dot-dashed and dotted orange lines represent the predictions of Equation 5-9 for the case of different heights of the Al_2O_3 pillar: h_{Al2O3}= 50 nm, 100 nm, 160 nm, respectively. The distances at which reversal occurs (if any) are marked by a black circle, and are in agreement with Equation

5-10. (b) Topographic and electric permittivity profiles of a sample used to illustrate the concept of contrast reversal (h_{Al2O3}=100nm, $\varepsilon_{r,Al2O3}$=8 and h_{SiO2}=140nm, $\varepsilon_{r,SiO2}$=6). (c) Theoretical non-contact intrinsic capacitance contrasts at three different imaging distances, z_c=10 nm, 17 nm and 50 nm, showing that contrast reversal occurs already at $z_c > z_c^*$=17 nm.

5-9 for the sample analysed in Figure 5-4 (thick green line SiO_2: h_1=140nm, ε_1=6 and thick orange line Al_2O_3: h_2=130 nm, ε_2=8). The figure shows that for imaging distances larger than z_c^*=189nm the order of the intrinsic capacitance contrast of the two pillars would become reversed in the intrinsic non-contact capacitance image (i.e. even if $\varepsilon_{r,1} < \varepsilon_{r,2}$ one would obtain $\delta C_{non-contact,\mathrm{int},1} > \delta C_{non-contact,\mathrm{int},2}$). Note, also, that at the distance of the measurement reported in Figure 5-4c, z_c=90 nm, (dot-dashed dark blue vertical line in Figure 5-5a), the two pillars show an almost identical contrast, as we have obtained experimentally (see Figure 5-4d). Instead, at z_c=30 nm (dot-dashed light blue line in Figure 5-5a) , the order of the contrasts is not reversed, also as found experimentally (see Figure 5-4b). The imaging distance at which the contrast between two regions becomes reversed depends on the relative values of their thicknesses (and on their electric permittivity values).

We show it explicitly Figure 5-5a, where we also plot the predictions of the intrinsic capacitance contrasts that would have been obtained for Al_2O_3 pillars of heights h_{Al2O3}=50 nm (orange dashed line), 100 nm (dot-dashed orange line) and 160 nm (dotted line). For the lower pillars the intrinsic contrast reversal would occur already at short imaging distances (z_c*=5 nm and 17 nm for the pillars of 50 nm and 100 nm thickness, respectively). Instead, for the taller pillar (h_{Al2O3}=160 nm) it would not occur at any imaging distance.

The meaning of the contrast reversal is illustrated in Equation 5-5b and Figure 5-5c for the case of a sample with h_{Al2O3}=100 nm. It can be shown that, in general, the contrast reversal with respect to the electric permittivity values takes place for imaging distances larger than a critical distance given by

$$z_c^* = \frac{\dfrac{h_1 h_2}{\varepsilon_{r,1}} - \dfrac{h_1 h_2}{\varepsilon_{r,2}}}{h_2 - h_1 + \dfrac{h_1}{\varepsilon_{r,1}} - \dfrac{h_2}{\varepsilon_{r,2}}}$$

Equation 5-10

In Figure 5-5a, the black circles represent precisely the values predicted by Equation 5-10.

Finally, we highlight once more that, for contact measurements, z_c=0 nm, (dot-dashed red line in Figure 5-5a) the contrast order is never reversed with respect to the corresponding electric permittivity values, as we have shown before.

We note that even if the extraction of quantitative electric permittivity images from non-contact capacitance images is less direct than for contact images, since it requires the knowledge of the sample topography and of the tip-sample distance, in addition to the tip radius, it is still possible to obtain them if required (e.g. when dealing with biological samples), as we have shown recently [64], and, also in the past, for low frequency capacitance measurements [45].

The results derived here are, in principle, valid as long as the analytical model in Equation 5-1 to Equation 5-4 remains valid. We have discussed in Ref. [40] that the thin film analytical model is valid for thin planar films showing lateral dimensions larger, and thickness smaller, than the tip radius, what cover a broad range of situations. When these conditions are not met, then the intrinsic capacitance becomes also dependent on the lateral dimensions of the thin film, and the thickness contribution still remains present in the intrinsic contact mode capacitance image. We show it

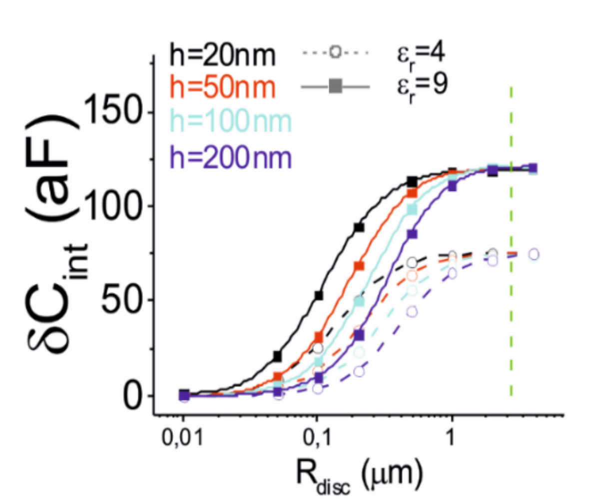

Figure 5-6 Numerically calculated intrinsic contact capacitance for dielectric discs of different thicknesses, h=20 nm, 50 nm, 100 nm and 200 nm, as a function of disc radius R_{disc} and for two different electric permittivities, ε_r=4 and 9. The tip radius is R=1000 nm and the half cone angle is θ=10°. For $R_{disc}>>R$, the intrinsic contact capacitance does not depend anymore on the disc radius, therefore it be approximated by Equation 5-1 to Equation 5-4. The vertical line represents the dimensions of the pillars in the samples analysed in Fig. 1 and 2 (equivalent R_{disc} =2820nm), which fall within the range of validity of the analytical model.

explicitly in Figure 5-6 where we plot the contact intrinsic capacitance numerically calculated (see Experimental section for details) for the case of a sample with Al_2O_3 and SiO_2 pillars of varying lateral dimensions. As it can be seen, for sample radii smaller than the tip radius (here R=1000 nm) there is a dependence of the contact intrinsic capacitance on the lateral dimensions of the thin film and on its thickness, which prevents using the simple relation in Equation 5-6. In this case, one has to resort to numerical simulations to extract and map the electric permittivity values of the sample. Instead, for larger sample diameters, the intrinsic capacitance becomes independent from the lateral dimensions of the thin film and from its thickness, and only depends on the electric permittivity (and tip radius), as shown before. In particular, the dimensions of the samples analysed here fall within this range (vertical green line), and hence can be described by the analytical model, as we did above.

To end up, we would like to stress that the problematics of disentangling topography crosstalk from electric permittivity contributions from capacitance SMM images cannot be solved by other approaches proposed to date, which involve the use of alternative imaging modes, such as constant height imaging [45], the use of special tip configurations, such as shielded probes [24, 25] and open ended coaxial probes [76], or the use of specific post-processing algorithms, such as time domain [29]. For instance, constant height imaging by definition contains no topography crosstalk effects, since the tip-substrate distance is not varied. However, in non-planar samples it provides optimal signal/noise only on the tallest parts of the sample, i.e. the closest to the tip, losing accuracy when thickness variations in the hundreds of nanometer are present in the sample. Shielded probes or open ended coaxial probes, on their side, limit the non-local interactions with the samples, i.e. the stray contributions, but not the interaction of the tip end with the substrate, which in the case of a thin film is still very relevant. Hence, their use does not eliminate topography crosstalk effects. Finally, the approach proposed by Farina et al. [29], based in analysing the SMM response in time rather than in frequency, while allowing to cancel the stray, doesn't solve the problem of the local signal changes due to the tip vertical movement, which still occurs between the tip apex and the sample. In this scope, our method represents a valid option to resolve these issues, which is even applicable with non-optimal conventional, and widely available, conductive AFM probes.

5.5 Materials and methods

5.5.1 Atomic Force Microscopy and Scanning Microwave Microscopy Imaging

The AFM-SMM setup used in this work has been described in section 2.4. Briefly, it consists of an AFM system in which a conductive tip is connected to a microwave source/meter (a vector network analyser, VNA), through a transmission line and a matching impedance, Z_0. While scanning the tip over the sample in conventional AFM imaging modes, the tip also acts as an emitting-receiving nanoantenna, irradiating a signal highly localized at the apex and at a frequency minimizing the reflections. Depending on the local impedance, part of the signal is reflected back travelling from the antenna to the VNA and recorded as a complex scattering parameter, S_{11}. This signal is converted into capacitance variation and conductance variation using a low frequency electrostatic force curve, previously acquired, following the calibration methodology described elsewhere [39]. With this system, we acquired single point approach curves, contact mode images, and intermittent contact mode images at a frequency of ~19 GHz and VNA IF bandwidth of ~500 Hz (power = 3dBm), with a resolution of 256x256 pixels. The calibration EFM force curves were acquired by applying a 3V voltage at 2 kHz frequency and recording the second harmonic amplitude 2ω. Solid platinum 25Pt400B AFM tips from Rocky Mountains Nanotechnology (nominal spring constant of ~18 N/m) were used. The noise level in the capacitance measurement is about 6aF. Note that the cross-section profiles shown from Figure 5-1 to Figure 5-4 correspond to the average obtained from 5 consecutive lines in the measured images. The tip apex radius of the tip, R, and the stray capacitance rate, k_{stray}, are determined via least square fitting of an experimental single-point approach curve on the bare metal to the theoretical model in Equation 5-1 to Equation 5-4, with h=0 nm (metal limit), as shown elsewhere [40]. The rest of the geometrical parameters is kept fixed to the nominal value: cone height H=80 μm and cone half angle θ=10°.

5.5.2 Topography crosstalk removal and intrinsic capacitance images

Intrinsic capacitance images have been obtained from the measured capacitance images by subtraction of the topography crosstalk contribution, following the procedure recently presented in chapter 3. In a nutshell, a topography crosstalk image is reconstructed by combining a single-point capacitance approach curve acquired on the metallic substrate with the topography image, and then it is subtracted from the measured capacitance image, to give rise to the intrinsic capacitance images. In order to use the same reference capacitance values in both the capacitance images and the capacitance approach curves, the latter are vertically shifted in order to set the capacitance variation at contact with the substrate to the same value obtained from the capacitance image.

5.5.3 Non-planar thin film samples fabrication

The samples consisting of SiO_2/Al_2O_3 micropatterned thin film pillars on a gold coated silicon wafer were fabricated as follows. The gold layer was deposited on a silicon wafer by thermal evaporation, using 10nm Cr as adhesion layer. After photolithography (AZ 1512 HS positive photoresist, Microchemicals) and development of the exposed resist (AZ 726 MIF developer, Microchemicals), about 65 nm (sample 1) and 140 nm (sample 2) of SiO_2 (Umicore) were deposited by e-beam evaporation. Subsequently, a lift-off process was performed in order to obtain the corresponding SiO_2 square structures on the gold coated silicon wafer. Next, a second photolithography, development, e-beam deposition and lift-of process was performed in order to deposit the 104 nm (sample 1) and 130 nm (sample 2) layer of Al_2O_3 (Umicore), and micropattern them at about 5 microns apart from the SiO_2 structures already present on the gold coated silicon wafer. Micropatterned thermal grown SiO_2 samples on highly doped silicon wafers have been produced by AMO GmbH.

5.5.4 Numerical simulations

To determine the effects of the lateral dimensions of the micropatterned oxides on the intrinsic capacitance values, we used a 2D axisymmetric model described in section 4.4.2 We calculate the tip-sample capacitance by integration of the surface charge density on the tip. Since the sample is located within the near-field region of the probe, the microwave field distribution is found in a static approximation, i.e. by solving Poisson's equation. In the geometrical model, the tip is represented by a truncated come ending with a hemisphere. Since, the intrinsic capacitance image does not contain any stray contribution, it is possible to omit the geometrical parts representing the cantilever and other microscopic components responsible of long range interactions.

5.6 Conclusions

We presented a method that enables mapping the GHz electric permittivity properties of non-planar thin film heterogeneous samples from AFM-SMM capacitance images acquired in contact mode. We showed that by constructing an intrinsic capacitance gradient image, in which topography crosstalk contributions are subtracted, one can derive directly a local electric permittivity image of the sample with just knowledge of the tip radius, and no effect of the material thickness. In addition, we have shown that for samples containing a reference material with known electric permittivity properties, the derivation of the quantitative electric permittivity map can be obtained even without knowing any information regarding the tip geometry. In the derivation of these results, it is key the use of contact mode imaging. In the case of non-contact imaging modes (such as intermittent contact mode, constant height or two pass modes very often used in SMM measurements) the interpretation of the intrinsic capacitance images in terms of the materials electric permittivity is not direct, since they are still affected by the thickness of the sample. Present findings represent a crucial step towards a quick and straightforward quantification of the electric microwave properties of 3D heterogeneous samples, and we believe that they can facilitate the way to the still rather unexplored field of microwave electrical characterization of three-dimensional structures.

6. NANOSCALE ELECTRIC PERMITTIVITY OF SINGLE BACTERIAL CELLS

The study of the tall inorganic heterogeneous pillars in chapter 5 provided an insight about the quantitative potential and limitations of the SMM capacitance images, once topography crosstalk is removed. In particular, we have seen that for intrinsic capacitance images acquired in non-contact mode, the contrast depends on the topography of the sample and on the distance tip-sample at which the image has been acquired.

Taking this into account, I finally analysed the dielectric local response of a single cell, namely an E.coli bacterium. I acquired the capacitance image at ~19 GHz, in intermittent contact mode, in dry and ambient conditions, and removed the topography crosstalk with the procedure detailed in chapter 3. By combination of this images with the 3D numerical models developed by Dr. Fabregas, and the analytical tools described in the 4th chapter, it was possible to extract the local permittivity of the cell.

This chapter reproduces almost literally the manuscript "Nanoscale electric permittivity of single bacterial cells at GHz frequencies by Scanning Microwave Microscopy, by M. C. Biagi,, R. Fabregas, G. Gramse, M. Van Der Hofstadt, A. Juárez, F. Kienberger, L. Fumagalli, and G. Gomila. In this manuscript I was in charge of performing the integration of experimental and theoretical part and of analysing the results. The manuscript was written by me in collaboration with the other authors.

6.1 Abstract

We quantified the electric permittivity of single bacterial cells at microwave frequencies and nanoscale spatial resolution by means of near-field Scanning Microwave Microscopy (SMM). To this end, calibrated complex admittance images have been obtained at ~19 GHz and analysed with a novel methodology that removes the non-local topography crosstalk contributions and thus provides quantifiable intrinsic dielectric images of the bacterial cells. Results for single Escherichia coli cells provide a relative electric permittivity of ~4 in dry conditions, and ~20 in humid conditions, with no significant loss contributions. Present findings, together with the ability of microwaves to penetrate the cell membrane, open an important avenue in the microwave label-free imaging of single cells with nanoscale spatial resolution.

6.2 Introduction

The electromagnetic properties (specifically, the complex permittivity) of single cells in the GHz frequency range are of utmost interest for biological and medical applications of microwaves. In particular, they determine how microwaves are transmitted, reflected or absorbed by biological tissues. This information can give rise to important novel microwave medical applications, such as medical microwave imaging [77] or microwave hyperthermia treatment for cancer and other diseases [78-81]. Electromagnetic properties are also relevant to assess the potential hazardous effects of microwaves on biological samples [82].

Until now, the information on the complex permittivity of cells has been obtained from macroscale studies carried out on tissues and cell suspensions [13], and from whole cell studies carried out with integrated microelectrodes in microfluidic devices [8, 83]. At present, however, there is a lack of information at the sub-cellular level and from small size cells, such as microorganisms, due to the inherent limitations of the existing techniques to address the very small scales (nanoscale).

In recent years, the Scanning Microwave Microscope has appeared as a potential alternative to access the electromagnetic properties of samples with high spatial resolution. Scanning Microwave Microscopy (SMM) [15, 25, 84] is a scanning probe technique that measures the local reflection of microwaves from the sample under inspection by means of a sharp probe, brought in close proximity to the sample surface (within the near-field region). SMM measurements can be related to the electrical impedance of the samples and this, further on, to their local complex permittivity. Due to the combination of the good lateral resolution of near-field measurements (far below the wavelength of the source radiation) with the high penetration depth of the microwaves, SMM represents a unique technology to produce high spatial resolution maps of the surface and internal electromagnetic properties of materials [15, 25, 84-86]. Since the original proposal by Ash and Nicholls [21] SMM has evolved incorporating advanced tip designs, better control of the tip sample distance and accurate quantification procedures, which now enable the extraction of the local complex permittivity with a spatial resolution deep down the sub-micrometre range in some specific applications (e.g. thin dielectric films) [63, 87-89]. SMM has also been applied to the local doping profiling of semiconductors [84]. Other relevant applications involve the study of highly correlated systems, such as complex oxides [56], graphene [57, 58], carbon nanotubes [59] and superconductors [90].

In contrast with its wide use in inorganic samples, SMM has been scarcely applied to biological systems[26, 30,31, 91]. In fact, compared to solid state inorganic samples, the measurement of biological samples presents a number of additional difficulties, such as their soft nature, the need to work under physiological liquid conditions for living cells studies, and their highly non-planar and irregular shape. These characteristics challenge the quantification of the local electromagnetic properties. The development of Atomic Force Microscopy (AFM)-based SMM systems, combining intermittent contact topographic imaging with microwave imaging , and the possibility to obtain images in liquid medium [28, 92] have enabled to solve some of these challenges. However, due to their highly non-planar structure, the quantitative determination of the complex permittivity of single cells with SMM still remains an open issue due to the overwhelming relevance of topography crosstalk contributions.

Here, we precisely consider this problem by presenting a methodology to analyse and remove crosstalk contributions from SMM images in a quantitative fashion, and so to access the intrinsic local electromagnetic response of non-planar bio-samples with nanoscale spatial resolution. The proposed methodology has been validated by means of 3D finite element numerical calculations and has been successfully applied to the analysis of single E. coli bacterial cells, providing the first evaluation of the nanoscale electric permittivity of a single cell in the GHz frequency range.

6.3 Results and discussion

SMM complex admittance images of non-planar bio-samples, like single bacterial cells, obtained in the conventional imaging modes (contact, intermittent contact or lift-mode) present always a large topography crosstalk contribution, which stems from the changes in probe-substrate capacitance due to the vertical movement of the probe when tracing the sample topography. This contribution usually masks the local dielectric response of the sample and makes very difficult to obtain quantitative electric permittivity values directly from SMM complex admittance images.

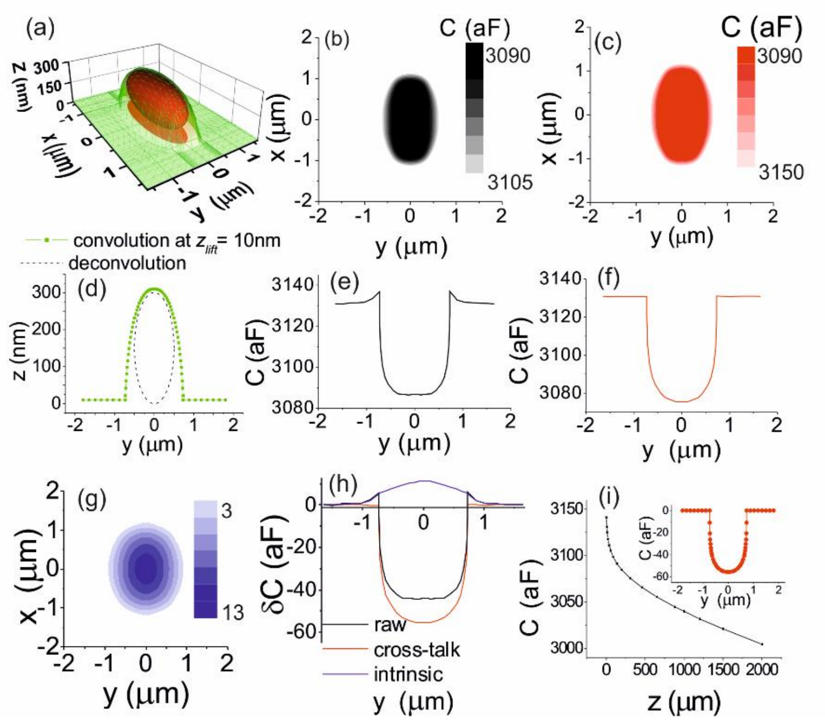

Figure 6-1 a) Green surface: ensemble of simulated lines representing the 3D tip movement over the bacterial cell (convoluted topography represented by a superellipse with n=2.3) and (b) numerically calculated capacitance image; (d) and (e) represent the corresponding transversal cross-section profiles. Dimensions of the bacterial cell: w=1000 nm, l= 2000 nm, h = 300 nm; dielectric constant of the bacterial cell ε_r = 4; tip radius R = 250 nm and tip-sample distance z_{lift} = 10 nm. (c) Topography crosstalk image obtained as in (b) but setting ε_r=1, and (f) corresponding transversal cross-section profile. (g) Intrinsic capacitance image obtained from the subtraction of (c) and (b). (h) Corresponding intrinsic transversal cross-section profile (blue line), total capacitance contrast (black line, same as in (e)) and topography crosstalk contrast (red line same as in (f)), the two latter referenced to the substrate value. . (i) Calculated capacitance approach curve on the bare metallic substrate. Inset: (circles) reconstructed topography crosstalk profile obtained combining the capacitance approach curve and the sample topography; (line) topography crosstalk profile same as in (e).

In order to illustrate the relevance of this contribution, and to design a method to remove it in a quantitative way, we have calculated theoretical SMM capacitance images of a tip-bacterial cell model with the help of 3D finite element numerical calculations, as detailed in the Material and Methods section. The tip-bacterial cell model takes into account specifically the geometry of the tip, represented by a truncated cone ending with a hemispherical apex, and of the bacterial cell, represented by an ellipsoid of homogeneous relative electric permittivity, ε_r. An example of a calculated electric potential 3D distribution corresponding to this model is shown in Figure 6-6, together with a 2D cross-section cut (inset Figure 6-6b).

The capacitance images are calculated by scanning virtually the tip following the convoluted sample topography at constant tip-sample distance, as in the actual acquisition of SMM images. Figure 6-1a shows the ensemble of virtual scan lines used in the calculations (green lines), together with the actual bacterial cell geometry (red ellipsoid), while in Figure 6-1d we compare a single scan line (green dots) and the corresponding cross-section bacterial cell geometry (dashed line). In Figure 6-1b we show a contour colour plot of the calculated capacitance image, and, in Figure 6-1e, a transversal cross-section profile, for a bacterial cell of relative electric permittivity $\varepsilon_r = 4$. Absolute capacitance values are shown in the images. When the tip moves up from the substrate towards the top of the bacterial cell, we observe a significant decrease in the capacitance. As it was discussed in detail in section

3.1, this capacitance decrease is mainly due to the fact that in such a displacement the tip-substrate distance increases. This fact can be explicitly seen in Figure 6-1c, where we show the capacitance image that would have been obtained in the case that the sample was not present but the tip was following the bacterial cell topography (or equivalently, in the case that the bacterial cell had $\varepsilon_r = 1$). A large decrease of the capacitance is obtained associated to the increase of the tip-substrate distance while tracing the sample topography. Clearly, this contribution is not related to the dielectric response of the sample, and just represents a topography crosstalk contribution. This contribution is indeed always present in the SMM capacitance images obtained with most conventional imaging modes (among which, contact, intermittent contact or lift modes). In order to highlight the intrinsic dielectric response of the sample, the topography crosstalk contribution has to be subtracted from the capacitance image. By performing this subtraction, one obtains an image which can be more directly related to the permittivity of the sample. We refer to it as the intrinsic capacitance image. By definition, this image shows no contrast in the case that the sample relative electric permittivity is unity, as it should be. The intrinsic capacitance image for the calculated capacitance image in Figure 6-1b is shown in Figure 6-1g, together with a transversal cross-section profile in Figure 6-1h (for easy of comparison, we also show the capacitance and crosstalk profiles, referenced to the substrate). As it can be seen, the intrinsic capacitance image shows a smaller contrast between substrate and bacterial cell than the capacitance image. Yet, it represents more truly the dielectric response of the sample, and hence, as will be shown below, it provides a better route for the local dielectric quantification. The intrinsic capacitance images obtained in this way also maximizes the SMM S/N ratio at all image points by keeping the tip always close to the sample surface. Figure 6-1h is similar to Figure 3-3b, where, the capacitance profiles were calculated with the analytical formulae for thin film rather than with 3D numerical model, such as here.

As it was explained in the 3rd chapter (section 3.2), the topography crosstalk capacitance image can also be obtained by using a capacitance approach curve and the sample topography. Indeed, if $C_{T,subs}(z)$ represents a single point approach curve onto a bare part of the substrate, with z being the tip-substrate distance, then the topography crosstalk image can be simply obtained as $C_{T,subs}\left(h'(\vec{x})+z_{lift}\right)$, where $h'(\vec{x})$ is the (convoluted) sample topography, with $\vec{x}=(x,y)$ being a plane position, and z_{lift} the tip-sample distance. This fact is illustrated in the inset of Figure 6-1i, where the cross-section profile from Figure 6-1f (line) is reconstructed from the substrate capacitance approach curve in Figure 6-1i and the sample topography in Figure 6-1a (circles).

The procedure outlined above has been applied to experimental SMM images obtained for a single E. coli bacterial cell with the experimental set-up described in the Materials and Methods section. Briefly, the set-up allows obtaining simultaneous topographic and microwave complex reflection parameter S_{11} images using a conductive probe connected to a vector network analyzer scanned over the sample surface. The S_{11} images are then

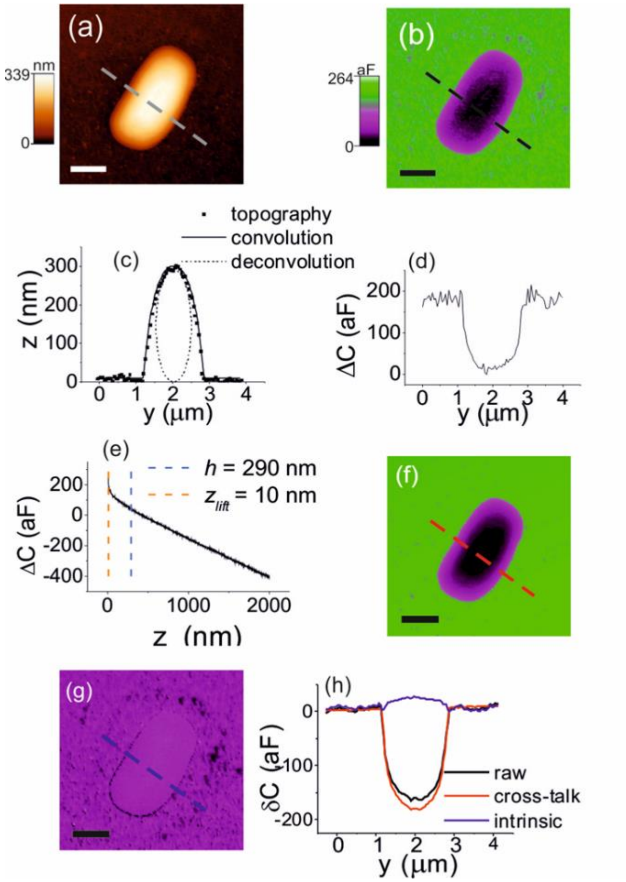

Figure 6-2. (a) Topography and (b) calibrated capacitance images of an E. coli bacterial cell at ~19 GHz in dry conditions (RH≤5%). (c) and (d) represent the corresponding transversal cross-section profiles along the dashed lines in the images. In (c) the actual bacterial cell cross-section extracted from deconvolution of the measured topography is shown as a dotted line. (e) Measured capacitance approach curve on the bare metallic substrate. The curve has been shifted by ~287 aF to level it with the substrate value in the capacitance image, at the lift distance z_{lift}=10 nm. The part of the curve used in the reconstruction is shown between the vertical dashed lines. (f) Reconstructed topographic cross-talk capacitance and (g) intrinsic capacitance images. (h) Comparison of transversal cross-sectional profiles referenced to the substrate along the dashed lines in the images. Scale bar 1μm

converted into calibrated complex admittance images, represented as conductance and capacitance images, which are then subject to analysis and quantification. Figure 6-2 shows simultaneously acquired (a) topography and (b) calibrated capacitance images on a single bacterial cell obtained at ~19 GHz in dry conditions (RH≤5%). The corresponding transversal cross-section profiles are shown in Figure 6-2c and Figure 6-2d. The conductance image shows negligible contrast, and it is not further considered (see section 6.6.4). Note that capacitance variations and not absolute values, are shown in the figure. The deconvoluted dimensions of the bacterial cell obtained from the topographic image (Figure 6-2a) are w= 963 nm, l= 2350 nm, h= 290 nm (see section 6.6.3). These dimensions are in agreement with those previously obtained for dry E. coli bacterial cells [41].

The capacitance image (Figure 6-2b) shows a clear decrease of the signal when the tip is on top of the bacterial cell, similarly to what was observed in the numerical calculations. As we have discussed before, this decrease is mainly due to the topography crosstalk, and this can be clearly seen in Figure 6-2f, where the crosstalk capacitance image corresponding to this bacterial cell is shown. This image has been obtained with the help of a capacitance approach curve measured on a bare part of the substrate (Figure 6-2f) and the sample topography (Figure 6-2a), as described above. The tip sample distance (z_{lift}= 10 nm) has been taken to be the tip oscillation amplitude used in the intermittent contact imaging. Figure 6-2g shows the intrinsic capacitance image obtained by subtraction of Figure 6-2b from Figure 6-2f.

The intrinsic capacitance image shows a much smaller contrast between substrate and bacterial cell than the capacitance image itself, right because of the lack of topography crosstalk contribution. For instance, in Figure 6-2h we show a comparison of transversal cross-section profiles of the capacitance (black line), topography crosstalk (red line) and intrinsic capacitance (blue line), taken along the dashed lines in the respective images and referenced to the substrate. One can see that the maximum capacitance contrast is ~160 aF, while the maximum intrinsic capacitance contrast only amounts to ~27 aF, i.e. ~17% of the former.

The benefit of this type of analysis is even more evident when comparing the results of Figure 6-2 obtained under dry conditions, with those obtained under humid conditions for the same bacterial cell and for similar imaging settings (Figure 6-3). Figure 6-3a shows the bacteria topography, Figure 6-3b the calibrated capacitance image, Figure 6-3c the topography crosstalk image, reconstructed from the capacitance approach curve in Figure 6-3e and the sample topography, Figure 6-3d the intrinsic capacitance image, and Figure 6-3f a comparison of transversal cross-section profiles taken along the dashed lines shown, referenced to the value on the substrate. The corresponding topography profile is shown in the inset of Figure 6-3e with the de-convoluted bacteria dimensions. In this case, the maximum capacitance contrast obtained is nearly ~80 aF while the maximum intrinsic capacitance contrast is around ~40 aF, i.e. around a 50%. This value compared with a relative contribution of ~17% for the measurements in dry

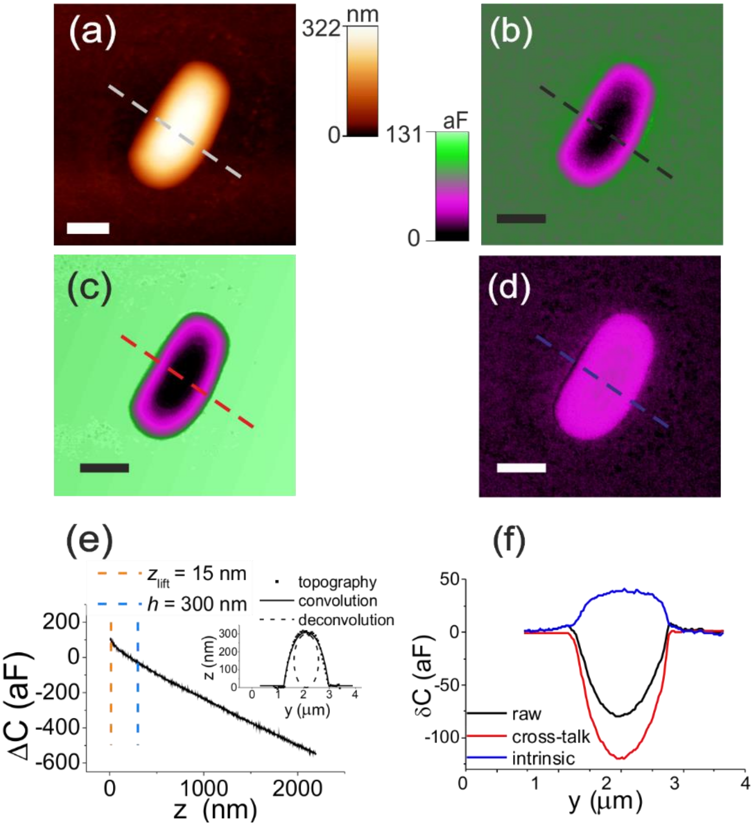

Figure 6-3. (a) Topography, (b) calibrated capacitance, (c) reconstructed topographic crosstalk and (d) intrinsic capacitance images for the same bacterial cell in Figure 6-2, but in humid conditions (RH=40%). (e) Capacitance approach curve on the metallic substrate used to reconstruct the topography crosstalk capacitance image (the curve has been shifted +359aF in order to level it with the substrate capacitance value in the image at the lift distance (in this case zlift=15nm). Inset: topographic cross-section profile along the line in (a). Dashed lines represent the deconvoluted bacterial cell geometry. (f) Comparison of transversal cross-section profiles referenced to the substrate along the dashed lines in (b), (c) and (d). Scale bar 1µm.

conditions, clearly points out that under humid conditions a larger dielectric response is obtained, and hence, that the sample should have a larger effective relative electric permittivity.

This statement can be quantitatively supported by comparing the obtained intrinsic capacitance images to the ones numerically calculated for the tip-bacterial cell model (Figure 6-6a), with the relative electric permittivity of the bacterial cell being the single adjustable parameter. In the calculations, we use the actual

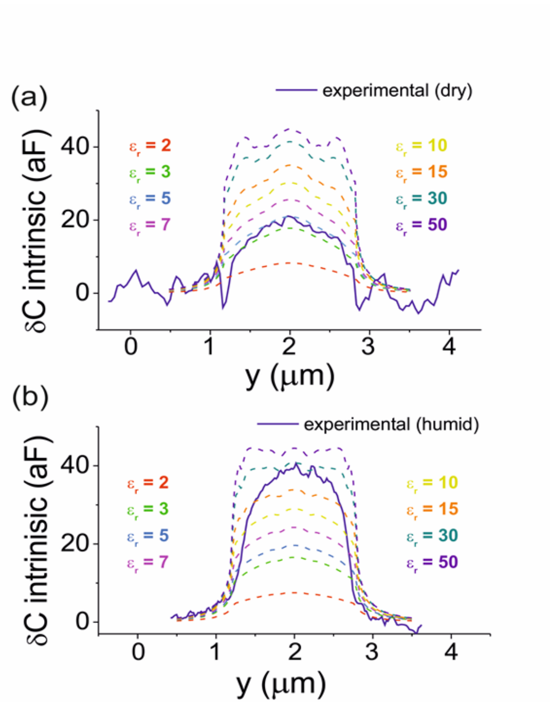

Figure 6-4 (a) Comparison of numerically calculated intrinsic capacitance profiles for different dielectric constants of the bacterial cell in Figure 6-2 (dashed lines) with experimental intrinsic capacitance profile (continuous thick line). The best agreement is found for ε_r~3-5. Data: w = 963 nm, l = 2350 nm, h = 290nm, R = 446nm, θ=10º, z_{lift} = 10nm. (b) Idem for the case of the bacterial cell in Figure 6-3, i.e. in humid conditions. The best agreement is found for ε_r ~15-30. Data: w = 950 nm, l = 2350 nm, h = 300 nm, R = 564nm, θ= 10º, z_{lift} = 15 nm. The experimental profiles in the image are the average of 4 consecutive lines for better signal to noise ratio.

measured dimensions of the bacterial cell, resulting from the topographic image and tip deconvolution procedure, the calibrated tip radius, obtained from the tip geometry calibration process, and the actual tip sample distance (z_{lift}), set to the mechanical oscillation amplitude of the probe.

In Figure 6-4a we show calculated intrinsic capacitance transversal cross-section profiles for different values of the bacteria relative electric permittivity (dashed lines), and compare them with the experimentally measured one in dry conditions (blue thick line, same as in Figure 6-2h). The experimental profile matches the theoretical ones for $\varepsilon_r \sim 3\text{-}5$. Similarly, in Figure 6-4b we show the same for the measurements performed in humid conditions. In this case, the best agreement is obtained for $\varepsilon_r \sim 15\text{-}30$, a considerable larger value than that obtained for dry conditions. These results then confirm in a quantitative way, what anticipated directly from the analysis of the intrinsic capacitance images, i.e. that in humid conditions a much larger dielectric response of the sample is obtained. Noteworthy, the relative permittivity values obtained from the analysis of the intrinsic capacitance images are in full agreement with those obtained from single point approach curve measurements performed on the center of bacteria, showing the full quantitative capability of the image quantification method presented here (see section 6.6.5, and 4.5.2, for more details on quantitative dielectric measurements with the approach curve method).

Present results constitute the first quantification of the local electric permittivity of a single bacterial cell in the GHz frequency range, obtained from SMM images. Up to now only low frequency measurements in the kHz range had been reported, obtained with a different scanning probe microscopy technique: electrostatic force microscopy [41]. In comparison, SMM measurements offer a major potential for nanoscale label-free imaging purposes, especially due to the higher penetration depth of microwaves with respect to low frequency signals. Microwave then could be more sensitive to the cells' interior properties, a characteristic that is expected to show its full potential for measurements performed under physiological conditions, whose quantitative analysis is still under development.

The origin of the different permittivity values measured in dry and humid conditions can be, in principle, attributed to the presence of moisture in the bacterial cell wall in the case of humid environment measurements. Indeed, at 19 GHz the relative electric permittivity of water is still around ~40 [93, 94], a value considerably higher than that of bacterial components. A similar explanation was provided for the low frequency measurements (~kHz) reported in Ref. [41] that showed a similar trend. More intriguing is the fact that no significant loss effects associated to the presence of moisture have been experimentally observed (the conductance images showed practically no contrast, with only a minor difference between humid and dry environment measurements, see section 6.6.4). This fact occurs in spite of the fact that loss effects in bulk water are maximal at around ~20 GHz [93, 94], very close to the measuring frequency. The reason why this happens is still under investigation, and could be related to the sensitivity of

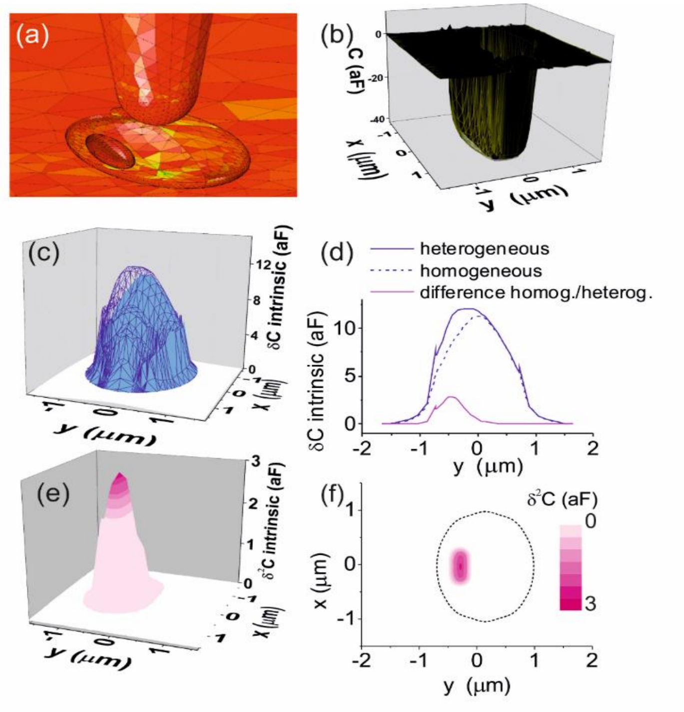

Figure 6-5 3D representation of a tip-bacterial cell model, with the bacteria presenting an internal inclusion. Dimensions of the bacterial cell: $w = 1$ μm, $l = 2$ μm, $h = 300$ nm and of the inclusion $w' = 200$ nm, $l' = 800$ nm, $h' = 150$ nm. Dielectric constant of the bacterial cell $\varepsilon_r = 4$ and of the inclusion $\varepsilon_r = 1000$. Tip radius: $R = 250$ nm. (b) Calculated capacitance image (black surface) for the heterogeneous bacterial cell and comparison with the homogeneous one (same as in Figure 6-1b, yellowish contour lines). In the calculations the tip follows the convoluted paths in Figure 6-1a. (c) Intrinsic capacitance image of the heterogeneous bacterial cell (blue surface lines) compared to the one of the homogeneous bacterial cell (same as in Figure 6-1g, cyan surface). (d) Transversal cross-section profiles of the intrinsic capacitance images for the heterogeneous and homogeneous bacteria. Also shown, the subtraction of the two intrinsic capacitance profiles (pink line). (e) 3D representation of the subtraction of the intrinsic capacitance images corresponding to the homogeneous and heterogeneous bacteria. (f) 2D contour plot of (e), with the actual bacterial cell geometry shown as dashed lines.

the conductance channel to loss phenomena in complex samples like a bacterial cell, or to a different behavior of moisture in a bacterial cell wall with respect to bulk water.

Moreover, we would like to emphasize the fundamental advantage of the methodology presented here for SMM image analysis, with respect to methodologies based on single point spectroscopic measurements (see section 6.6.5). The image analysis method proposed allows to visualize and quantify in a single shot the dielectric homogeneity (or heterogeneity) of the whole sample at very high spatial resolution. For instance, from Figure 6-2g and Figure 6-3d, one can directly infer that the bacterial cell shows an approximately homogeneous dielectric response, which is in fact in agreement with the lack of internal structure presented by these cells. Achieving the same information from single point measurements would require the acquisition and analysis of a large number of curves at different positions in the sample. This would complicate largely the analysis and would compromise severely the achievable spatial resolution.

Finally, we would like to highlight the potential of the image analysis method proposed here for the label-free imaging of sub-cellular structures. To illustrate this point we consider the case of a bacterial cell with a dielectric inclusion, not detectable from the cell topography (Figure 6-5a). In this example the bacterial cell has the same geometry and permittivity than that of Figure 6-1but it presents an inclusion with ε_I=1000. In Figure 6-5b we show the calculated capacitance images for this bacterial cell, and for an uniform bacterial cell, both obtained scanning at a lift distance

z_{lift}=10 nm with a tip of radius $R = 250$ nm. As it can be seen, a relatively tiny difference is observed between both calculated images, namely a small sinking, which would be very difficult to appreciate experimentally. Instead, when the intrinsic capacitance images are compared (Figure 6-5c), a distinct relative difference between the homogeneous and heterogeneous cases can be detected and the presence of some internal structure is more evident. This shows up even more clearly when the two intrinsic capacitance images are subtracted (Figure 6-5d, e, f): the remaining intrinsic capacitance closely resembles the internal inclusion present in the cell's interior.

6.4 Conclusions

We have shown that calibrated complex admittance images obtained in the standard Scanning Microwave Microscopy imaging modes (contact, intermittent contact or lift mode) are greatly affected by topography crosstalk contributions when taken in non-planar irregularly shaped objects like single cells. The crosstalk contribution can amount to up to an 83% of the measured image contrast in the SMM capacitance image, thus preventing the direct use of these images to quantify the samples' local electric permittivity. We have presented a methodology to quantify and remove the topography capacitance crosstalk contribution, which allows the derivation of SMM capacitance images revealing only the intrinsic dielectric response of the sample. This intrinsic contribution is then suitable for a quantitative analysis and it enables, combined with 3D finite element numerical calculations, to extract the electric permittivity of the non-planar sample. We have applied this procedure to a single bacterial cell and obtained for the first time its electric permittivity at ~19 GHz and at the nanoscale, in both dry and humid conditions. Characterizing the local electromagnetic properties of single cells in this frequency range opens important applications in Biology and Medicine. Among them, we have highlighted the potential of SMM for the label-free imaging of internal structures of single cells at an unprecedented spatial resolution.

6.5 Materials and methods

6.5.1 3D finite element simulations.

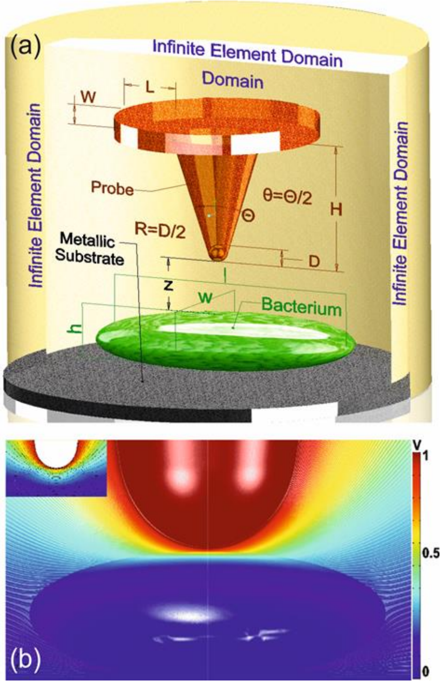

Figure 6-6 (a) Schematic representation of the 3D model of tip and bacterial cell used in the finite element numerical calculations (not to scale). (b) Example of an electric potential distribution obtained from the simulations for 1V applied on a bacterial cell with electric permittivity ε_r=4. Note that only part of the domain is shown. Inset: cross-section cut of the axial plane

We used finite element numerical simulations to calculate theoretical SMM capacitance images and theoretical SMM capacitance approach curves. These data are used in the analysis of the topography crosstalk contribution in SMM capacitance images and in the quantitative analysis of the experimental measurements.

Figure 6-6a shows the schematics of the 3D tip-bacterial cell model used. Similarly to models used in low frequency nanoscale dielectric measurements [40, 42-46], and to the 2D model presented in section 4.1.1, the tip is represented as a truncated cone of half-angle θ and cone height H terminating in a tangent hemisphere of radius R. A disc of thickness W and with a radius that oversees the cone base by an amount L is located onto the cone base, and it models local cantilever effects. Non-local cantilever contributions have been taken into account through a phenomenological stray contribution term, as detailed below.

The bacterial cell is lying on a metallic substrate, and is modelled as an oblate ellipsoid with semiaxes $a=w/2$, $b=l/2$ and $c=h/2$, where w, l and h are the width, length and height of the bacterial cell. This geometry reflects the actual rod shape of bacterial cells, and represents an important evolution of the 2D axial symmetric spheroid model developed earlier [41] and detailed in section 4.4.1. An accurate process of optimization, validation and numerical noise reduction of the 3D simulations has been undertaken, in order to meet the experimental requirements and to enable the handling of 3D structures whose physical dimensions vary in more than three orders of magnitude.

The bacterial cell is assumed to have a homogeneous electric permittivity, ε_r, in agreement with the mainly capacitive response experimentally observed in both dry and humid environments. The value of ε_r must be regarded here as an effective quantity, representing the global intrinsic response of all the inner and outer bio-compartments of the bacterial cell, as explained elsewhere

[44].

The capacitance between the tip and sample was calculated solving Poisson's equation with the finite element software Comsol Multiphysics 5.0 (AC/DC electrostatic module). Poisson's equation results in the distribution of the static electric potential around the tip and in the sample (an example is depicted Figure 6-6b), from which we derive the charge density on the tip surface, and, by integration, the capacitance. Solving the Poisson's equation, instead of the full set of Maxwell's equations, implies considering the electromagnetic field in the near-field region only. This assumption is justified in the limit of tip diameter much smaller than the wavelength, and therefore legitimate in the present study [95].

In the model we set the surface of the tip to "terminal", the bottom boundary of the simulation box to "ground" and the top and side boundaries to "zero charge". The infinite element function is used on the top and side boundaries to get rid of size effects of the simulation box. The mesh was set to at least 200000 elements.

Automatic software routines have been written to compute capacitance images, $C_{tip}(\vec{x})$, where $\vec{x} = (x, y)$ represents a position in the plane of the sample. In the calculations the tip moves following the convoluted topographic profile of the bacterial cell, with the vertical tip position being given by $z(\vec{x}) = h'(\vec{x}) + z_{lift}$ where $h'(\vec{x})$ is the convoluted bacterial cell topography and z_{lift} the tip-sample distance. Images of 31x35 points have been calculated. Additionally, single point capacitance approach curves, $C_{tip}(z)$, have been calculated, where z is the tip substrate distance.

6.5.2 Scanning Microwave Microscopy imaging.

The SMM setup used in the measurements has been thoroughly discussed in section 2.4. Briefly, it consists of an Atomic Force Microscope (AFM), whose conductive tip is connected to a vector network analyzer (VNA) through a half wavelength coaxial resonator (transmission line) with a characteristic impedance of Z_0=50 Ohm. A shunt resistance of 50 Ohm is also connected in parallel to the characteristic impedance to maximize the sensitivity. The tip is scanned in intermittent contact mode (to image in gentle conditions) and traces the sample topography, while the VNA outputs a monochromatic wave at ~19 GHz. The tip acts like a nanoantenna, irradiating the microwave signal over a small sample region highly localized under its apex. Depending on the mismatch between the characteristic impedance (Z_0) and the impedance of the tip-sample system (Z) part of the wave is reflected back to the VNA, and part is transmitted throughout the sample.

The ratio between the reflected and the incident signal, known as complex reflection parameter S_{11}, is then acquired and converted into complex admittance values following a calibration procedure demonstrated elsewhere [39] and known as one port VNA calibration. Briefly, the three error parameters [96] of the transmission line in S_{11} reflection measurements are determined using as input known values of capacitance. These values results from the integration of a low frequency capacitance gradient approach curve, as taken in Electrostatic Force Microscopy (for more details see Ref. [39] and Refs. [40, 42, 43] for details on EFM curves).

In this study, images and approach curves of the complex impedance were taken using a Keysight 5600 AFM combined with a Keysight E8362B VNA. Solid platinum 25Pt400B AFM tips from Rocky Mountains Nanotechnology were used, having a nominal spring constant ~8 N/m and nominal resonance frequency ~10 kHz. Tip radii were enlarged above 100 nm to ensure adequate signal collection. SMM images were acquired in intermittent contact mode at frequency ~19 GHz and VNA IF bandwidth ~500Hz (power 3dBm). Image speed was 8μm/s and the pixel resolution 256x256. The calibration EFM force curves were recorded at the 2ω harmonic applying a voltage of 3V amplitude and 2 kHz frequency. Complex admittance data are presented as conductance (G) and capacitance (C) images, which are obtained from the real and imaginary parts of the admittance images, $= G + j\omega C$. Measurements have been performed in both humid conditions (Relative Humidity ~40-50%) and in dry conditions (RH≤5%), with the use of an environmental enclosure and the flow of Nitrogen.

6.5.3 Bacterial strain and culture conditions.

We analyzed E. coli strain MG1655 cells deposited on a gold substrate (Arrandee). A single colony from an agar plate was used to inoculate 10mL of Luria-Bertani broth and subsequently incubated overnight in a shaking water bath (250 rpm) at 37º. 600 μL of the suspension were centrifuged at 3000 rpm for 3 min, obtaining a pellet that was then resuspended in 600 μL of milli-q-water. 40 μL of this solution were pipetted onto a gold pad of

1cm×1cm and left to dry in a flow hood. The gold substrate surface had been previously washed 15 min in acetone, 15 min in isopropanol and 15 min in milli-Q water, each step in sonication, and then attached to a 1.5 cm diameter magnet through silver paint. The magnet was connected to the electric ground of the SMM. Before measuring, we rinsed the samples with milli-Q water in order to remove any salt or poorly adhered cell.

6.5.4 Tip radius calibration.

As a first step of the quantification procedure, we calibrated the tip radius of the tip, R, by applying the procedure that we previously described in the section 4.1. Briefly, experimental capacitance variation approach curves measured on the metallic substrate, $\Delta C_{exp,metal}(z) = C_{exp,metal}(z) - C_{exp,metal}(z_0)$, are acquired and matched with theoretical capacitance variation approach curves, $\Delta C_{th,metal}(z) = \Delta C_{th,metal}(z) + k_{stray}\,(z - z_0)$, calculated for different tip radii, R. Here, z_0 is a reference distance typically around 2 µm, $\Delta C_{th,metal}(z)$ is the theoretical tip capacitance variation numerically calculated (see above) and k_{stray} is a stray component representing non-local cantilever (and probe holder) effects not included in the model-see Refs. [40, 44, 46] for details on this model. The tip radius and the stray component are then extracted with the use of a specific least-square fitting routine implemented in MATLAB (Mathworks Inc.). In the fitting routine, the remaining set of geometrical parameters are set to their nominal values, namely H= 80 µm, θ=10º, W=3 µm and L=0 µm. The range of distances used in the fit is at least twice the tip radius.

For better accuracy the averaged value of the tip radius obtained from two consecutive capacitance approach curves is considered.

6.5.5 Bacterial cell geometry deconvolution.

The actual three-dimensional geometry of the bacterial cell used in the numerical calculations is obtained from the measured bacterial cell topography through the tip deconvolution procedure described in section 4.3.2, for the case that only the tip apex is tangent to the bacterial cell (Figure 4-10). The convolution is found with the formula of the superellipse. Based on the ellipsoid geometry assumed for the bacterial cell, it can be shown that the tip convoluted profile follows a superellipse function of the form

$$\left.\begin{aligned} x(\theta) &= \pm k_a \cos^{\frac{2}{n}} \theta \\ y(\theta) &= \frac{h}{2} \pm k_b \sin^{\frac{2}{n}} \theta \end{aligned}\right\} \quad 0 \le \theta \le \frac{\pi}{2}$$

Equation 6-1

where k_a and k_b are the semiaxes of the superellipse, with $k_a=w/2+R$ and $k_b=h/2+R$, where w and h are the width and height of the bacterial cell. For a longitudinal profile one has to exchange k_a by k_c where $k_c=l/2$, and l is the bacterial cell length. This approximation holds as long as the tip radius is larger than half the cell height, as is in the present study. The de-convoluted dimensions of the bacterial cell are obtained by adjusting the superellipse profile to the measured topography profile by variation of the exponent n, and semiaxis k_a (or k_c), for a given calibrated tip radius and measured bacterial cell height, h.

6.6 Appendix

6.6.1 Validation of the methodology with a SiO_2 test sample

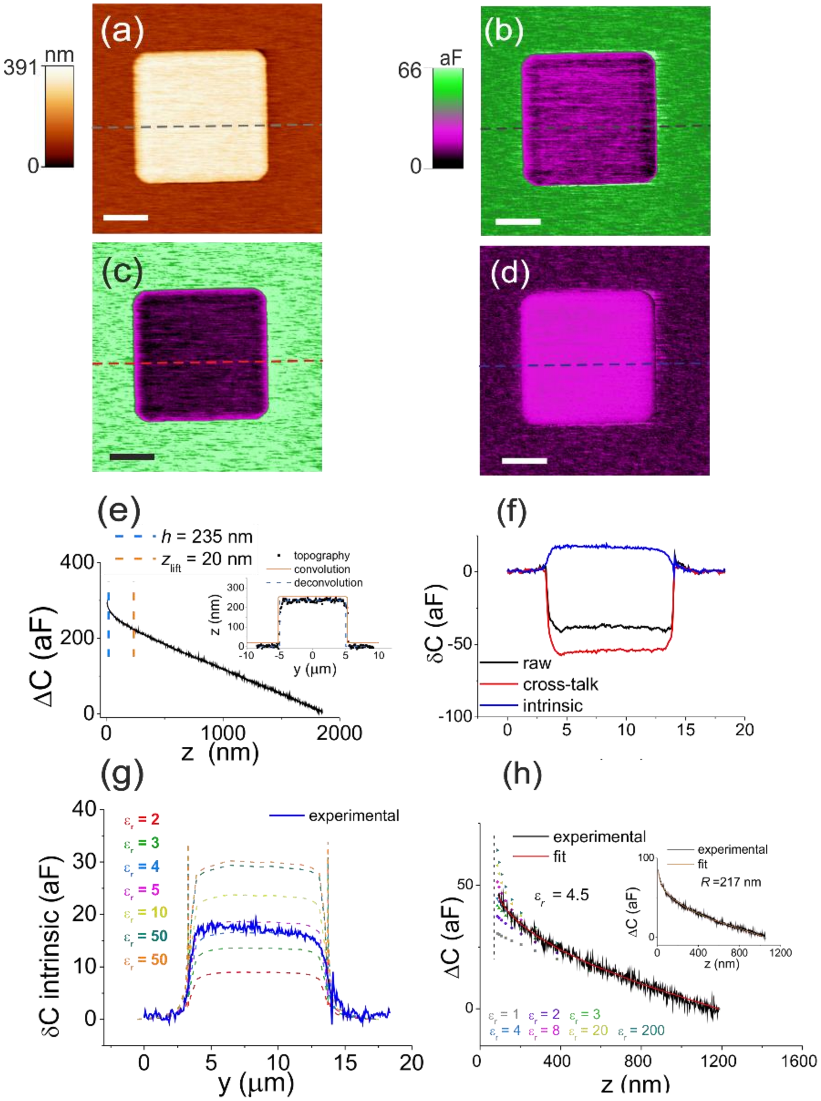

Figure 6-7

(a)-(d)Topography, total capacitance, crosstalk capacitance and intrinsic images for SiO_2 film 235nm thick and 10μm wide. Scale bar: 3.7μm. The crosstalk contribution has been calculated with the help of the capacitance approach curve on the substrate in (e) and the topographic profile along the line in (a) shown in the inset of (e). (f) Raw, crosstalk and intrinsic capacitance profiles (dashed lines) for different relative electric permittivity's of the silicon dioxide compared with the experimental profile (thick solid line). Calibrated tip radius R=217 nm, cone half angle θ=10º and lift distance z_{lift}=20nm. The comparison gives ε_r =4-5. (h) Capacitance approach curve measured on the centre of the SiO_2 (thick solid line) and comparison with theoretically calculated curves (symbols) for different values of the relative electric permittivity. The thin red line is a least square fitting of the theoretical curve to the experimental data, giving ε_r=4.5±0.5. Inset: approach curve on the bare part of the silicon substrate used to calibrate the tip geometry, with the stray contribution subtracted.

6.6.2 Bacterium geometry effects on the capacitance signal

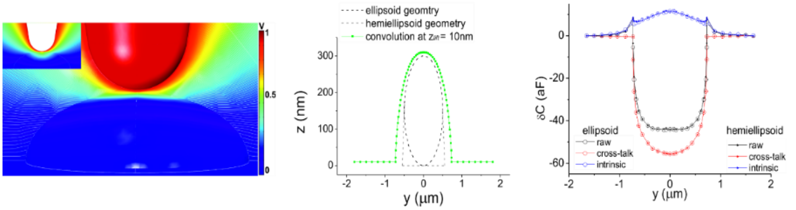

Figure 6-8

(a) Electric potential distribution for the case of a hemiellipsoidal oblate bacterium geometry. The bacterium dimensions are w=1104nm, h=300nm, l=2118nm. The hemielliposoid bacterium dimensions have been chosen so that the convoluted topographic profile is identical to the one for the full ellipsoid bacterium in (b) tip path corresponding to the convoluted hemiellipsoidal bacterium cross-section for a tip of radius R=250nm at a lift distance z_{lift} =10nm (green symbols). The grey dashed line represents the hemiellipsodal bacterium cross-section, while the dark dashed lines the full ellipsoidal bacterium in Figure 6-1. (c) Numerically calculated capacitance (black symbols), capacitance crosstalk (red symbols) and intrinsic capacitance (blue symbols) contrast profiles. For comparison, the corresponding values for the full ellipsoid geometry are represented as empty symbols. The two geometries provide almost identical results with only some small differences around the edges of the bacterium.

6.6.3 Topography deconvolution

We report here the procedure of tip deconvolution for an ellipsoid object. The tip apex is represented by a circle of radius R, and the bacterial cell by an ellipse of semiaxes alternatively $a=h/2$ and $b=w/2$ or $a=h/2$, and $c=l/2$, for the transversal and longitudinal directions, respectively, where h, w and l are the height, width and length of the bacterial cell. For given geometries of the tip and the bacterial cell, it is first found the tangent point between circle and ellipse when both lie on the same ground line (substrate). Then, the parameter n in the superellipse of Equation 6-1 is varied until this passes through three points: the centre of the circle passing through the tangent point, the centre of a circle on top of a bacterial cell, and the centre of the circle at one side of the bacterial cell. This superellipse gives the trajectory of the centre of the tip apex when a topographic image is recorded in contact with the bacterial cell. Next, the superellipse is translated downwards a distance -R. This gives the movement of the contact point between the apex and the bacterial cell while the tip is scanned at distance z_{lift} from the bacterial cell, and it is therefore a convoluted profile. The de-convoluted dimension of a topographic measurement is then obtained by varying the width (or the length) of the bacterial cell until the convoluted profile matches the profile measured from the topographic image. The height is kept fixed to the measured height, since it is not affected by the tip convolution. Figure 6-9 the application of this procedure to two bacterial cells, one measured in dry conditions (a) and one in humid conditions (b). The recovered bacterial cell dimensions obtained from the de-convolution process are listed in Table 6-1. As it can be seen, bacterial cells kept their volume quite constant (variation below 12%) when changing the atmospheric humidity conditions.

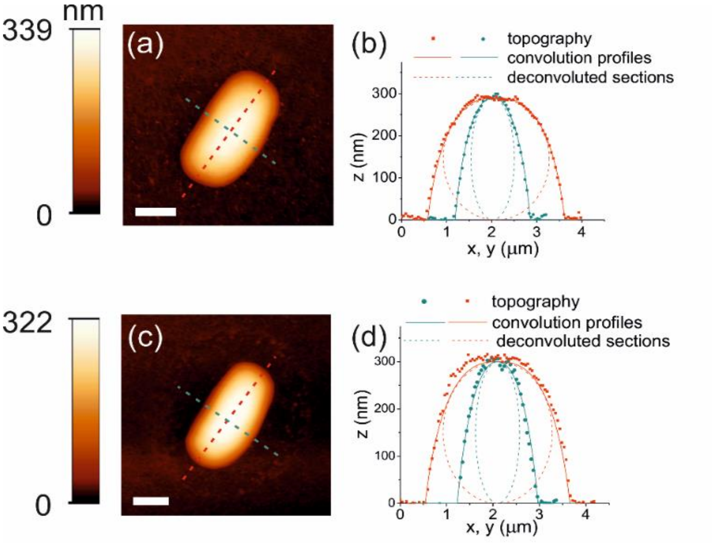

Figure 6-9

(a) Bacterial cell topographic image in dry conditions. (b) Longitudinal (red symbols) and transversal (green symbols) profiles. The continuous lines in (b) represent the fitted convoluted profile according to Equation 6-1, and the dashed line the actual bacteria geometry. Data extracted for the present cases: h = 290 nm, w = 963 nm (n_w = 2.2), l = 2350 nm (n_l = 2.63). The calibrated tip radius was R= 446 nm. (c) and (d) idem for the same bacterial cell in humid conditions. Data extracted: h=300 nm, w = 950 nm (n_w = 2.18), l = 2350 nm (n_l = 2.63). Calibrated tip radius R = 564 nm. Scale bars 1 µm.

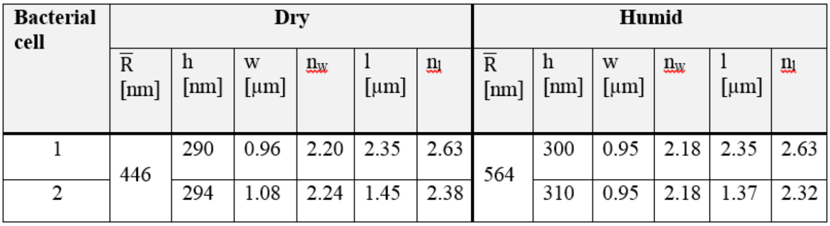

Bacterial cell	Dry						Humid					
	$\overline{R}$ [nm]	h [nm]	w [µm]	n_w	l [µm]	n_l	$\overline{R}$ [nm]	h [nm]	w [µm]	n_w	l [µm]	n_l
1	446	290	0.96	2.20	2.35	2.63	564	300	0.95	2.18	2.35	2.63
2		294	1.08	2.24	1.45	2.38		310	0.95	2.18	1.37	2.32

Table 6-1 Results of tip deconvolution for the two bacteria analyzed

6.6.4 SMM conductance images

Figure 6-10a and Figure 6-10d show the bacteria SMM conductance images recorded simultaneously to the topographic and SMM capacitance images for the case of dry and humid conditions, respectively. Figure 6-10b and Figure 6-10e show the corresponding cross-sectional profiles along the lines in the images. The SMM conductance images clearly reveal the presence of the bacterial cells. However, the origin of the image contrast cannot be associated to a conductivity or loss response of the bacterial cell. Instead, it has be associated to the fact that the tip-substrate conductance at short distances (but out of contact) decreases from the tip-substrate conductance value at larger distances, an effect that does not occur on top of the bacterial cell (see SMM conductance approach curves in Figure 6-10c and Figure 6-10f). The origin of such substrate conductance variation is still not clear, and it can be due to several factors, such as some residual from the calibration procedure, to a crosstalk associated to the vertical movement of the tip (of unknown origin for the moment) or to some physical process (still of unknown nature). A detailed interpretation of this effect lies outside the scope of the present work, as it does not influence the results reported.

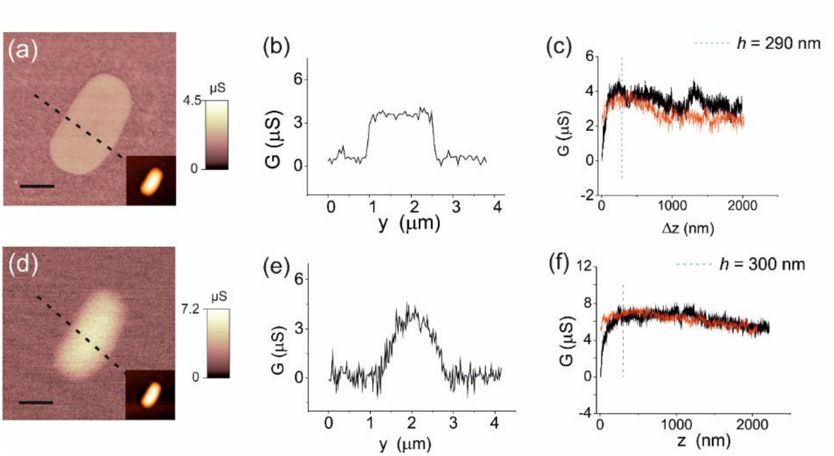

Figure 6-10 SMM conductance images obtained on single bacterial cells in (a) dry and (d) humid environments, respectively. (b) and (e) corresponding transversal cross-section profiles. (c) and (f) SMM conductance approach curves measured on the metallic substrate (black lines) and on the centre of the bacterial cell (red lines) at relative tip-sample distance, for dry and humid environments, respectively. Insets: bacterial cell topographic images recorded simultaneously

6.6.5 Relative electric permittivity quantification from single point SMM capacitance approach curves

We have also quantified the local electric permittivity of the bacterial cell from single point approach curves, taken on the same bacterial cells analysed in the paper, in dry and humid conditions. We followed a method similar to those developed for low frequency nanoscale capacitance microscopy microscopy [44-46] and electrostatic force microscopy [40, 42, 43], detailed in section 4.5.2. The sequence of measurements was the following: first, two approach curves were taken on the metallic substrate (curves 1-2 in Table 6-3). Next, three approach curves were taken at the top centre of the first bacterial cell (curves 1-2-3 for bacterial cell 1 in Table 6-2). Then, two more approaches curves where taken on the substrate (curves 3-4 in Table 6-3) and three more on top of the second bacterial cell (curves 1-2-3 for bacterial cell 2 in Table 6-2). At the end, two last curves were taken on the metallic substrate, and an image of the bacterial cell was acquired in intermittent contact mode, to verify tip and bacterial cell integrity during the measurements, and used to quantify the intrinsic capacitance.

For the radius calibration, we fitted each SMM capacitance approach curve on the metallic substrate with the theoretical capacitance approach curves obtained with from the 3D numerical calculations. The fitting parameters are R and k_{stray}, as detailed in the Materials and Methods section. Then, we set as tip radius the average of the values obtained from each couple of curves. Similarly, for the extraction of the relative electric permittivity, each of the three capacitance approach curves on the bacterial cells was fitted with theoretical capacitance approach curves obtained with the 3D numerical calculations. In this case the simulations included the apex geometry (the averaged radii) and the bacteria dimensions resulting from the tip de-convolution, with ε_r and k_{stray} being the fitting parameters. Examples of the quality of the fittings are shown in Figure 6-11. The complete list of results obtained are shown in Table 6-3 and Table 6-2.

The reproducibility of the results is illustrated in Figure 6-12 where we compare the relative electric permittivities obtained from the different measurements. According to these results the overall averaged relative electric permittivities are $\varepsilon_r = 4{,}2 \pm 0{,}6$ and $\varepsilon_r = 19{,}2 \pm 10{,}3$ in dry and humid conditions, respectively. These results are fully compatible with the ones obtained from the image analysis proposed in the main text.

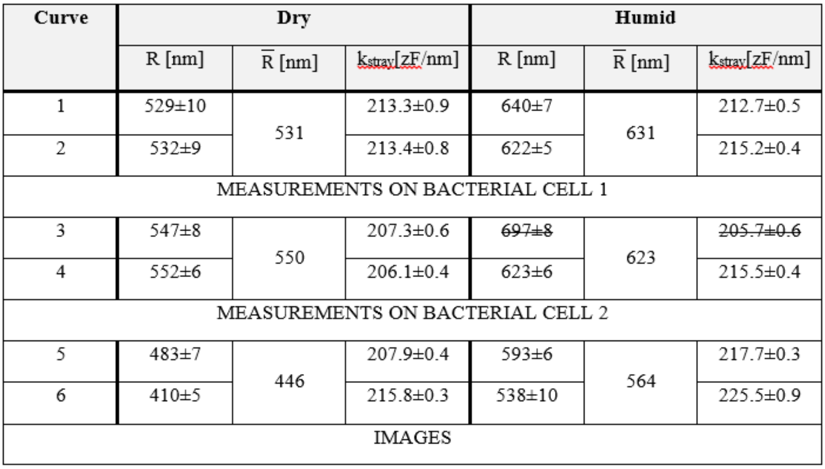

Curve	**Dry**			**Humid**		
	R [nm]	$\bar{R}$ [nm]	k_{stray}[zF/nm]	R [nm]	$\bar{R}$ [nm]	k_{stray}[zF/nm]
1	529±10	531	213.3±0.9	640±7	631	212.7±0.5
2	532±9		213.4±0.8	622±5		215.2±0.4
MEASUREMENTS ON BACTERIAL CELL 1						
3	547±8	550	207.3±0.6	~~697±8~~	623	~~205.7±0.6~~
4	552±6		206.1±0.4	623±6		215.5±0.4
MEASUREMENTS ON BACTERIAL CELL 2						
5	483±7	446	207.9±0.4	593±6	564	217.7±0.3
6	410±5		215.8±0.3	538±10		225.5±0.9
IMAGES						

Table 6-3 Results of tip radius calibration

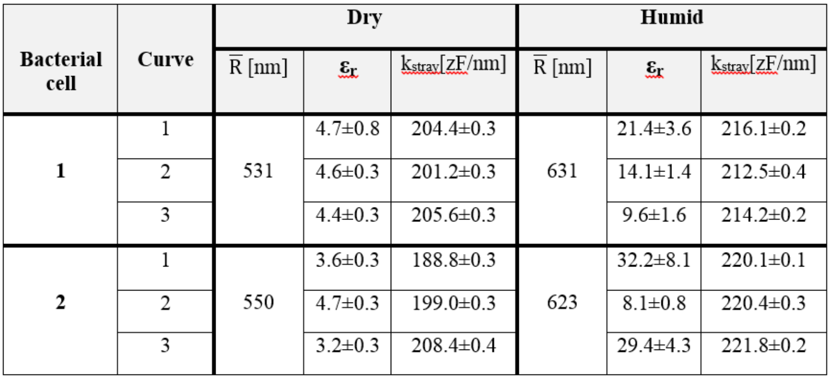

Bacterial cell	**Curve**	**Dry**			**Humid**		
		$\bar{R}$ [nm]	ε_r	k_{stray}[zF/nm]	$\bar{R}$ [nm]	ε_r	k_{stray}[zF/nm]
1	1	531	4.7±0.8	204.4±0.3	631	21.4±3.6	216.1±0.2
	2		4.6±0.3	201.2±0.3		14.1±1.4	212.5±0.4
	3		4.4±0.3	205.6±0.3		9.6±1.6	214.2±0.2
2	1	550	3.6±0.3	188.8±0.3	623	32.2±8.1	220.1±0.1
	2		4.7±0.3	199.0±0.3		8.1±0.8	220.4±0.3
	3		3.2±0.3	208.4±0.4		29.4±4.3	221.8±0.2

Table 6-2Results of tip permittivity extraction

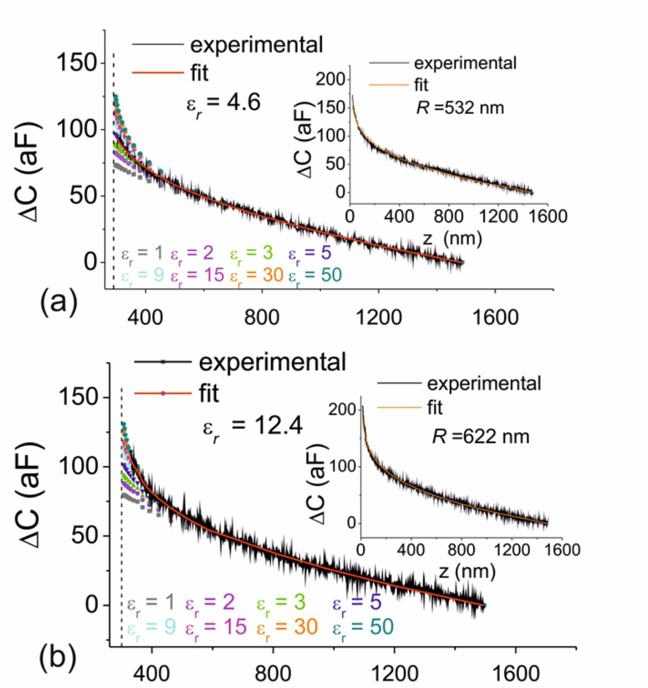

Figure 6-11 Dielectric constant extraction of a bacterial cell from SMM single point capacitance approach curves in (a) dry and (b) humid conditions. (a) Inset: Experimental (black line) and theoretical (orange line) capacitance single approach curve on the metallic substrate used for tip radius calibration, giving in this case R = 532±9 nm k_{stray}= 213.4±0.8 zF/nm. Main image: Experimental (black line) and theoretical (symbol) single capacitance approach curves on the bacterial cell. A least square fitting (red curve) gives ε_r = 4.6±0.3 and k_{stray}= 201.2±0.3 zF/nm. Parameters of the simulations: $\bar{R}$ = 531nm, cone angle θ=10º, cone height H=80 µm, cantilever width L = 0 nm, cantilever thickness W= 3 µm. Bacterial cell dimensions: w = 963 nm, l = 2350 nm, h = 290 nm. For humid bacterial cell (b), we obtain, R = 622±5nm, k_{stray} = 215.2±0.4 zF/nm for the single curve on metal, and εr = 21±4 and kstray = 216.1±0.2 zF/nm. Parameters of the simulations: $\bar{R}$ = 631nm, w = 950 nm, l = 2350 nm, h = 300 nm (remaining parameters same as in dry).

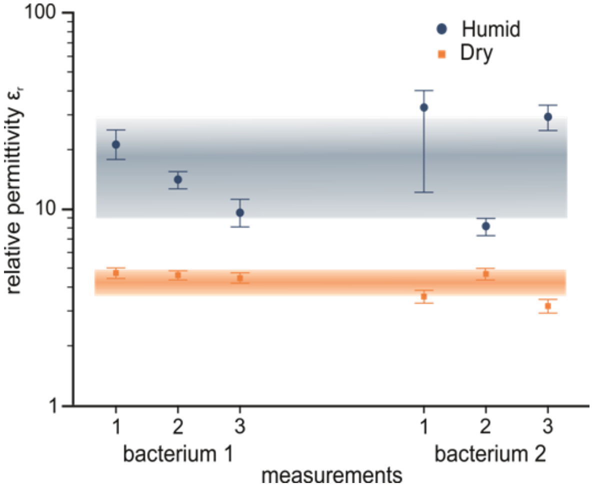

Figure 6-12 Graphical representation of three independent measurements performed in two different bacteria in dry (RH ≤ 5%) and ambient conditions (RH = 40%). The average relative electric permittivity are ε_r = 4.2±0.6 and ε_r = 19.2±10.3 in dry and humid conditions, respectively.

CONCLUSIONS AND PERSPECTIVES

The objective of my thesis was to obtain local quantitative information about the dielectric response (i.e. the permittivity) of a single cell, at microwave frequencies, by means of an AFM-based Scanning Microwave Microscope. Indeed, the final outcome of all this work is a successful application of this technique, to the quantification of the electric permittivity of a single E.coli bacterial cell, in dry and humid conditions, at ~19 GHz and at the nanoscale, as I have shown in chapter 6.

The analysis methods developed allowed to obtain for the first time a value for the nanoscale microwave dielectric permittivity of a single cell, and the technique proved to be sensitive to the environment humidity and to the constitutive molecular materials of the cell.

To attain such results I worked both on the experimental and on the theoretical aspects: in fact, the quantification of dielectric properties cannot be done but combing the experimental SMM technique to the theoretical methodologies for the interpretation of the data obtained.

In chapter 3 I have shown that the capacitance images acquired with SMM in conventional AFM modes (contact or intermittent or lift modes) are strongly affected by topography crosstalk contributions. These, especially if the sample is a tall irregular one, like a cell, hamper from drawing any even qualitative information about its dielectric nature.

I have developed a method for analysis of GHz capacitance images, which allows to remove such topography crosstalk and other non-local contributions, with a simple post-processing. Subsequently, it is possible to obtain intrinsic capacitance images, more directly related to the dielectric response of the sample. I have applied this method also to electrostatic force measurements at kHz, in a work resulting in a publication not detailed in this Thesis (which focuses on capacitance measurements ad GHz).

Interesting conclusions about the quantitative information host by the intrinsic capacitance have been drawn from the investigation of heterogeneous three-dimensional thin oxides, in chapter 5.

I have shown that the intrinsic images acquired in contact mode are utterly independent from topography, and therefore represent direct maps of the permittivity, as long as the thin film approximation is valid. Otherwise one has to resort to numerical models to quantify the permittivity.

Instead, the intrinsic capacitance contrast is not independent from the topography when the images are acquired in intermittent mode or lift mode. In such cases, it depends also on the tip-sample distance the sample's heights. Subsequently, the interpretation of intrinsic capacitance images must be done carefully in such imaging modes, which are also the most suitable for soft samples like biological cells.

In order to attain a full quantification of the permittivity, I have developed new analysis tools suitable to extract this information from intrinsic capacitance: a procedure to determine the tip dimensions (adapted from low frequency force measurements), several deconvolution algorithms to determine the actual dimensions of pillars (i.e., for parallelepiped shapes) and cells (i.e. for ellipsoidal shape), and, finally, two procedures to extract the value of the permittivity using either the intrinsic capacitance contrast or a single point approach curve acquired on top of the sample, which combine 2D numerical calculations and experimental results. As final product of the implementation these analysis tools, I developed two user friendly interfaces which were distributed within the group.

As final and main result of this work, it was possible to assay that a single E.coli is a non-planar (3D), dielectrically fairly homogeneous sample: its dielectric response was found to be uniform all over the cell volume. A value around 4 was found for the dielectric permittivity in dry conditions, in agreement with the values reported in literature for the molecular constituent of a bacterial cell. In ambient conditions it was found a permittivity of ~20, which is consistent with the presence of water in the environment.

From this standpoint, looking out in perspective, I am confident that the better understanding achieved now on how to interpret the SMM capacitance measurements, and the results of this thesis, will open the way and inspire a number of impacting studies on biological samples at the nanoscale.

Among these, I want to highlight two in particular. First, interesting results could come from studying cells presenting internal structures, naturally, such as eukaryotic cells, or by uptake, such as nanoparticles used for drug delivery. The capability of microwave to penetrate inside the cell membrane would provide images of the internal distribution at an unprecedented spatial resolution for non-labeling techniques. Secondly, the study of the local microthermal effects of microwave exposure, where the SMM system both delivers to the sample, locally, the low heating power, and records the response.

Of course, biological samples are more compelling to study in their physiological environment, but, although it is possible to perform measurements of the microwave reflection of a sample immersed in a saline solutions, the interpretation of it is much more complex. The calibration procedure presented in chapter 2, and the numerical models in chapter 4, must consider in such case the electrical effects of ion charges in a liquid medium. However, developing appropriate methodologies to obtain quantitative information from a single cell in its natural environment is surely a task to be tackled sooner or later, in order to have a proper understanding of the local microwave interaction with biological systems.

One last point to add concerns the technological advances that the results of this thesis could bring to the SMM technique. Precisely, the crosstalk removal methodology theorized and validated in this work is suitable to be implemented online in the software driving the SMM, in such a way that while SMM images are formed pixel-by-pixel from the scans over the sample, the user could see in real time the intrinsic capacitance images, already free from parasitic artifacts. Since, as it was shown in chapter 5, the intrinsic images can be (more or less straightforwardly) related to the dielectric response, this software development would save time, providing immediately a qualitative information.

RESUMEN

Caracterización eléctrica a la nanoescala de material biológico en el rango de las microondas

El objetivo de mi tesis era cuantificar la respuesta dieléctrica local de una célula individual en frecuencias dentro del rango de las microondas, utilizando un microscopio de sonda de barrido capaz de trabajar a tan altas frecuencias (scanning microwave microscope, SMM), basado en un microscopio de fuerzas atómica (AFM).

Actualmente, la mayoría de información sobre la interacción entre radiación de microondas y materia biológica ha sido proporcionada por estudios de espectroscopia dieléctrica en tejidos, suspensiones celulares o a nivel de célula individual. Estas informaciones,

obtenidas a nivel micro/macroscópico, han sido fundamentales para el desarrollo de numerosas técnicas médicas de diagnóstico y tratamiento, que utilizan la radiación de microondas como vector de energía.

Sin embargo, es necesario estudiar la interacción de campos de microondas a una escala mucho menor que la unicelular. Una de las razones, es precisamente superar la variabilidad de resultados observados con espectroscopia dieléctrica, asociada a la heterogeneidad de la materia biológica a micro y macroescala. Además, ha surgido un cierto grado de preocupación a nivel de seguridad sobre los posibles efectos dañinos de la exposición a las radiaciones de microondas que nos rodean, como pueden ser las que se utilizan para comunicación terrestre y/o vía satélite, para los radares etc. Como las patologías detectables son el resultado de cambios en los mecanismos fisiológicos que tienen lugar a un nivel de complejidad mucho más bajo (por ejemplo cambios en la distribución de cargas, en el estado químico o energético), una respuesta adecuada a este problema necesita el conocimiento del comportamiento dieléctrico a las microondas a nivel local (es decir escala nanométrica), en células individuales, componentes subcelulares y macromoléculas.

La espectroscopia dieléctrica ha alcanzado su límite de resolución, sin embargo recientemente la microscopia de rastreo con microondas en campo cercano (NF-SMM) ha aparecido como alternativa prometedora para caracterizar la respuesta dieléctrica de muestras con alta resolución espacial. Consiste en una técnica de imagen de sonda de barrido, donde la polarización dieléctrica específica es el mecanismo de contraste que forma la imagen.

En SMM, la reflexión local de las microondas por la muestra se mide por medio de una punta afilada que escanea las proximidades de la muestra, dentro de la región de campo cercano. La reflexión se relaciona con la impedancia eléctrica de la muestra, y, a partir de esta, se puede obtener la permitividad compleja local. Al medir dentro de la región de campo cercano, se asegura la excelente resolución lateral de la técnica, muy por debajo de la longitud de onda de la radiación utilizada, y principalmente relacionada con la dimensión de la sonda utilizada para el rastreo. Además, dadas las excelentes capacidades de penetración de la membrana celular que tienen las microondas, este montaje experimental, permite obtener imágenes de las propiedades dieléctricas de los componentes intra-celulares.

A pesar de la importancia, discutida anteriormente, de caracterizar la respuesta dieléctrica local en las células y componentes subcelulares a tan altas frecuencias, el SMM apenas ha sido aplicado a muestras biológicas, y los pocos estudios que existen se limitan a resultados cualitativos. De hecho, hasta ahora, no han sido reportados resultados experimentales cuantitativos acerca de las propiedades dieléctricas en el rango de las microondas y a escala nanométrica en muestras biológicas. Este hecho puede ser debido a la temprana edad de la técnica para medidas en muestras suaves en condiciones fisiológicas, es decir en líquido, y a la complejidad de la interpretación de los datos, especialmente en el caso de muestras de alturas irregulares como células.

Mi trabajo de tesis se ha enfocado precisamente en este problema:

la elaboración y aplicación de adecuadas metodologías de análisis para obtener información cuantitativa cerca la permitividad local a las microondas a nivel unicelular, a partir de medidas de SMM.

En este trabajo de Tesis he utilizado un SMM basado en un AFM, que adquiere simultáneamente imágenes de la topografía y la impedancia de la muestra. Las muestras analizadas resultaron no conductivas, por tanto, las imágenes de impedancia del SMM medidas son, de hecho, imágenes de capacidad.

En primer lugar, se demostró que una de las principales dificultades de interpretación de las imágenes SMM de capacidad en muestras con alturas irregulares, tales como las células, se encuentra en su naturaleza tridimensional, que está en el origen del “crosstalk” topográfico. El “crosstalk“ topográfico, es una contribución parásita local de la capacidad que se mide, que aparece en las imágenes adquiridas en los modos de AFM más comunes, tales como el modo de contacto, el modo de contacto intermitente o modo de elevación. Dado que a menudo representa la gran mayoría de la señal medida, puede enmascarar la respuesta dieléctrica local de la muestra.

Probablemente la contribución más importante de mi investigación tanto a la comunidad SMM como para el grupo de investigación es la elaboración de una metodología para separar y eliminar la contribución del “crosstalk” topográfico en las imágenes SMM de capacidad. El procedimiento se basa en la combinación de una curva de aproximación en capacidad, adquirida con el SMM en un punto del sustrato metálico de las muestras, que conjuntamente con la imagen de la topografía, permite de reconstruir la imagen del “crosstalk” topografico, que a continuación puede ser substraída de la imagen capacitancia adquirida con el SMM. La nueva imagen de capacitancia intrínseca obtenida en este modo está relacionada solamente con la respuesta dieléctrica intrínseca de la muestra, y por consecuencia es adecuada para la cuantificación de la permitividad.

Dado que la capacitad intrínseca es una magnitud extensiva, es decir, depende de la permitividad de la muestra pero también de su geometría y dimensiones, así como de la geometría y dimensión de las sondas, éstas deben determinarse y tenerse en cuenta cuidadosamente. La geometría de la sonda puede ser obtenida con un procedimiento de calibración, que he adaptado a las medidas de microondas a partir de uno preparado para medidas de fuerza electrostática en baja frecuencia. Este, hace uso de modelos numéricos con elementos finitos en 2D para la punta. Una vez que se conoce la geometría de la sonda, las dimensiones de las muestras se pueden recuperar de la deconvolución de la imagen topográfica con la geometría de la sonda. He elaborado varios algoritmos de deconvolución para las diferentes geometrías de las células bacterianas (elipsoide, semiellipsoide, elipsoide con tapa y elipsoidales enterrado), y de los pilares (paralelepípedo con bordes redondeados) medidos experimentalmente.

Por último, una vez que la geometría del sistema se conoce por completo, esta información se puede insertar en modelos analíticos, así como en los modelos numéricos en 2 i 3D, para calcular teóricamente la capacitad entre la punta y la muestra. Para muestras morfológicamente complejas y de dimensiones que cubren varios órdenes de magnitud, los modelos analíticos son difíciles de teorizar. De hecho, parte de mi trabajo se dedicó a adaptar los modelos numéricos 2D para una célula bacteriana y un pilar, desarrollados originalmente por el grupo de investigación para medidas en baja frecuencia, a las medidas de capacitad en microondas. La permitividad de la muestra puede cuantificarse por comparación con la capacitad calculada teóricamente con las medidas de SMM.

Como producto final de la aplicación de las técnicas de análisis y herramientas para cuantificar la permitividad, he desarrollado y distribuido dentro del grupo dos interfaces sencillas de utilizar por un usuario: una para la calibración de la punta y una otra para la extracción de la permitividad.

Antes de la aplicación a las muestras de interés, las metodologías han sido validadas en muestras de referencia, que consisten en pilares de óxido de silicio con respuesta dieléctrica conocida, y cuya altura y dimensiones son comparables a las de células bacterianas.

La primera aplicación de interés de estos métodos ha sido en muestras heterogéneas que presentan grandes variaciones de altura, y cuyas dimensiones son comparables a las de bacterias. De hecho, estas muestras, al igual que las células individuales, presentan el problema del “crosstalk” topográfico pero su naturaleza rígida e inorgánica las hace más fácil de trabajar permitiendo rebajar las precauciones experimentales que deben ser respetadas a la hora de medir muestras biológicas.

He obtenido imágenes de capacitancia intrínsecas aproximadamente a 19 GHz en muestras tridimensionales heterogéneas, que consisten en pilares de diferentes materiales y espesores, y he demostrado que cuando estas imágenes son adquiridas en modo de contacto, corresponden directamente la permitividad eléctrica del material. Esto demuestra la posibilidad de identificar directamente materiales diferentes en base a la diferente permitividad eléctrica, independientemente de sus espesores, con un simple procesamiento de la imagen. También he demostrado que los mapas cuantitativos de la permitividad eléctrica se pueden obtener de una forma sencilla, sin necesidad de ningún cálculo teórico o complejo procedimiento de cuantificación, cuando se conoce la permitividad eléctrica de uno de los materiales. El uso del modo de contacto es un factor clave a para lograr a esto resultado. Sin embargo, para la mayoría de las muestras biológicas las imágenes deben ser obtenidas en condiciones más suaves, como el contacto intermitente o modo de elevación. En tales casos he visto que los efectos del espesor de la muestra local y de la distancia de imagen hacen que la interpretación de las imágenes de capacitancia en términos de la permitividad eléctrica de los materiales sea mucho más compleja.

Finalmente, he obtenido imágenes intrínsecas, aproximadamente a ~ 19 GHz, de una sola célula, en particular una bacteria E. coli, en el modo de contacto intermitente, y en condiciones ambientales secas y húmedas. Combinando las imágenes experimentales de capacidad intrínseca con modelos numéricos 3D y las herramientas de análisis desarrolladas ha sido posible extraer la permitividad local de la célula.

E. coli ha resultado ser una muestra no plana (3D), y dieléctricamente bastante homogénea: se ha encontrado que su respuesta dieléctrica es uniforme en todo el volumen de la célula. Se ha determinado un valor de permitividad dieléctrica alrededor de 4 en seco, de acuerdo con los valores reportados en la literatura para los componentes moleculares de una célula bacteriana. En condiciones ambiente la permitividad es cerca 20, lo cual es consistente con la presencia de agua en el medio ambiente. Estos resultados representan la primera cuantificación de la permitividad local de una sola célula hecha en microondas, y demuestran que SMM es sensible a la humedad del ambiente.

En general, los resultados obtenidos demuestran que, a pesar de la complejidad del análisis de los datos, es posible cuantificar la permitividad en el rango de las microondas en muestras biológicas con resolución nanométrica, a partir de imágenes SMM de capacidad. Esta técnica experimental y la metodología de análisis asociada y desarrollada en este trabajo de tesis podrán explotar todo su potencial en las células eucariotas, cuyas estructuras internas podrían ser visualizadas gracias al poder de penetración de las microondas dentro de la membrana celular. También podrían tener una importante aplicación en el campo de las nanopartículas tanto para la administración de fármacos como para el diagnóstico, donde podrían ayudar a comprender las estructuras objetivo, su distribución, los lugares de interacción y el destino intracelular de las nanopartículas después de la administración.

.

APPENDIX

LIST OF PUBLICATIONS AND CONGRESS PRESENTATIONS

Publications

M. C. Biagi, G. Badino, G. Gramse, L. Fumagalli, G. Gomila

Direct Mapping of the Electric Permittivity at GHz frequencies of 3D heterogeneous Samples by Combined Atomic Force-Scanning Microwave Microscopy

Submitted

M. Van Der Hofstadt, R. Fabregas, **M. C. Biagi**,, L. Fumagalli, G. Gomila

Nanoscale dielectric microscopy of non-planar samples by lift mode electrostatic force microscopy

Nanotechnology (2016), **27**, 405706

M. C. Biagi, R. Fabregas, G. Gramse, M. Van Der Hofstadt, F. Kienberger, L. Fumagalli, G. Gomila

Nanoscale Electric Permittivity of Single Bacterial Cells at GHz frequency by Scanning Microwave Microscopy

ACS Nano (2016), **10**, 280−288

Congress presentations

M. C. Biagi, R. Fabregas, G. Badino, F. Kienberger, L. Fumagalli, G. Gomila

Mapping the nanoscale dielectric permittivity on heterogeneous samples via Scanning Microwave Microscopy (poster)

8th Ibec Symposium, Barcelona, 2016

M. C. Biagi, R. Fabregas, G. Gramse, M. Van Der Hofstadt, F. Kienberger, L. Fumagalli, G. Gomila
Nanoscale Electric Permittivity of Single Bacterial Cells at GHz frequency by Scanning Microwave Microscopy
(oral presentation)
6th AFM Multifrequency, Madrid, 2016

M. C. Biagi, R. Fabregas, G. Gramse, M. Van Der Hofstadt, F. Kienberger, L. Fumagalli, G. Gomila
Nanoscale Electric Permittivity of Single Bacterial Cells at GHz frequency by Scanning Microwave Microscopy (poster)
Nanobiomed, Barcelona, 2015

M. C. Biagi, R. Fabregas, G. Gramse, M. Van Der Hofstadt, F. Kienberger, L. Fumagalli, G. Gomila
Nanoscale dielectric characterization of single bacterial cells at microwave frequency (oral presentation)
Ibec PhD seminars, Barcelona, 2015

M. C. Biagi, R. Fabregas, G. Gramse, M. Van Der Hofstadt, F. Kienberger, L. Fumagalli, G. Gomila
Nanoscale Electric Permittivity of Single Bacterial Cells at GHz frequency by Scanning Microwave Microscopy
(oral presentation and poster)
7th Ibec Symposium, Barcelona, 2015

R. Fabregas, **M. C. Biagi**, L. Fumagalli, G. Gomila
Three-Dimensional Modeling of Scanning Microwave Microscopy Applied to a Single Bacterial Cell (poster)
Iberian Comsol Multiphysics Conference, Malaga, 2015

M. C. Biagi, R. Fabregas, G. Gramse, M. Van Der Hofstadt, F. Kienberger, L. Fumagalli, G. Gomila
E.Coli polarization at microwave: a quantitative analysis (poster)
Nanomeasure, Barcelona, 2015

M. C. Biagi, L. Fumagalli, G. Gomila
Nanoscale electrical characterization of biological samples at microwave frequencies (poster)
6th Ibec Symposium, Barcelona, 2014

REFERENCES

[1] R. Sorrentino and G. Bianchi, *Microwave and RF Engineering*, John Wiley and Sons, 2010.

[2] T. S. England, “Dielectric properties of the human body for wave-lengths in the 1-10 cm range,” 1950, *Nature*, **166**, 480–481.

[3] T. S. England and N. A. Sharples, “Dielectric Properties of the Human Body in the Microwave Region of the Spectrum,” *Nature*, 1949, **163,** 487–488.

[4] H. F. Cook, “The dielectric behaviour of some types of human tissues at microwave frequencies,”1951, *Br. J. Appl. Phys.*, **2**(10), 295–300.

[5] H. P. Schwan, “Electrical properties of tissues and cell suspensions: mechanisms and models,”1994, *Proc. 16th Annu. Int. Conf. IEEE Eng. Med. Biol. Soc.*, 70–71.

[6] T. Chen, D. Dubuc, M. Poupot, J.-J. Fournié, and K. Grenier,

"Microwave biosensor dedicated to the dielectric spectroscopy of a single alive biological cell in its culture medium," 2013, *Proc. IEEE Int. Microw. Symp*, 1–4.

[7] Y. Yang, H. Zhang, J. Zhu, G. Wang, T.-R. Tzeng, X. Xuan, K. Huang, and P. Wang, "Distinguishing the viability of a single yeast cell with an ultra-sensitive radio frequency sensor," *Lab Chip*, 2010, **10** (5), 553–555.

[8] M. Nikolic-Jaric, S. F. Romanuik, G. A. Ferrier, G. E. Bridges, M. Butler, K. Sunley, D. J. Thomson, and M. R. Freeman, "Microwave frequency sensor for detection of biological cells in microfluidic channels," 2009, *Biomicrofluidics*, **3** (3).

[9] G. a Ferrier, S. F. Romanuik, D. J. Thomson, G. E. Bridges, and M. R. Freeman, "A microwave interferometric system for simultaneous actuation and detection of single biological cells.," *Lab Chip*, 2009, **9** (23), 3406–3412.

[10] D. van der Zwaag, N. Vanparijs, S. Wijnands, R. De Rycke, B. G. De Geest, and L. Albertazzi, "Super Resolution Imaging of Nanoparticles Cellular Uptake and Trafficking," *ACS Appl. Mater. Interfaces*, 2016, **8** (10), 6391–6399.

[11] R. Tantra and A. Knight, "Cellular uptake and intracellular fate of engineered nanoparticles: A review on the application of imaging techniques," *Nanotoxicology*, 2011, **5**(3), 381–392.

[12] F. Apollonio, M. Liberti, A. Paf, C. Merla, P. Marracino, A. Denzi, C. Marino, and G. Inzeo, "Feasibility for Microwaves Energy to Affect Biological Systems Via Nonthermal Mechanisms : A Systematic Approach," 2013, **61**(5), 2031–

2045.

[13] A. Vander Vorst, A. Rosen, and Y. Kotsuka, *RF/Microwave Interaction with Biological Tissues*, New Jersey, John Wiley and Sons, 2006.

[14] J. D. Jackson, *Classical Electrodynamics*, 3rd ed., New York: John Wiley and Sons, 1963.

[15] S. M. Anlage, V. V. Talanov, and A. R. Schwartz, "Principles of Near-Field Microwave Microscopy," in *Scanning Probe Microscopy: Electrical and Electromechanical Phenomena at the Nanoscale*, S. . Kalinin and A. Gruverman, Eds. New York: Springer Verlag, 2007.

[16] E. H. Synge, " A suggested method for extending microscopic resolution into the ultra-microscopic region," 1928, *London, Edinburgh, Dublin Philos. Mag. J. Sci.*, **6**(35), 356–362.

[17] M. Tabib-Azar, J. Katz, and S. R. LeClair, "Evanescent microwaves: a novel super-resolution noncontact nondestructive imaging technique for biological applications," *IEEE Trans. Instrum. Meas.*, 1999, **48**(6), 1111–1116, 1999.

[18] Z. Frait, "No Ti," *Czech J Phys Sect*, 1959, **A**(9), 403.

[19] R. F. Soohoo, "A Microwave Magnetic Microscope," *J. Appl. Phys.*, 1962, **33**(3), 1276.

[20] S. M. Anlage, D. E. Steinhaumer, B. J. Feenstra, C. P. Vlahacos, and F. C. Wellstood, "Near-Field Microwave Microscopy of Materials Properties," *Microwave Superconductivity, 2001,* 239–269.

[21] E. A. Ash and G. Nicholls, "Super-resolution Aperture

Scanning Microscope," *Nature*, 1972, **237**(5357), 510–512.

[22] D. E. Steinhauer, C. P. Vlahacos, F. C. Wellstood, S. M. Anlage, C. Canedy, R. Ramesh, A. Stanishevsky, and J. Melngailis, "Quantitative imaging of dielectric permittivity and tunability with a near-field scanning microwave microscope," 2000, *Rev. Sci. Instrum.*, **71**(7), 2751.

[23] V. V. Talanov, A. Scherz, and A. R. Schwartz, "Noncontact electrical metrology of Cu/low-k interconnect for semiconductor production wafers," 2006, *Appl. Phys. Lett.*, **88**(26).

[24] Y. Yang, K. Lai, Q. Tang, W. Kundhikanjana, M. a Kelly, K. Zhang, Z. Shen, and X. Li, "Batch-fabricated cantilever probes with electrical shielding for nanoscale dielectric and conductivity imaging," *J. Micromechanics Microengineering*, 2012, **22**(11), 115040.

[25] K. Lai, W. Kundhikanjana, M. a. Kelly, and Z.-X. Shen, "Nanoscale microwave microscopy using shielded cantilever probes," 2011, *Appl. Nanosci.*, **1**(1) 13–18.

[26] K. Lai, W. Kundhikanjana, H. Peng, Y. Cui, M. a Kelly, and Z. X. Shen, "Tapping mode microwave impedance microscopy," 2009, *Rev. Sci. Instrum.*, **80**(4) 43707.

[27] M. S. Kim, S. Kim, J. Kim, K. Lee, B. Friedman, J.-T. Kim, and J. Lee, "Tip–sample distance control for near-field scanning microwave microscopes," *Rev. Sci. Instrum.*, 2003, **74**(8), 3675.

[28] S. Kim, H. Yoo, K. Lee, B. Friedman, M. A. Gaspar, and R. Levicky, "Distance control for a near-field scanning

microwave microscope in liquid using a quartz tuning fork," *Appl. Phys. Lett.*, 2005, **86**(15) 153506.

[29] M. Farina, A. Lucesoli, T. Pietrangelo, A. di Donato, S. Fabiani, G. Venanzoni, D. Mencarelli, T. Rozzi, and A. Morini, "Disentangling time in a near-field approach to scanning probe microscopy," 2011, *Nanoscale*, **3**(9) 3589–93.

[30] M. Farina, A. Di Donato, T. Monti, T. Pietrangelo, T. Da Ros, A. Turco, G. Venanzoni, and A. Morini, "Tomographic effects of near-field microwave microscopy in the investigation of muscle cells interacting with multi-walled carbon nanotubes," *Appl. Phys. Lett.*, 2012, **101**(20), 203101.

[31] J. Park, S. Hyun, a Kim, T. Kim, and K. Char, "Observation of biological samples using a scanning microwave microscope.," *Ultramicroscopy*, 2005, **102**(2) 101–6.

[32] K. Lee, A. Babajanyan, H. Melikyan, C. Kim, S. Kim, J. Kim, J. H. Lee, B. Friedman, R. Levicky, and S. Kalachikov, "Label-free DNA microarray bioassays using a near-field scanning microwave microscope," *Biosens. Bioelectron.*, 2013, **42**(1), 326–331.

[33] K. Lai, M. B. Ji, N. Leindecker, M. a Kelly, and Z. X. Shen, "Atomic-force-microscope-compatible near-field scanning microwave microscope with separated excitation and sensing probes.," *Rev. Sci. Instrum.*, 2007, **78**(6), 63702.

[34] A. Tselev, J. Velmurugan, A. V. Ievlev, S. V. Kalinin, and A. Kolmakov, "Seeing through Walls at the Nanoscale: Microwave Microscopy of Enclosed Objects and Processes in Liquids," *ACS Nano*, 2016, **10**(3) 3562–3570.

[35] S.-S. Tuca, G. Badino, G. Gramse, E. Brinciotti, M. Kasper, Y. J. Oh, R. Zhu, C. Rankl, P. Hinterdorfer, and F. Kienberger, “Calibrated complex impedance of CHO cells and E. coli bacteria at GHz frequencies using scanning microwave microscopy.,” *Nanotechnology*, 2016, **27**(13), 135702.

[36] C. Gao, T. Wei, F. Duewer, Y. Lu, and X.-D. Xiang, “High spatial resolution quantitative microwave impedance microscopy by a scanning tip microwave near-field microscope,” *Appl. Phys. Lett.*, 1997, **71**(13), 1872.

[37] M. Tabib-Azar, N. S. Shoemaker, and S. Harris, “Non-destructive characterization of materials by evanescent microwaves,” *Meas. Sci. Technol.*, 193, **4** (5), 583–590.

[38] H. P. Huber, M. Moertelmaier, T. M. Wallis, C. J. Chiang, M. Hochleitner, A. Imtiaz, Y. J. Oh, K. Schilcher, M. Dieudonne, J. Smoliner, P. Hinterdorfer, S. J. Rosner, H. Tanbakuchi, P. Kabos, and F. Kienberger, “Calibrated nanoscale capacitance measurements using a scanning microwave microscope,” *Rev. Sci. Instrum.*, 2010, **81**(11), 113701.

[39] G. Gramse, M. Kasper, L. Fumagalli, G. Gomila, P. Hinterdorfer, and F. Kienberger, “Calibrated complex impedance and permittivity measurements with scanning microwave microscopy,” *Nanotechnology*, 2014, **25**(14), 145703.

[40] G. Gomila, G. Gramse, and L. Fumagalli, “Finite-size effects and analytical modeling of electrostatic force microscopy applied to dielectric films,” *Nanotechnology*, 2014, **25**(25), 255702.

[41] D. Esteban-ferrer, M. A. Edwards, L. Fumagalli, A. Jua, and G. Gomila, "Electric Polarization Properties of Single Bacteria Measured with Electrostatic Force Microscopy," 2014, *ACS Nano,* **8**(10), 9843–9849.

[42] L. Fumagalli, D. Esteban-Ferrer, A. Cuervo, J. L. Carrascosa, and G. Gomila, "Label-free identification of single dielectric nanoparticles and viruses with ultraweak polarization forces," *Nat. Mater.*, 2012, **11**(9), 808–16.

[43] G. Gramse, G. Gomila, and L. Fumagalli, "Quantifying the dielectric constant of thick insulators by electrostatic force microscopy: effects of the microscopic parts of the probe," *Nanotechnology*, 2012, **23**(20), 205703.

[44] L. Fumagalli, G. Ferrari, M. Sampietro, and G. Gomila, "Dielectric-constant measurement of thin insulating films at low frequency by nanoscale capacitance microscopy," *Appl. Phys. Lett.*, 2007, **91**(24) 243110.

[45] L. Fumagalli, G. Ferrari, M. Sampietro, and G. Gomila, "Quantitative Nanoscale Dielectric Microscopy of Single-Layer Supported Biomembranes," *Nano Lett.*, 2009, **9** (4), 1604–1608.

[46] G. Gomila, J. Toset, and L. Fumagalli, "Nanoscale capacitance microscopy of thin dielectric films," 2008, *J. Appl. Phys.*, **104**(2), 24315.

[47] G. Gramse, a Dols-Perez, M. a Edwards, L. Fumagalli, and G. Gomila, "Nanoscale measurement of the dielectric constant of supported lipid bilayers in aqueous solutions with electrostatic force microscopy," *Biophys. J.*, 2013, **104**(6),

1257–62.

[48] G. Gomila, J. Toset, and L. Fumagalli, “Nanoscale capacitance microscopy of thin dielectric films,” *J. Appl. Phys.*, 2008, **104**(2), 2–10.

[49] V. V. Talanov, A. Scherz, R. L. Moreland, and A. R. Schwartz, “A near-field scanned microwave probe for spatially localized electrical metrology,” *Appl. Phys. Lett.*, 2006, **88**(13).

[50] U. Dürig, D. W. Pohl, and F. Rohner, “Near-field optical-scanning microscopy,” *J. Appl. Phys*, 1986, **59**(3318), 3318-3328.

[51] C. Gao, B. Hu, I. Takeuchi, K.-S. Chang, X.-D. Xiang, and G. Wang, “Quantitative scanning evanescent microwave microscopy and its applications in characterization of functional materials libraries,” *Meas. Sci. Technol.*, 2004, **16**(1), 248–260.

[52] H. Chang, C. Gao, I. Takeuchi, Y. Yoo, J. Wang, P. G. Schultz, and X. Xiang, “Combinatorial synthesis and high throughput evaluation of ferroelectric / dielectric thin-film libraries for microwave applications,” 1998, **72**(17), 2185–2187.

[53] H. Chang, I. Takeuchi, and X. D. Xiang, “A low-loss composition region identified from a thin-film composition spread of (Ba1-x-ySrxCay)TiO3,” *Appl. Phys. Lett.*, 1999, **74**(8), 1165–1167.

[54] M. J. Cadena, S. H. Sung, B. W. Boudouris, R. Reifenberger, and A. Raman, “Nanoscale Mapping of Dielectric Properties of Nanomaterials from Kilohertz to Megahertz Using

Ultrasmall Cantilevers," *ACS Nano,* 2016*,* **10**(4), 4062–4071.

[55] D. R. Rolison, J. W. Long, J. C. Lytle, A. E. Fischer, C. P. Rhodes, T. M. McEvoy, M. E. Bourg, and A. M. Lubers, "Multifunctional 3D nanoarchitectures for energy storage and conversion," *Chem. Soc. Rev.*, 2009, **38**(1), 226–52.

[56] K. Lai, M. Nakamura, W. Kundhikanjana, M. Kawasaki, Y. Tokura, M. A. Kelly, and Z.-X. Shen, "Mesoscopic Percolating Resistance Network in a Strained Manganite Thin Film," *Science*, 2010, **329**(5988), 190—119.

[57] V. V Talanov, C. Del Barga, L. Wickey, I. Kalichava, E. Gonzales, E. A. Shaner, A. V Gin, and N. G. Kalugin, "Few-Layer Graphene Characterization by Near-Field Scanning Microwave Microscopy," *ACS Nano*, 2010, **4**(7), 3831–3838.

[58] W. Kundhikanjana, K. Lai, H. Wang, H. Dai, M. A. Kelly, and Z. Shen, "Hierarchy of Electronic Properties of Chemically Derived and Pristine Graphene Probed by Microwave Imaging," *Nano Lett.*, 2009, **9** (11), 3762–3765.

[59] H. Xu, S. M. Anlage, L. Hu, and G. Gruner, "Microwave shielding of transparent and conducting single-walled carbon nanotube films," *Appl. Phys. Lett.*, 2007, **90**(18), 183119.

[60] E. Brinciotti, G. Gramse, S. Hommel, T. Schweinboeck, A. Altes, M. a. Fenner, J. Smoliner, M. Kasper, G. Badino, S.-S. Tuca, and F. Kienberger, "Probing resistivity and doping concentration of semiconductors at the nanoscale using scanning microwave microscopy," *Nanoscale*, 2015, **7**(35), 14715–14722.

[61] B. G. Ghamsari and S. M. Anlage, “Nanoscale Electrodynamic Response of Nb Superconductors,” *IEEE Trans. Appl. Supercond.*, 2013, **23** (3), 7100104–7100104.

[62] A. El Fellahi, K. Haddadi, J. Marzouk, S. Arscott, C. Boyaval, T. Lasri, and G. Dambrine, “On-Wafer Probe Station for Microwave Metrology at the Nanoscale,” 2005, *Instrumentation and Measurement Technology Conference (I2MTC)*.

[63] A. Karbassi, D. Ruf, A. D. Bettermann, C. A. Paulson, D. W. van der Weide, H. Tanbakuchi, and R. Stancliff, “Quantitative scanning near-field microwave microscopy for thin film dielectric constant measurement.,” 2008, *Rev. Sci. Instrum.*, **79**(9), 94706.

[64] M. C. Biagi, R. Fabregas, G. Gramse, M. Van Der Hofstadt, A. Juárez, F. Kienberger, L. Fumagalli, and G. Gomila, “Nanoscale Electric Permittivity of Single Bacterial Cells at Gigahertz Frequencies by Scanning Microwave Microscopy,” *ACS Nano*, 2016, **10** (1), 280–288.

[65] I. Ferain, C. a. Colinge, and J.-P. Colinge, “Multigate transistors as the future of classical metal–oxide–semiconductor field-effect transistors,” *Nature*, 2011, **479**(7373), 310–316.

[66] J. Kim, A. J. Hong, S. M. Kim, K.-S. Shin, E. B. Song, Y. Hwang, F. Xiu, K. Galatsis, C. O. Chui, R. N. Candler, S. Choi, J.-T. Moon, and K. L. Wang, “A stacked memory device on logic 3D technology for ultra-high-density data storage,” *Nanotechnology*, 2011, **22**(25), 254006.

[67] C. Hu, Z. Mou, G. Lu, N. Chen, Z. Dong, M. Hu, and L. Qu, "3D graphene-Fe3O4 nanocomposites with high-performance microwave absorption," *Phys. Chem. Chem. Phys.*, 2013, **15**(31) 13038–43

[68] F. Castles, D. Isakov, A. Lui, Q. Lei, C. E. J. Dancer, Y. Wang, J. M. Janurudin, S. C. Speller, C. R. M. Grovenor, and P. S. Grant, "Microwave dielectric characterisation of 3D-printed BaTiO3/ABS polymer composites," *Sci. Rep.*, 2016, **6**, 22714.

[69] S. Baskaran, J. Liu, K. Domansky, N. Kohler, X. Li, C. Coyle, G. E. Fryxell, S. Thevuthasan, and R. E. Williford, "Low Dielectric Constant Mesoporous Silica Films Through Molecularly Templated Synthesis," *Adv. Mater.*, 2000, **12**(4), 291–294.

[70] B. Wood, B. McDougall, O. Chan, A. Dent, C.-N. Ni, R. Hung, H. Chen, P. Xu, P. Nguyen, M. Okazaki, D. Mao, X. Xu, R. Ramiraz, M.-P. Cai, M. Jin, W. Lee, A. Noori, M. Shek, and C.-P. Chang, "3D MOSCAP Vehicle for Electrical Characterization of Sidewall Dielectrics for 3D Monolithic Integration," *ECS Trans.*, 2011, **35**(2), 69–81.

[71] G. Gomila, J. Toset, and L. Fumagalli, "Nanoscale capacitance microscopy of thin dielectric films," *J. Appl. Phys.*, 2008, **104**(2) 24315.

[72] T. I. K. Richard S. Muller, *Device Electronics for Integrated Circuits*, 3rd ed. Wiley, 2003.

[73] K. W. Vogt, M. Houston, M. F. Ceiler, C. E. Roberts, and P. A. Kohl, "Improvement in dielectric properties of low temperature PECVD silicon dioxide by reaction with hydrazine," *J. Electron. Mater.*, 1995, **24**(6), 751–755.

[74] M. F. Ceiler Jr., P. A. Kohl, and S. A. Bidstrup, "Plasma-Enhanced Chemical Vapor Deposition Silicon Dioxide Deposited at Low Temperatures," *Journal of Electrochemical Society*, 1995, **142**(6), 2067–2071.

[75] B. Fowler, "Relationships between the material properties of silicon oxide films deposited by electron cyclotron resonance chemical vapor deposition and their use as an indicator of the dielectric constant," *J. Vac. Sci. Technol. B Microelectron. Nanom. Struct.*, 1994, **12** (1), 441.

[76] D. E. Steinhauer, C. P. Vlahacos, F. C. Wellstood, S. M. Anlage, C. Canedy, R. Ramesh, A. Stanishevsky, and J. Melngailis, "Quantitative imaging of dielectric permittivity and tunability with a near-field scanning microwave microscope," *Rev. Sci. Instrum.*, 2000, **71**(7), 2751.

[77] S. C. Hagness, E. C. Fear, and A. Massa, "Guest editorial: Special cluster on microwave medical imaging," *IEEE Antennas Wirel. Propag. Lett.*, 2012, **11**, 1592–1597.

[78] C. J. Diederich, "Thermal ablation and high-temperature thermal therapy: Overview of technology and clinical implementation," *Int. J. Hyperth.*, 2005, **21** (8), 745–753.

[79] A. P. O'Rourke, D. Haemmerich, P. Prakash, M. C. Converse, D. M. Mahvi, and J. G. Webster, "Current status of liver tumor ablation devices," *Expert Rev. Med. Devices*, 2007, **4**(4), 523–537.

[80] R. W. Y. Habash, R. Bansal, D. Krewski, and T. Ha, "Thermal Therapy , Part III : Ablation," 2007, **35**, 37–121.

[81] T. C. Winter, P. F. Laeseke, and F. T. Lee, "Focal Tumor

Ablation: a New Era in Cancer Therapy," *Ultrasound Q.*, 2007, **22**(3), 195–217.

[82] S. Banik, S. Bandyopadhyay, and S. Ganguly, "Bioeffects of microwave - a brief review," *Bioresour. Technol.*, 2003, **87**(2), 155–159.

[83] K. Grenier, D. Dubuc, T. Chen, F. Artis, T. Chretiennot, M. Poupot, and J. J. Fournié, "Recent Advances in Microwave-Based Dielectric Spectroscopy at the Cellular Level for Cancer Investigations," *IEEE Transactions on Microwave Theory and Techniques*, 2013, **61**(5), 2023–2030.

[84] A. Imtiaz, T. M. Wallis, S.-H. Lim, H. Tanbakuchi, H.-P. Huber, A. Hornung, P. Hinterdorfer, J. Smoliner, F. Kienberger, and P. Kabos, "Frequency-selective contrast on variably doped p-type silicon with a scanning microwave microscope," *J. Appl. Phys.*, 2012, **111**(9), 93727.

[85] C. Plassard, E. Bourillot, J. Rossignol, Y. Lacroute, E. Lepleux, L. Pacheco, and E. Lesniewska, "Detection of defects buried in metallic samples by scanning microwave microscopy," *Phys. Rev. B*, 2011, **83**(12), 121409.

[86] G. Gramse, E. Brinciotti, A. Lucibello, S. B. Patil, M. Kasper, C. Rankl, R. Giridharagopal, P. Hinterdorfer, R. Marcelli, and F. Kienberger, "Quantitative sub-surface and non-contact imaging using scanning microwave microscopy," *Nanotechnology*, 2015, **26**(13), 135701.

[87] C. Gao, B. Hu, I. Takeuchi, K.-S. Chang, X.-D. Xiang, and G. Wang, "Quantitative scanning evanescent microwave microscopy and its applications in characterization of

functional materials libraries," *Meas. Sci. Technol.*, 2005, **16**(1), 248–260.

[88] C. Gao, T. Wei, F. Duewer, Y. Lu, and X.-D. Xiang, "High spatial resolution quantitative microwave impedance microscopy by a scanning tip microwave near-field microscope," *Appl. Phys. Lett.*, 1997, **71**(13), 1872.

[89] C. Gao and X.-D. Xiang, "Quantitative microwave near-field microscopy of dielectric properties," *Rev. Sci. Instrum.*, 1998, **69**, 3846.

[90] T. Tai, B. Ghamsari, and S. M. Anlage, "Nanoscale electrodynamic vortex response of Nb superconductors," 2012, *CPEM Digest (Conference on Precision Electromagnetic Measurements)*, 328–329.

[91] Y. J. Oh, H.-P. Huber, M. Hochleitner, M. Duman, B. Bozna, M. Kastner, F. Kienberger, and P. Hinterdorfer, "High-frequency electromagnetic dynamics properties of THP1 cells using scanning microwave microscopy," *Ultramicroscopy*, 2011, **111**(11), 1625–9.

[92] M. Farina, S. Member, A. Di Donato, D. Mencarelli, G. Venanzoni, and A. Morini, "High Resolution Scanning Microwave Microscopy for Applications in Liquid Environment," 2012, **22**(11), 595–597.

[93] U. Kaatze, "Measuring the dielectric properties of materials. Ninety-year development from low-frequency techniques to broadband spectroscopy and high-frequency imaging," *Meas. Sci. Technol.*, 2013, **24**(1), 12005.

[94] R. Buchner, J. Barthel, and J. Stauber, "The dielectric

relaxation of water between 0º C and 35º C," 1999, *Chem. Phys. Lett.,* **306**(2), 57-63.

[95] A. N. Reznik, "Quasistatics and electrodynamics of near-field microwave microscope," 2014, *J. Appl. Phys.*, **115**(8), 84501.

[96] J. Hoffmann, M. Wollensack, M. Zeier, J. Niegemann, H. P. Huber, and F. Kienberger, "A calibration algorithm for nearfield scanning microwave microscopes," *12th IEEE International Conference on Nanotechnology (IEEE-NANO)*, 2012, 1–4.

[97] F. Artis, T. Chen, T. Chretiennot, J.-J. Fournie, M. Poupot, D. Dubuc, and K. Grenier, "Microwaving Biological Cells: Intracellular Analysis with Microwave Dielectric Spectroscopy," *IEEE Microw. Mag.*, 2015, **16**, (4), 87–96.